POLITECNICO DI TORINO

Department of Applied Science and Technology

Master's Degree in Physics of Complex Systems

Master's Degree Thesis

Structure and Dynamics of Single-Crystalline Superconductor $LaPt_2Si_2$

Supervisors
Prof. RENATO GONNELLI
Prof. KIM LEFMANN
PhD student ELISABETTA NOCERINO

Candidate
IRENE SANLORENZO

April 2022

Abstract

The coexistence of superconductivity (SC) and charge- and/or spin-density waves (CDW and/or SDW) is fundamental to our understanding behind the mechanism of high-Tc SC. Materials like Fe-based pnictides, transition metal dichalcogenides, heavy fermions or cuprate superconductors have gained significant interest as the fluctuations associated with CDW and /or SDW are considered to be a key factor in inducing SC in these systems.

Recently, the quasi-2D Pt-based rare earth intermetallic material $LaPt_2Si_2$ has attracted a lot of attention as it exhibits strong interplay between CDW and SC. $LaPt_2Si_2$ crystallizes in a $CaBe_2Ge_2$-type tetragonal structure (space group P4/nmm), where two non-equivalent layers (Si_2–Pt_1–Si_2) and (Pt_2–Si_1–Pt_2) are arranged in alternating stacking separated by lanthanum atoms, which results to a crystal structure lacking inversion symmetry. Around T_{CDW}= 112 K, a structural transition from a high-temperature tetragonal to a low-temperature orthorhombic structure, together with the CDW transition has been reported in polycrystalline $LaPt_2Si_2$. Below T_{SL}= 10 K, superlattice reflections were observed, indicating that the unit cell of the $LaPt_2Si_2$ is tripled in size along the [100] direction. Below T_{SC} = 1.22 K the material becomes a superconductor.

Theoretical calculations show that the Fermi surface of $LaPt_2Si_2$ is of two-dimensional nature and CDW and SC coexist in the (Si_2-Pt_1-Si_2) layer. Also the calculations of the phonon dispersions predict phonon-softening instabilities, indicating structural instability. The softened phonon modes would mainly arise from Pt_1, suggesting that the CDW transition occurs in the Pt_1 layers and has a large electron-phonon interaction. Until now, the vast majority of the results have been reported only on polycrystalline samples, but the very recent synthesis of good quality single crystals allows further investigations to clarify the nature of the interplay between the CDW and SC in $LaPt_2Si_2$.

This work presents recent inelastic neutron scattering results of $LaPt_2Si_2$ single crystals performed at the HRC instrument in J-PARC, Japan. We investigated the phonon excitation spectra below and above the structural transition T_{CDW}= 85 K, and clearly observed the CDW wavevector $\vec{q}$=(0.35,0,0), but no phonon softening was observed. In addition, XRD and Raman scattering have also been performed in order to characterize the material and better understand its properties. The overall measured phonon dispersions show the two main energy levels predicted by theoretical calculations. Moreover, the weak superlattice peaks appear at position previously identified [1]. Interestingly, when increasing temperature the superlattice peaks increase even above T_{CDW}, an effect which will require further investigations to be fully understood.

Acknowledgements

This work would not have been possible without my supervisor at Niels Bohr Institute, professor Kim Lefmann, for his constant help and support and the opportunity given to be part of the research group in a stimulating and international environment. I would like to thank professor Renato Gonnelli for his supervision from Politecnico di Torino and his support in the thesis work. Elisabetta Nocerino, PhD student from KTH, Stockholm has been a constant guide for me, thank you for your help from the very first experiment to the end, I have learnt a lot from you. Thank you to professor Martin Månsson from KTH, Stockholm and Yasmine Sassa from Chalmers University, Göteborg for the constant involvement and support given and for the original idea behind the experiment which is the core of this thesis. I would like to thank all the research group at NBI, many people changed throughout my path but all of them contributes somehow to my stay in Copenhagen. I would like also to include the sample providers Prof. Zakir Hossain of the Indian Institute of Technology, Kanpur, India and Dr. Arumugam Thanizhavel of the Tata Institute of Fundamental Research, Mumbai, India, the instrument scientist of HRC (J-PARC Center) Shinichi Itoh also Professor Takatsugu Masuda, Shinichiro Asai and Shunsuke Hasegawa from The Institute for Solid State Physics, Tokyo University. Moreover, the laboratory responsible in Stockholm university Dr. Andrew Kentaro Inge for the XRD data and the laboratory responsible in Chalmers University, Ezio Zanghellini, for the Raman experiment. If the research group could collect the data is thanks to all the people involved in the several facilities and labs around the globe.

Not enough words can be spent for my family, especially my mum and dad that have always been a solid pillar throughout my whole university path. Thank you to the person that has always been there for me, Bernardo, the person that made me see the light in tough times, the person that face his fears to take a plane for me. Thank you to Cristina, endless calls have been spend from North to South of Europe, but you can be sure that at 45 minutes the call had to restart again. You have been there since the beginning, it was inspiring and much fun to grow with you. Together with Eliana, we survived this Master, between a Spritz and a jungle of emotions. Even if now you are back in Puglia, Maracas will always be

there. Another special person worth mentioning is Tonno, I hope we will dance together again but until then, thank you for the good laughs and great time. My dance partners, Crox and Frago, and our chat group that change 100 names in the meantime, thank you for your constant support and for always being there. Thank you to my university mate that then became friends, in particular Adrian, someone you could always rely on for a physics lecture or a friendly beer, Sara that shared with the pain and gain of lots of exams but also someone that would pull you back to reality and Jessica that was always there to help and pull me through some of the final steps of this path. Thanks to BEST, thank you for letting me meet people from around the globe, for opening my mind and for pushing me outside of my conform zone.

Table of Contents

List of Tables

List of Figures

Acronyms

BSC

Bardeen-Cooper-Schrieffer

CDW

charge density wave

DAVE

Data Analysis and Visualization Environment

DFT

Density Functional Theory

EDX

Energy dispersive x-ray spectroscopy

FS

Fermi surface

HRC

High Resolution Chopper Spectrometer

INS

inelastic neutron scattering

ISSP

Institute of Solid State Physics

JAEA

Japan Atomic Energy Agency

JPARC
Japan Proton Accelerator Research Complex

KEK
High Energy Acceleration Research Organization

LA
Longitudinal Acoustic

LO
Longitudinal Optical

MLF
Material and Life Science Experimental Facility

NBS
neutron Brillouin scattering

NIST
National Institute of Standards and Technology

NS
Neutron Scattering

RT
Room Temperature

SC
superconductivivity

SDW
spin density wave

SEM
Scanning electron microscopy

SOC
Spin-Orbit Coupling

T_c

Superconducting Critical Temperature

T_{CDW}

Charge Density Wave Temperature

TOF

Time-of-Flight

XRD

X-rays diffractometer

Chapter 1

Introduction

1.1 Motivation

Superconductivity describes the property of conducting electricity with the complete disappearance of electrical resistance in various materials when they are cooled below a characteristic temperature. It is characterized by an expulsion of the magnetic field from the interior of a sample. A simplified way to classify them is to distinguish two types: low-temperature, or conventional, superconductivity, which generally only occurs within a few degrees of absolute zero and is well-understood by BCS theory or its extensions; and high-temperature superconductivity, which is not well understood [2] [3]. Unconventional superconductivity refers to superconductors where the Cooper pairs are not bound together by phonon exchange, instead another type of exchange occurs e.g. spin fluctuation interactions.

Superconductivity has a lot of potential in today's society, new applications for superconductors are developed every day, however there is still a lot to know about superconducting materials. The final goal of investigating high-temperature SC is to hopefully, one day, be able to make SC that work at accessible temperatures. An example is the use of superconductivity applied to power transmissions, which would dramatically reduce energy costs around the world but there are many more applications linked to technologies.

The mechanism of unconventional superconductivity is still largely unknown, years after the discovery of the first cuprate superconductor by Bednorz and Muller (1986) [4]. For this reason, much research has gone into elucidating the microscopic properties of the many different families of unconventional superconductors with the aim of finding the mechanism that binds (Cooper) pairs of electrons together, in turn forming the basis for the emergence of the superconducting state. One common theme is the inherent two-dimensionality of these materials, another is the spontaneous formation in these materials of one-dimensional "stripe"-like structures,

which in general carry both charge and (antiferro-)magnetism [5] [6]. In addition, to form the Cooper pairs a dynamic interaction is searched for, similar to the (BCS) electron-phonon coupling mechanism known from conventional superconductivity, e.g. seen in simple metals [2] [3].
A superior method to study lattice- and magnetic dynamics on the microscopic scale is neutron scattering, which is the central technique for this study. The two-dimensional superconductor studied using neutron scattering is $LaPt_2Si_2$.

1.2 $LaPt_2Si_2$

The coexistence of superconductivity (SC) and charge- and/or spin-density waves (CDW and/or SDW) is fundamental to our understanding behind the mechanism of high-Tc SC. CDW and SC are states of broken symmetry in solids which require electron-electron interaction mediated by phonons and are originated by instabilities of the Fermi surface (nesting, gap). However, charge redistribution and Cooper pairing are two independent phenomena with opposite effects on the electronic spectrum: SC induces infinite conductivity, CDW induces semiconductor gap and non-conducting state. Even if their effect is opposite, it has been observed that they can coexist. Materials like Fe-based pnictides, transition metal dichalcogenides, heavy fermions or cuprate superconductors have gained significant interest as the fluctuations associated with CDW and /or SDW are considered to be a key factor in inducing SC in these systems.
Recently, RPt_2Si_2 (R = La, Pr) system has attracted an intensive research interest as it exhibits strong interplay between CDW and superconductivity. Unlike cuprates and pnictides, SDW has not been found in these materials, one reason to expect so is that they do not have a magnetic ion, unlike Cu or Fe. $LaPt_2Si_2$ crystallizes in a $CaBe_2Ge_2$-type tetragonal structure (space group P4/nmm), seen in Fig. 1.1, where two non-equivalent layers (Si_2–Pt_1–Si_2) and (Pt_2–Si_1–Pt_2) are arranged in alternating stacking separated by lanthanum atoms, which results in a crystal structure lacking inversion symmetry.
Theoretical calculations show that the Fermi surface of $LaPt_2Si_2$ is of two-dimensional nature [7] and CDW and SC coexist spatially in the (Si_2–Pt_1–Si_2) layer. Also the calculations of the phonon dispersions predict phonon-softening instabilities, which should lead to structural instability [7, 8]. The softened phonon modes would mainly arise from Pt_1, suggesting that the CDW transition occurs in the Pt_1 layers and has a large electron-phonon interaction [7, 8].

In polycrystalline samples, a first order transition was observed from high temperature tetragonal to low temperature orthorhombic structure, which is believed to be due to a CDW transition at T_{CDW} = 112 K. Below T_{SL}= 10 K, superlattice reflections corresponding to (n/3,0,0) where n=1 and 2 were observed, indicating that the unit cell of the $LaPt_2Si_2$ is tripled in size along the [100] direction at low temperature. Moreover at lower temperature there is a SC transition at $T_C = 1.22$ K [9].

Later a single-crystalline $LaPt_2Si_2$ sample was measured with XRD [1]. The diffraction patterns show the occurrence of satellite Bragg peaks corresponding to the wave vector $q \approx [0.36, 0, 0)]$. This additional periodicity, is probably related to the supposed CDW state. The satellites have their maximum intensity at 85 K, disappear above 175 K and almost vanish below 85 K.

The phonon dispersion in this sample has never been measured, therefore the aim of the inelastic neutron scattering experiment at High Resolution Chopper Spectrometer (HRC) at J-PARC was to investigate the phonon modes in single crystalline, quasi-2D Pt-based rare earth intermetallic $LaPt_2Si_2$, in order to observe the phonon softening predicted by theoretical calculations, and confirm in this way the occurrence of CDW (the softening should be a signature of CDW) [8] [10]. Maps for the phonon spectra at 3 different temperatures (3 K, 85 K, 220 K) were acquired. The low temperature crystal structure, in the CDW phase, is not solved (the only information in this regard is the fact that it should be orthorhombic). The investigation of $LaPt_2Si_2$ single crystals is particularly important due to the strong directional dependency of the in-plane CDW and superconductivity.

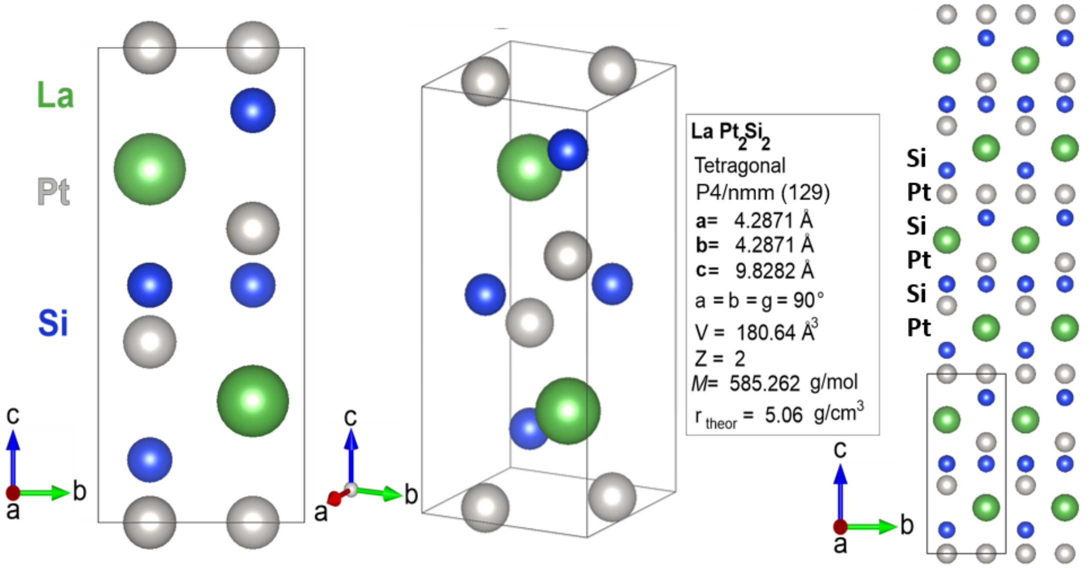

Figure 1.1: Crystallographic data and atomic structure of $LaPt_2Si_2$. The layered structure with the alternating stacking planes (Si_2–Pt_1–Si_2) and (Pt_2–Si_1–Pt_2) is clearly visible along the c axis. It has been calculated with VESTA program [11].

1.3 Previous studies on $LaPt_2Si_2$

The properties of $LaPt_2Si_2$ as a single crystal are not much explored since the majority of results have been reported only on polycrystalline samples [9][12][13][14]. Recently, several papers have been published in order to fully characterize and understand this complex compound [1] [15].

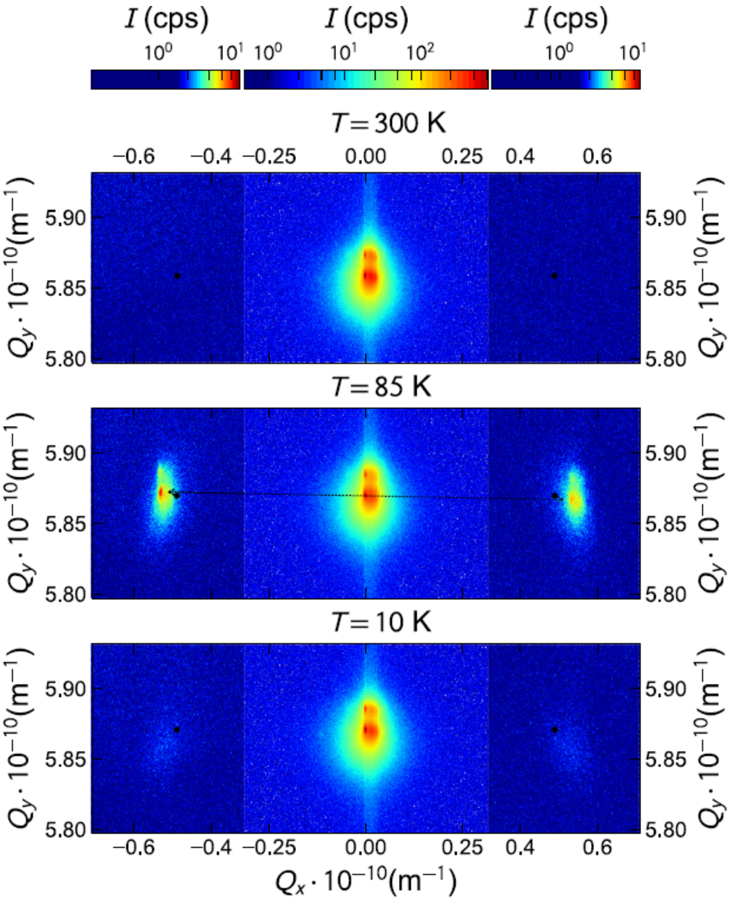

Figure 1.2: Reciprocal space map of (0 4 0) diffraction at T = 300, 85, and 10 K. The scattering plane corresponds to the basal plane. The black point shows the position of q = (1/3, 0, 0). From [1].

In a recent publication [1], X-ray diffraction (XRD) patterns on single crystalline $LaPt_2Si_2$ show the occurrence of satellite Bragg peaks corresponding to the wave vector q ≈ [0.36, 0, 0)]. The satellites indicate the occurrence of the CDW transition at low temperatures [1]. In the same paper, the group said that a structural transition might occur due to the observation of the broadening of a structural peak which implies that a and b axis are no longer equivalent [1]. The

satellites reveal maximum intensity at 85 K, disappear above 175 K and almost vanish below 85 K, as it is shown in Fig. 1.2. The map acquired during the INS experiment at HRC allow to observe incommensurate reflections with a temperature dependence that will be compared with the literature.
X-rays characterisation was also performed on the powdered single crystal, with in-house equipment and the pattern was refined with a tetragonal $CaBe_2Ge_2$ model, showing that the tetragonal symmetry is preserved down to low temperature [1], in contrast with first order structural phase transition from tetragonal (high-T) to orthorhombic (low-T) present in the polycrystalline samples [9].
In order to better understand the structure, XRD diffraction has been performed as function of T in a range from 80K to 300K, using a Cu-alpha D8 diffractometer, on these crystals to collect reliable structural information. However such a measurement would not provide complete structural characterization as the measurement system is limited in temperature range and resolution. Instead in Fig. 1.3 it is possible to see XRD previously performed by Falkowski group using in-house equipment.

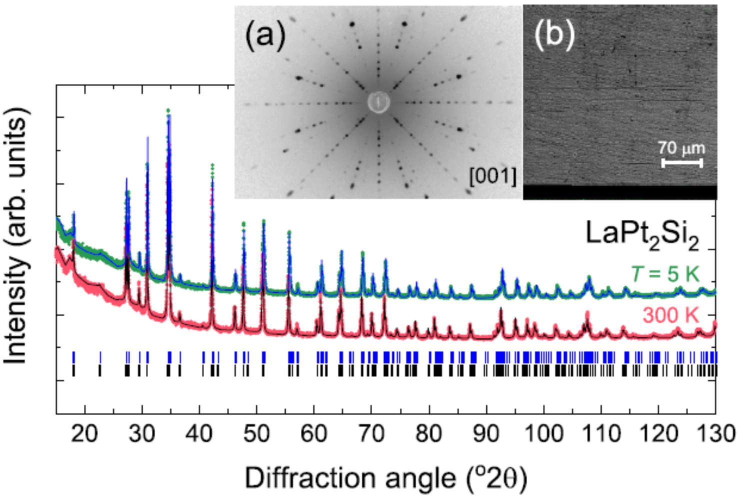

Figure 1.3: XRD powder patterns of $LaPt_2Si_2$ collected at T = 5 and 300 K refined using the $CaBe_2Ge_2$-type structure, space group P4/nmm (blue and black lines, respectively). The peak positions are indicated by the vertical bars bellow the data. Inset (a) shows the Laue diffraction pattern of $LaPt_2Si_2$ single crystal with a view along the [001] axis. Inset (b) shows the SEM micrograph obtained from the surface of single-crystalline $LaPt_2Si_2$ used for the EDX analysis. From [1].

Electrical resistivity reveals that the 85 K transition is hysteretic in temperature, with the difference between heating and cooling being almost 10 K, proving the first-order type of the transition [1]. The transition dramatically enhances resistivity in the low-T state, pointing to a formation of a pseudogap. This, however, does allow a superconducting state, arising below Tc = 1.6 K [1]. The temperature dependence of the upper critical field is not compatible with the weak coupling BCS theory[1]. Strong anisotropy of the electronic structure and its dramatic changes at the structure transition are manifest also in thermal expansion and thermoelectric power [1].

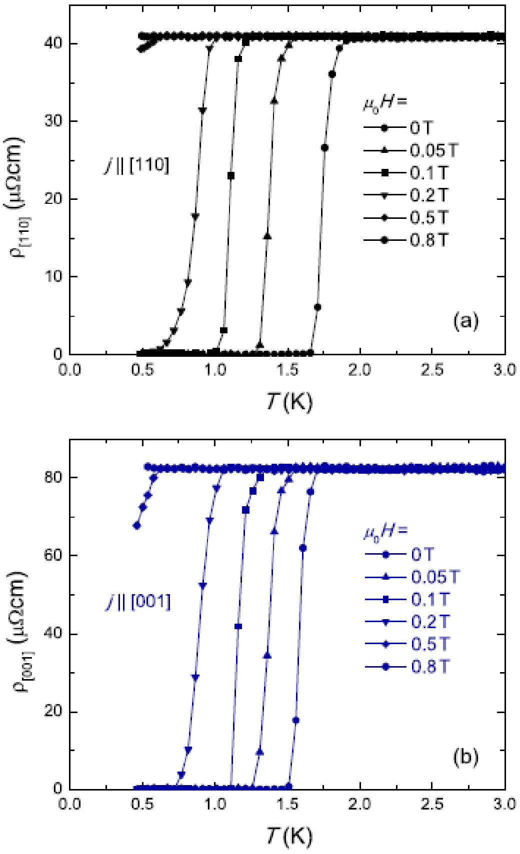

Figure 1.4: Low-T detail ρ(T) in vicinity of the superconducting transition for both crystallographic directions of single-crystalline $LaPt_2Si_2$ in various applied magnetic fields. From [1].

A sharp superconducting transition bringing resistivity to the zero value is shown in Fig. 1.4. The recorded actual values of critical temperature are for both directions slightly different, $T_c^{[110]}$ = 1.65 K and $T_c^{[001]}$= 1.5 K. At present it is not clear what is the nature of the small difference. The presence of superconductivity is a remarkable fact as archetypal CDW systems are not superconductors [16] as the two phenomena (CDW/SC) are competitive and detrimental to each other. In Figs. 1.4(a) and 1.4(b), it is shown the view of the low-T range together with effect of an applied magnetic field on the superconducting transition for both crystallographic directions. In both cases, T_c gradually decreases with increasing field and already a field of 0.5 T pushes T_c below 0.4 K [1].

The superconductivity itself exhibits certain unconventional features, not compatible with the common weak coupling BCS model [1].

Chapter 2

Basics of Neutron Scattering

This chapter is mostly based on the Notes of the Neutron Scattering Course that I took at the University of Copenhagen, Niels Bohr Institute, by Kim Lefmann [17].

2.1 Introduction to Neutron Scattering, properties of the neutron and five reasons to use them

Neutron scattering is a means to study the structure, dynamics (movement of atoms) and the compositions of materials on the atomic and nanometer scale.
Today nearly 8000 researchers who use neutron centres for their scientific work could be identified in Europe. They rely on the open access and user programs at nine neutron sources across Europe and additionally eight smaller sources for specific applications. Also neutron sources from abroad in America, Japan, Australia and Russia are used by European researchers [18]. Neutrons play an important role in the advancement of research into many different areas of science, such as biology, materials science, chemistry, particle physics as well as engineering and medicine. Neutron scattering also present some disadvantages, it is rare and time consuming, experiments last from hours to days in neutron facilities. As the capacity is limited, not all the proposals done by international and local researchers can be accepted. As a consequence, neutron scattering should be used only when other methods are inadequate. X-ray scattering is the technique chosen for the study of atomic and nanometer-scale structure in materials. X-ray sources present lots of advantages, they are more common and they are much stronger than neutron sources, especially for synchrotron X-ray sources. However, for some purposes

neutrons are instead chosen due to some properties that make them more convenient.

The neutron is a neutral particle, which is stable only in the confines of the nucleus of the atom. Outside the nucleus, the neutron decays with a mean lifetime of about $\tau = 886$ s [19], it is much longer than the time a neutron spends within a scattering experiment, which is a fraction of a second. As a consequence, neutron decay is neglected in experiments. Its mass is rather close to that of a proton ($m_n = 1.675 \cdot 10^{-27}$ kg) [20].

Neutron has a particle-wave duality. When a neutron is slown down to low speed, thousands m/s, it behaves as a wave. The neutron wave interfere with itself through scattering from the nuclei in materials. From studying the interference pattern, it is possible to know the structure of the material, the properties and the chemical composition. In neutron scattering, the wave nature is hidden in the neutron wave number

$$k = \frac{2\pi}{\lambda} \tag{2.1}$$

or in the wave vector of length k (same direction as velocity)

$$\vec{k} = \frac{m_n \vec{v}}{\hbar} \tag{2.2}$$

Å (10^{-10} m) is the unit of measure for wavelengths, and Å^{-1} for wave numbers. The neutron velocity is always measured in m/s. The neutron kinetic energy is given by

$$E = \frac{\hbar^2 k^2}{2m_n} \tag{2.3}$$

which has a unit of measure in eV or meV, in particular 1 eV = 1.60218 $\cdot 10^{-19}$ J.

Adequate flux density for neutron scattering investigations of materials are produced by neutron sources which are based on one of two principles, also illustrated in Fig. 2.1:

- Fission. It takes place within a reactor, it produces a high continuous flux of neutrons and can be used for a variety of purposes including power generation and experiments.

- Spallation. A high-flux source in which protons that have been accelerated to high energies hit a target material, prompting the emission of neutrons.

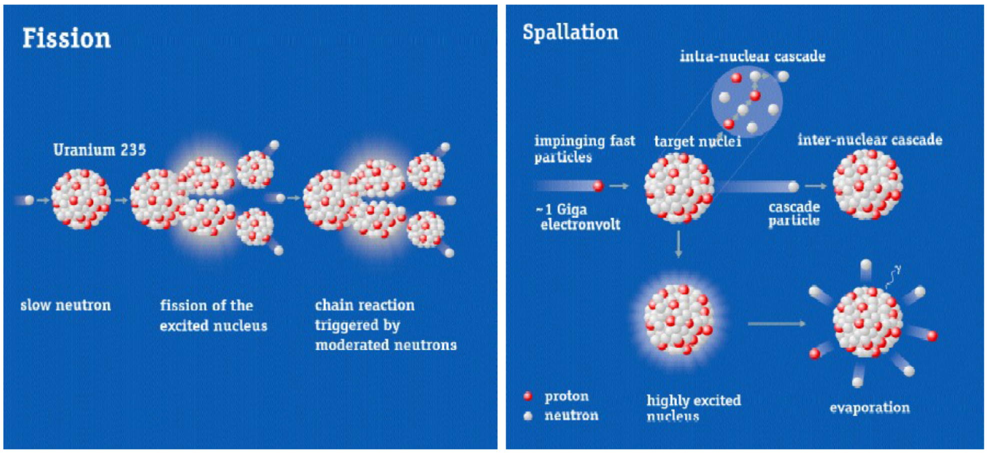

Figure 2.1: The two main methods of neutron production. Left: Traditional nuclear reactors make use of production of neutrons for maintaining the chain reaction; a surplus of neutrons can be used for neutron scattering. Right: Protons accelerated into the GeV regime can excite heavy nuclei with a large neutron surplus, creating free neutrons among the reaction products. From [17].

One common feature is that neutrons are moderated to slower velocities close to the source and then transported to the neutron scattering instruments in neutron guide systems. More details on the instrumentation will be given in later chapters. There are two types of scattering, elastic and inelastic. The crystal is composed of lattice planes, if a certain condition is fulfilled, there is constructive interference between scattered waves from different lattice planes and the condition is the Bragg Law:

$$n\lambda = 2dsin(\theta) \tag{2.4}$$

The scattering vector is

$$\vec{q} = \vec{k}_i - \vec{k}_f \tag{2.5}$$

where the wave vectors k have the length of k (wave number) and direction of propagation of the neutron; it is the central concept as it links the experiment with the material. $\vec{q}$ should be equal to $2\pi/d$ to fulfil the Bragg law. In inelastic scattering instead, the neutron comes in with $\vec{k}_i$ and the final neutron has a $\vec{k}_f$ with a different length, therefore the neutron lose some energy. This leads to the need to define an energy transfer, the energy is conserved but given to the material. As a consequence, one quantum of vibration appear in the material, therefore the energy lost by the neutron is the same as the energy gained by the material. Also the momentum is conserved.

By studying the energy transfer and the momentum of the neutron it is possible to study what is happening inside the material, for example the dispersion relation, i.e. the correspondence between q vector and the energies for vibrations inside the material.

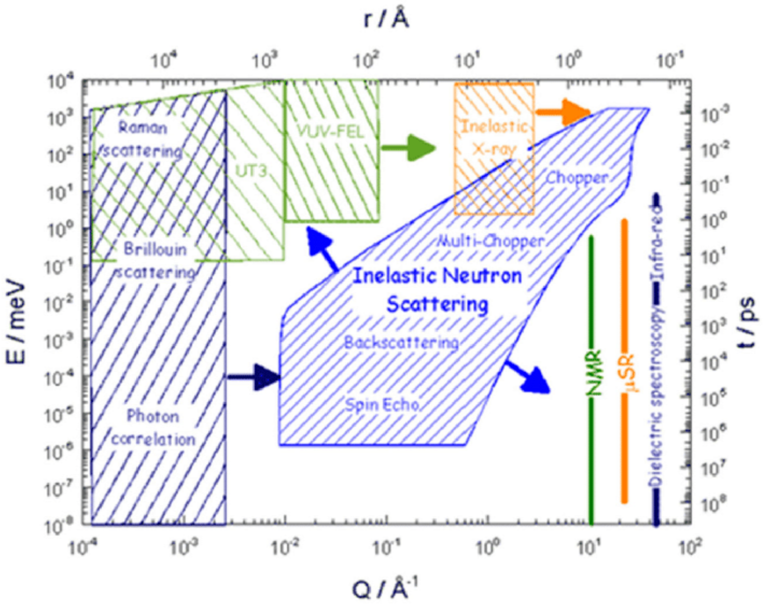

Figure 2.2: Energy and momentum coverage of inelastic neutron scattering. From [21].

In Fig. 2.2, it is possible to observe the energy and q coverage of inelastic neutron scattering. It covers four order of magnitude in length and nine order of magnitude in time scale. However, all the entire blue area in Fig. 2.2 cannot be covered simultaneously. The instrument needs to be specialised to in a particular range and this is why neutron scattering is very rich in instrument set ups.

Neutron has a wavelength typically of the order of one Armstrong and thus can study the structure of materials. There are five reasons to use neutrons instead of X-Rays:

- The neutron has a wavelength (Å) and an energy (meV) comparable to the typical atomic spacing and vibrational energies therefore it is possible to study both the atomic structure and dynamics.

- The neutron scattering cross section varies randomly through the periodic table and is isotope dependent. It is possible to probe isotopes and light elements, because the neutrons scatter from the core, neutrons feel the nuclear potential, i.e. the inner structure of the nucleus.

- The neutron probe is weak, the signal could be weak but most of the displayed neutrons scatter only once so it is possible to use simulations to study them.
- The neutron is highly penetrating, it is possible to study thick samples and samples in a complex environment.
- The neutron has a magnetic moment but no charge, enabling the study of magnetic structure and dynamics.

2.2 The neutron flux and cross section

The neutron flux is defined as

$$\psi = \frac{\text{number of neutrons impinging on a surface per sec}}{\text{surface area perpendicular to neutron beam direction}} \tag{2.6}$$

usual values are $10^4 - 10^9$ n/(cm^2 s).
The scattering cross section is defined as the ability of the system to scatter neutrons

$$\sigma = \frac{1}{\psi}\text{number of neutrons scattered per second} \tag{2.7}$$

which has units of area.
If the sample is very thick then it will scatter everything, instead for thin samples where the beam is not significantly attenuated through the scattering, the cross section will be depending linearly on the system (sample) volume like $\sigma = V\Sigma$.
To understand how σ is distributed over the solid angle, the calculation leads to the differential scattering cross section which is the intensity of neutrons scattered into a particular solid angle

$$\frac{d\sigma}{d\Omega} = \frac{1}{\psi}\frac{\text{number of neutrons scattered into the solid angle } d\Omega \text{ per sec}}{d\Omega} \tag{2.8}$$

The total number of scattered neutrons is the integral of neutrons per solid angle over all of the 4π solid angle, hence

$$\sigma = \int \frac{d\sigma}{d\Omega} d\Omega \tag{2.9}$$

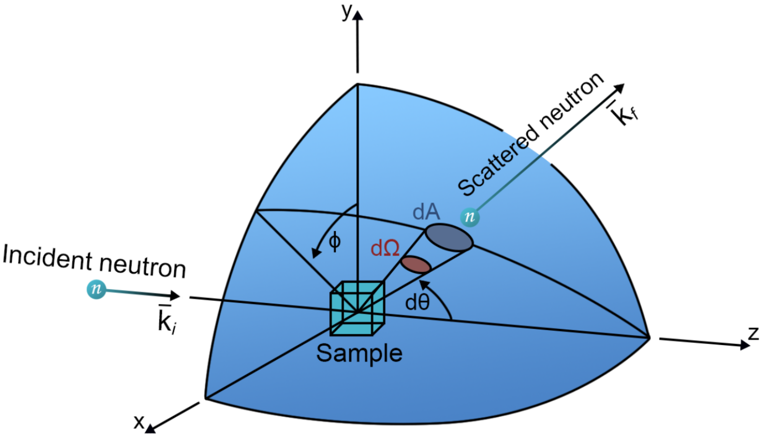

Figure 2.3: An illustration of the scattering geometry. The incoming neutrons, labeled k_i, scatter at the center of the sphere with the scattering angle 2θ and azimuthal angle ϕ. The neutrons scattered into the solid angle element $d\Omega$ (or detector area dA), are described with k_f. From [22].

When a neutron is absorbed by a nucleus, a wide range of radiations can be emitted or fission can be induced. In most cases, the absorption cross section, σ_a, of thermal neutrons is inversely proportional to the neutron velocity therefore: $\sigma_a \propto \lambda$.

There is an actual absorption cross section for each and every nucleus,

$$\sigma_{a,j} = \sigma_{a,j,th}\frac{\lambda}{\lambda_{th}} \tag{2.10}$$

where $\lambda_{th} = 1.7982$ Å. The absorption cross section for isotope j is given as $\sigma_{a,j,th}$ per nucleus in units of "barns" (1 barn $= 10^{-28}$ m ^{2}) and they are all tabulated e.g. see the Neutron Data Booklet [23] or the NIST homepage [24].

The total absorption cross section is $\sigma_a = \sum_j \sigma_{a,j}$. The total cross section is the scattering cross section plus the absorption cross section which is the one to take into account in order to calculate how the beam is attenuated through the sample.

2.3 The neutron wave

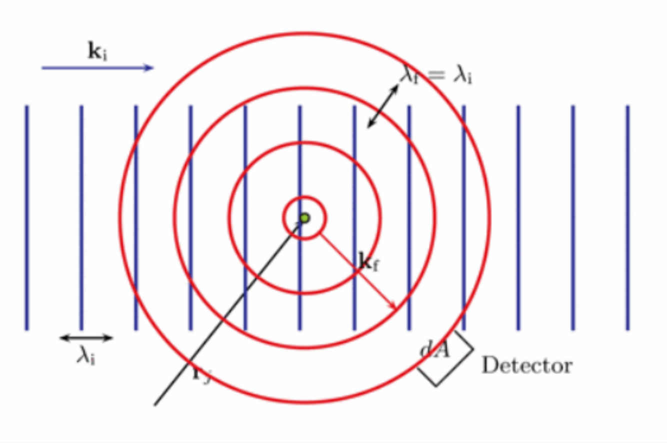

Figure 2.4: An illustration of the initial wave, ψ_i, of wavelength λ_i, and the final wave, ψ_f, of wavelength λ_f, describing a neutron scattering off a single nucleus. The area, dA, for measuring the flux of the outgoing neutrons is the detector area as sketched. From [17].

The neutron comes in with wave vector k_i, most of the wave will continue but a tiny part will scatter as a spherical wave. A plane wave describes the incoming (or initial) neutron as

$$\psi_i(\vec{r}) = \frac{1}{\sqrt{Y}} e^{i\vec{k}_i\cdot\vec{r}} \tag{2.11}$$

where Y is a normalization constant. The time dependence $e^{-i\omega t}$ has no role until the inelastic scattering discussion will be explored in later chapters, therefore it has been neglected.

Considering the idealized situation illustrated in Fig. 2.4 where a neutron scattered by a single nucleus, labeled j, which is at a fixed in position. The scattered neutron can be described as a spherical wave leaving the nucleus, which is centered at r_j. Therefore the scattered, or final, wave is

$$\psi_f(\vec{r}) = \psi_i(\vec{r}_j) e^{i\vec{k}_f|\vec{r}-\vec{r}_j|} \frac{b_j}{|\vec{r}-\vec{r}_j|} \tag{2.12}$$

where b_j is a quantity characteristic for the particular isotope. Since b_j has the unit of length, it is usually denoted scattering length and is typically of the order $1-10$ fm. This above equation is valid only for $|\vec{r}$ - $\vec{r}_j| \gg b_j$, "far" from the nucleus.

The detector has an area $dA = \vec{r}^2 d\Omega$. Since the scattering cross section is the final aim of the calculation, the flux is a necessary quantity to move in this direction. If a volume element is taken $dAdL$ in the incoming neutron wave, then the number of neutrons per second, therefore the incoming neutron flux, is defined as

$$\psi = \frac{dN}{dt}\frac{1}{dA} = \frac{|\psi_i|^2\, dAdL}{dL/\vec{v}}\frac{1}{dA} = \vec{v}|\psi_i|^2 = \frac{\hbar\vec{k}_i}{m}\frac{1}{Y} \tag{2.13}$$

Taking into account the outgoing wave function, the number of scattered neutrons in $d\Omega$ per second is

$$\vec{v}|\psi_f|^2 dA = \frac{\hbar k_f}{m}\frac{1}{Y}\frac{b_j^2}{r^2}dA = \frac{\hbar k_f}{m}\frac{1}{Y}b_j^2 d\Omega \tag{2.14}$$

which is valid only where $\vec{r} \gg \vec{r}_j$.
The definition of the differential scattering cross section for one nucleus is given by

$$\frac{d\sigma}{d\Omega} = \frac{\frac{\hbar\vec{k}_f b_j^2 d\Omega}{mY}}{d\Omega}\frac{mY}{\hbar\vec{k}_i} = \frac{\vec{k}_f}{\vec{k}_i}b_j^2 = b_j^2 \tag{2.15}$$

where $\vec{k}_i = \vec{k}_f$, by assuming that the energy is conserved, therefore the energy of the neutron is unchanged. This is the so-called elastic scattering.

2.4 Scattering from two nuclei - interference

If a new nucleus ($\vec{r}_{j'}$) is added to the previous picture, again placed at fixed position, new spherical waves will appear and interfere. The neutron wave is described to be from one single neutron but it is the wave function that scatters from two different nuclei at the same time.
Denoting the nuclear scattering lengths as b_j and $b_{j'}$, the final wave function, coming out of the two nuclei can be defined as

$$\psi_f(\vec{r}) = \psi_i(\vec{r}_j)e^{i\vec{k}_f|\vec{r}-\vec{r}_j|}\frac{b_j}{|\vec{r}-\vec{r}_j|} + \psi_i(\vec{r}_{j'})e^{i\vec{k}_f|\vec{r}-\vec{r}_{j'}|}\frac{b_{j'}}{|\vec{r}-\vec{r}_{j'}|} \tag{2.16}$$

The equation for the neutron reaching the detector is the same as before

$$\begin{aligned} \#\ \text{neutrons per second into } d\Omega &= \vec{v}|\psi_f|^2 dA \\ &= \frac{\hbar k_f}{mr^2}\frac{1}{Y}\left|e^{i\vec{k}_i\vec{r}_j}e^{i\vec{k}_f|\vec{r}-\vec{r}_j|}b_j e^{i\vec{k}_i\vec{r}_{j'}}e^{i\vec{k}_f|\vec{r}-\vec{r}_{j'}|}b_{j'}\right|^2 dA \end{aligned} \tag{2.17}$$

using again the approx that $\vec{r} \gg \vec{r}_j$.
After writing the nuclear coordinate r_j as the sum of parallel and perpendicular component to r and checking that the perpendicular component is by far the

smallest and vanishes to first order (formal proof on the notes [17]), only one component of the nuclear coordinate, $r_{j,||}$ is used in the calculation, it is possible to obtain

$$\begin{aligned}&\frac{\hbar k_f}{mr^2}\frac{1}{Y}\left|e^{i\vec{k}_i\cdot\vec{r}_j}e^{i\vec{k}_f\cdot(\vec{r}-\vec{r}_j)}b_j e^{i\vec{k}_i\cdot\vec{r}_{j'}}e^{i\vec{k}_f\cdot(\vec{r}-\vec{r}_{j'})}b_{j'}\right|^2 dA = \\ &= \frac{\hbar k_f}{mr^2}\frac{1}{Y}\left|e^{i\vec{k}_f\cdot\vec{r}}\right|^2\left|e^{i\vec{k}_i-\vec{k}_f\cdot\vec{r}_j}b_j + e^{i\vec{k}_i-\vec{k}_f\cdot\vec{r}_{j'}}b_{j'}\right|^2 dA\end{aligned} \tag{2.18}$$

There is a common factor of $e^{i\vec{k}_f\cdot\vec{r}}$ which is a phase that depends on the position of the detector. By substituting the scattering vector in the previous equation and by recognizing that $\left|e^{i\vec{k}_f\cdot\vec{r}}\right|^2 = 1$, the eq. (2.18) becomes

$$\frac{\hbar k_f}{mr^2}\frac{1}{Y}\left|e^{i\vec{q}\cdot\vec{r}_j}b_j + e^{i\vec{q}\cdot\vec{r}_{j'}}b_{j'}\right|^2 dA \tag{2.19}$$

For simplicity it is possible to assume $b_j = b_{j'}$, then b_j^2 can vary between zero and four according to the phases. Two nuclei can scatter four times more than one nucleus therefore with N nuclei, it possible to scatter by N^2 more. In neutron scattering, it is essential to define interference between waves scattered from a large number of nuclei in the same way as it has been defined for two nuclei above. The principle of interference applies equally well to many particles as to two, therefore by generalizing the result to several particles, the elastic differential scattering cross section from nuclei is given by

$$\frac{d\sigma}{d\Omega} = \frac{\vec{k}_f}{\vec{k}_i}\left|\sum_j b_j e^{i\vec{q}\cdot\vec{r}_j}\right|^2 = \left|\sum_j b_j e^{i\vec{q}\cdot\vec{r}_j}\right|^2 \tag{2.20}$$

which is at the basis of the Neutron Scattering Technique, and can be calculated for particular structures.

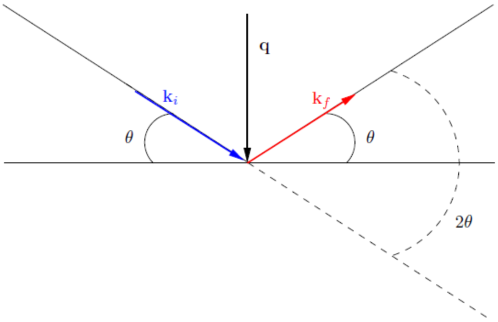

Figure 2.5: An illustration of the scattering process with the incoming and outgoing beam, the wave vectors, $\vec{k}_i$ and $\vec{k}_f$, and the scattering vector $\vec{q}$. From [17].

2.5 Coherent and Incoherent Scattering

Incoherence is defined as lack of coherence in scattering between different nuclei, this is due to the potentials or scattering amplitudes b that can vary in space and time. Scattering potential may depend upon the relative spin of the neutron and the spin of the nuclei that can randomly flip (unless at low T), these fluctuations might induce a variation in b_j. Another effect that could also vary b_j is the isotope variation.

The quantity b_j can be defined as an average plus a fluctuation that can vary in time and space

$$b_j \rightarrow \bar{b}_j + \delta b_j \tag{2.21}$$

To make the calculation more treatable, some approximations on time and space averages are done

$$\langle b_j \rangle = \bar{b}_j \tag{2.22}$$

$$\langle \delta b_j \rangle = 0 \tag{2.23}$$

$$\langle \delta b_i \delta b_j \rangle = 0 \tag{2.24}$$

Calculating the random fluctuations for two nuclei, the following result is observed

$$\begin{aligned} \langle \frac{d\sigma}{d\Omega}|_{n=2} \rangle &= \langle \left| (\bar{b}_j + \delta b_j) e^{i\vec{q}\cdot\vec{r}_j} + (\bar{b}_{j'} + \delta b_{j'}) e^{i\vec{q}\cdot\vec{r}_{j'}} \right|^2 \rangle = \\ &= \langle (\bar{b}_j + \delta b_j)^2 + (\bar{j}' + \delta j')^2 + (\bar{b}_j + \delta b_j)(\bar{b}_{j'} + \delta b_{j'})[e^{i\vec{q}\cdot(\vec{r}_j - \vec{r}_{j'})} + e^{-i\vec{q}\cdot(\vec{r}_j - \vec{r}_{j'})}] \rangle \\ &= \bar{b}_j^2 + < 2\bar{b}_j \delta b_j > + < \delta b_j^2 > + \bar{b}_{j'}^2 + < 2\bar{b}_{j'} \delta b_{j'} > + < \delta b_{j'}^2 > + \\ &+ \langle \bar{b}_j \bar{b}_{j'} + \bar{b}_j \delta b_{j'} + \bar{b}_{j'} \delta b_j + \delta b_j \delta b_{j'} \rangle [e^{i\vec{q}\cdot(\vec{r}_j - \vec{r}_{j'})} + e^{-i\vec{q}\cdot(\vec{r}_j - \vec{r}_{j'})}] \end{aligned} \tag{2.25}$$

where each average could be computed separately. It is useful to use the approximation defined in eq. (2.22, 2.23, 2.24). The value $\langle \delta b_j^2 \rangle$ is a randomly fluctuating term squared, which can be only positive.

$$\begin{aligned} \langle \frac{d\sigma}{d\Omega}|_{n=2} \rangle &= \bar{b}_j^2 + \bar{b}_{j'}^2 + \bar{b}_j \bar{b}_{j'} (e^{i\vec{q}\cdot(\vec{r}_j - \vec{r}_{j'})} + e^{-i\vec{q}\cdot(\vec{r}_j - \vec{r}_{j'})}) + \langle \delta b_j^2 \rangle + \langle \delta b_{j'}^2 \rangle \\ &= \left| \sum_i \bar{b}_i e^{i\vec{q}\cdot\vec{r}_j} \right|^2 + \sum_j \frac{\sigma_{inc,j}}{4\pi} \end{aligned} \tag{2.26}$$

where by definition $\langle \delta b_{j'}^2 \rangle = \frac{\sigma_{inc,j}}{4\pi}$. The incoherent scattering cross section $\sigma_{inc,j}$ is tabulated for each and every element and isotope, it represents a constant scattering

of neutrons, i.e. in all directions, without interference between scattering from neighbour atoms. The interesting part is the first term (coherence part) which will give the variation in scattering with the solid angle (interference) while the second term will scatter everywhere, each nucleus on its own, with no interference, and it comes from the assumption of uncorrelation. Incoherent scattering send out neutrons in all directions and it is responsible for the background.
One defines the coherent scattering cross section for a single nucleus j as $\sigma_{coh,j} = 4\pi\langle b_j\rangle^2$. The explicit average notation $\langle b_j\rangle$ is dropped, and the symbol b_j almost exclusively means the average scattering length of a certain isotope or element.

Chapter 3

Diffraction from Crystals

This chapter is mostly based on the Notes of the Neutron Scattering Course that I took at the University of Copenhagen, Niels Bohr Institute, by Kim Lefmann [17].

3.1 Introduction to crystals

A crystal is a substance in which the constituent atoms, molecules, or ions are packed in a regularly ordered, repeating three-dimensional pattern, forming a lattice. A lattice is an arrangement in space of isolated points (lattice points) in a regular pattern, showing the positions of atoms, molecules, or ions in the structure of a crystal. Lattice vectors connect two lattice points. Primitive lattice vectors are the shortest lattice vectors possible, three of them span the lattice space. All other lattice vectors can be expressed as a set of three indices that tell the indices of the vector sum that reproduces a particular lattice vector. In crystalline objects there is a long range order, a basic pattern of atoms is repeated over and over in three dimensions. Basic pattern can be made up of atoms or molecules or a building block of some other structure. The unit cell is the smallest repeating volume of the lattice. The volume of the unit cell is

$$V_o = \vec{a}(\vec{b} \times \vec{c}) \tag{3.1}$$

Any point in the lattice is given by a vector from the origin which is

$$\vec{r} = n_a\vec{a} + n_b\vec{b} + n_c\vec{c} \tag{3.2}$$

where n_a, n_b and n_c are integers. The angle between $\vec{a}$ and $\vec{b}$ is denoted γ, the angle between $\vec{b}$ and $\vec{c}$ is α and between $\vec{a}$ and $\vec{c}$ is β.

The reciprocal lattice vectors are defined as

$$\begin{aligned} \vec{a}^* &= \frac{2\pi}{V_o}\vec{b} \times \vec{c} \\ \vec{b}^* &= \frac{2\pi}{V_o}\vec{c} \times \vec{a} \\ \vec{c}^* &= \frac{2\pi}{V_o}\vec{a} \times \vec{b} \end{aligned} \tag{3.3}$$

It has the following properties:

$$\begin{aligned} \vec{a}^* \cdot \vec{a} = 2\pi \\ \vec{a}^* \cdot \vec{b} = 0 \end{aligned} \tag{3.4}$$

where the reciprocal lattice vectors are perpendicular to two of the three real space vectors. On the reciprocal lattice space it is possible to define any point as

$$\vec{\tau}_{hkl} = h\vec{a}^* + k\vec{b}^* + l\vec{c}^* \tag{3.5}$$

where h,k and l are integers.

Bravais lattice has exactly one atom per unit cell. Non Bravais lattice there are more than one atom per unit cell. Position of i-th atom in the jth unit cell is $\vec{r}_{ij} = \vec{r}_j + \vec{\Delta}_i$ with $\vec{r}_j$ the position of the jth lattice point and $\vec{\Delta}_i$ the displacement within the unit cell of that atom.

There are a number of geometrical symmetries to assign to the lattice, the translation invariance is present but they can also have mirror symmetry, rotational invariance etc. There are 7 different crystal groups and they fulfil different criteria that are described in Table 3.1.

Crystal system	Lattice vectors	Mimimum symmetry	Crystal classes	Crystal lattices	# space groups
Cubic	$a = b = c$, $\alpha = \beta = \gamma = 90°$	Four 3 or $\bar{3}$	23 m3 432 $\bar{4}$3m m3m	P I F	36
Hexagonal	$a = b \neq c$ $\alpha = \beta = 90°$, $\gamma = 120°$	One 6 or $\bar{6}$	6 $\bar{6}$ 6m 622 6mm $\bar{6}$2m 6/mmm	P	27
Trigonal	$a = b = c$, $\alpha = \beta = \gamma \neq 90°$	One 3 or $\bar{3}$	3 $\bar{3}$ 32 3m $\bar{3}$m	P (R)	25
Tetragonal	$a = b \neq c$, $\alpha = \beta = \gamma = 90°$	One 4 or $\bar{4}$	4 $\bar{4}$ 4/m 422 4mm $\bar{4}$2m 4/mmm	P I	68
Orthorhombic	$a \neq b \neq c$, $\alpha = \beta = \gamma = 90°$	Three 2 or $\bar{2}$	222 2mm mmm	P C (A,B) I F	59
Monoclinic	$a \neq b \neq c$, $\alpha = \gamma = 90°$	One 2 or $\bar{2}$	2 m 2/m	P C (I)	13
Triclinic	(none)	1 or $\bar{1}$	1 $\bar{1}$	P	2
Total: 7			32	14 independent	230

Table 3.1: An overview over the crystal systems, their properties, the corresponding crystal lattices, crystal classes, and their distribution of space groups. From [25].

3.2 Scattering from crystals and Bragg law

The differential cross section from nuclear scattering is given by:

$$\frac{d\sigma}{d\Omega} = \left|\sum_j b_j e^{i\vec{q}\cdot\vec{r}_j}\right|^2 \tag{3.6}$$

where the sum is done over all atoms.
By inserting the crystal, there is the need to sum over all unit cells (j) and sum over the atoms within that unit cell (i), the b can only depend on the position within the unit cell because all unit cells are necessarily identical and using equation $\vec{r}_{ij} = \vec{r}_j + \vec{\Delta}_i$, eq. (3.6) becomes

$$\begin{aligned} \frac{d\sigma}{d\Omega} &= \left|\sum_j \sum_i b_i e^{i\vec{q}\cdot\vec{r}_j} e^{i\vec{q}\cdot\vec{\Delta}_i}\right|^2 \\ &= \left|\sum_j e^{i\vec{q}\cdot\vec{r}_j}\right|^2 \left|\sum_i b_i e^{i\vec{q}\cdot\vec{\Delta}_i}\right|^2 \end{aligned} \tag{3.7}$$

More information on the symmetry is needed on the specific crystal to calculate further. The second term of the equation (3.7) which contain a sum over all atomic positions in the unit cell is called the nuclear structure factor $|F_N(\vec{q})|^2$. The intensity of the scattering is proportional to $|F_N(\vec{q})|^2$, the height of the peaks from the scattering reflects the nuclear structure factor.
Focusing on the first term, also called the lattice sum, further calculations can be done

$$\begin{aligned} \left|\sum_{j=1}^{N} e^{i\vec{q}\cdot\vec{r}_j}\right|^2 &= \sum_{j=1}^{N}\sum_{j'=1}^{N} e^{i\vec{q}\cdot\vec{r}_j} e^{-i\vec{q}\cdot\vec{r}_{j'}} \\ &= \sum_{j=1}^{N}\sum_{j-j'=1}^{N} e^{i\vec{q}\cdot(\vec{r}_j-\vec{r}_{j'})} \\ &= N\sum_{j-j'=1}^{N} e^{i\vec{q}\cdot(\vec{r}_j-\vec{r}_{j'})} \\ &= N\sum_{j=1}^{N} e^{i\vec{q}\cdot(\vec{r}_j)} \end{aligned} \tag{3.8}$$

This is an equation of the form $|x^2| = N|x|$ which will have 2 solutions, N if the phase stay constant to modulo 2Ω and zero if the phase shift around. The first requirement is the same as saying that $\vec{q}$ is a reciprocal lattice vector.

$$x = \begin{cases} 0 & = N\delta_{\vec{q},\vec{\tau}} \\ N \end{cases} \tag{3.9}$$

This is the only case in which the lattice sum is different from zero, the only place in $\vec{q}$ space where there is diffraction is on the reciprocal lattice points.
The distance between the lattice planes is $d = \frac{2\pi}{|b^*|}$ for a general τ, $d_\tau = \frac{2\pi}{|\vec{\tau}|}$.
From eq. (3.9), it is possible to see that $|\vec{q}| = |\vec{\tau}|$ which means that length of $\vec{q}$ and the length of τ (reciprocal lattice vector) are the same. This is equivalent to the Bragg law.

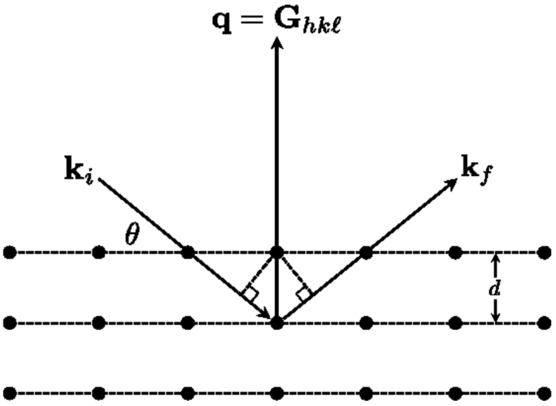

Figure 3.1: Diffraction in Bragg geometry. The incoming and outgoing wave vectors are $\vec{k}_i$ and $\vec{k}_f$, respectively, $\vec{q}$ is the scattering vector, and $\vec{d}$ is the relevant lattice spacing in the crystal. The incoming and outgoing angles are equal. From [26].

From Fig. 3.1 it is observed that

$$\begin{aligned} \vec{q} &= \vec{\tau} \\ 2k_i sin(\theta) &= n\frac{2\pi}{d} \\ 2\frac{2\pi}{\lambda} sin(\theta) &= n\frac{2\pi}{d} \\ 2d sin(\theta) &= n\lambda \end{aligned} \tag{3.10}$$

which is the Bragg law.

3.3 Vibrations of the atoms and scattering

If the position of the atoms is time dependent, it is possible to define

$$\vec{R}_j(t) = \vec{r}_j + \vec{U}_j(t) \tag{3.11}$$

where $\vec{U}_{ij}(t)$ is the vibration of the atoms and the average $\langle \vec{U}_j(t) \rangle = 0$ because it is a vibration around the lattice point.
From the differential cross section

$$\begin{aligned} \frac{d\sigma}{d\Omega} &= \langle \left| \sum_j b_j e^{i\vec{q}\cdot\vec{R}_j(t)} \right|^2 \rangle \\ &= \langle \sum_j \sum_{j'} b_j b_{j'} e^{i\vec{q}\cdot\vec{R}_j(t)} e^{-i\vec{q}\cdot\vec{R}_{j'}(t)} \rangle \\ &= \langle \sum_j \sum_{j'} b_j b_{j'} e^{i\vec{q}\cdot\vec{r}_j} e^{-i\vec{q}\cdot\vec{r}_{j'}} e^{i\vec{q}\cdot\vec{U}_j(t)} e^{-i\vec{q}\cdot\vec{U}_{j'}(t)} \rangle \end{aligned} \tag{3.12}$$

The $U(t)$ are less than a fraction of an Ångström (Å) so it is possible to Taylor expand expression (3.12).

$$\frac{d\sigma}{d\Omega} = \langle \sum_j \sum_{j'} b_j b_{j'} e^{i\vec{q}\cdot\vec{r}_j} (1 + i\vec{q}\cdot\vec{U}_j - \frac{(\vec{q}\cdot\vec{U}_j)^2}{2})(1 - i\vec{q}\cdot\vec{U}_{j'} - \frac{(\vec{q}\cdot\vec{U}_{j'})^2}{2}) \rangle \tag{3.13}$$

And because of $\langle \vec{U}_j(t) \rangle = 0$, everything with $U(t)$ to the first power vanish

$$\frac{d\sigma}{d\Omega} = \sum_j \sum_{j'} b_j b_{j'} e^{i\vec{q}\cdot\vec{r}_j} (1 - \langle (\vec{q}\cdot\vec{U}_j)^2 \rangle - \langle (\vec{q}\cdot\vec{U}_j)(\vec{q}\cdot\vec{U}_{j'}) \rangle \tag{3.14}$$

Assuming that on average U_j and $U_{j'}$ are uncorrelated, meaning that the fluctuation at j is not depending on fluctuation on j' then the term $\langle (\vec{q}\cdot\vec{U}_j)(\vec{q}\cdot\vec{U}_{j'})) \rangle$ average to zero.

$$\frac{d\sigma}{d\Omega} = \sum_j \sum_{j'} b_j b_{j'} e^{i\vec{q}\cdot\vec{r}_j} \langle 1 - (\vec{q}\cdot\vec{U}_j)^2 \rangle \tag{3.15}$$

If more terms would have been taken in the expansion, it would be possible to recognize that $\langle 1 - (\vec{q}\cdot\vec{U}_j)^2 \rangle = e^{-\langle (\vec{q}\cdot\vec{U}_j)^2 \rangle}$ which is the vibrational term, a lowering of the scattering amplitude due to vibrations, also known as Debye Waller factor, for convention written as e^{-2W}. At T=0, it is very close to one and when the temperature increases, it begins to drop until falling to zero around the melting point.

Therefore the differential cross section becomes

$$\begin{aligned} \frac{d\sigma}{d\Omega} &= \left|\sum_j e^{i\vec{q}\cdot\vec{r}_j}\right|^2 \left|\sum_i b_i e^{i\vec{q}\cdot\vec{\Delta}_i}\right|^2 e^{-2W} \\ &= \left|\sum_j e^{i\vec{q}\cdot\vec{r}_j}\right|^2 \left|F_N(\vec{q})\right|^2 e^{-2W} \end{aligned} \tag{3.16}$$

where $\left|\sum_i b_i e^{i\vec{q}\cdot\vec{\Delta}_i}\right|^2 = |F_N(\vec{q})|^2$.

3.4 Theory of diffraction

From the previous calculations in eq. (3.16), the differential cross section has been derived as function of the structure factor, where the first term $\left|\sum_{j=1}^{N} e^{i\vec{q}\cdot\vec{r}_j}\right|^2$ is equal to $N^2 \sum_{\vec{\tau}} \delta_{\vec{q},\vec{\tau}}$ so that if $\vec{q}$ is a reciprocal lattice vector then it gives N^2 otherwise zero. On the atomic scale this is true, on the global scale, it scatters as N, linearly, as when N becomes large (real crystals), the distribution becomes very high and sharp and the integrated intensity under the curve becomes proportional to N. The second term is $\left|\sum_i b_i e^{i\vec{q}\cdot\vec{\Delta}_i}\right|^2 = |F_N(\vec{q})|^2$, the nuclear structure factor squared which is the Fourier transform of the atoms in the unit cell weighted by their scattering length and the third term is e^{-2W}, the Debye Waller factor which is approximately 1.

In order to make the delta function more mathematically treatable when working with continuous variables it is possible to write

$$\begin{gathered} \sum_{j=1}^{N} e^{i\vec{q}\cdot\vec{r}_j} = c \sum_{\vec{\tau}} \delta(\vec{q}-\vec{\tau}) \\ \sum_{j=1}^{N} \int_{BZ} e^{i\vec{q}\cdot\vec{r}_j} d^3\vec{q} = c \sum_{\vec{\tau}} \int_{BZ} \delta(\vec{q}-\vec{\tau}) d^3\vec{q} \\ \frac{2\pi}{V_o} = c \end{gathered} \tag{3.17}$$

where one Brillouin zone is the same as one of the cells of the reciprocal lattice and integrating the delta function over all space gives one. V_o is the volume of the reciprocal unit cell.

If $\vec{r}_j$ is any lattice point then the complex phase would rotate around when $\vec{q}$ varies. It is a propriety of the Brillouin zone that the integral would vanish completely unless $\vec{r}_j = 0$. A formal proof is present on the notes [17].

τ can rotate all over the solid angle but it will scatter only when the Bragg law is fulfilled. This can happen in many different directions depending on the orientation of the crystal forming a cone like in Fig. 3.2. It is difficult to calculate but not too difficult to visualize especially with powder where the crystallites have all different orientations, therefore no matter the orientation, the whole scattering cone will be visible.

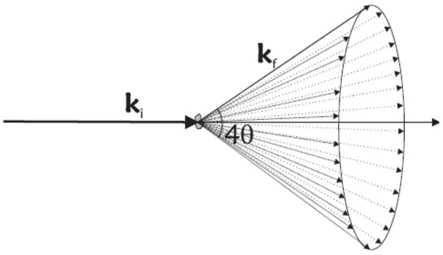

Figure 3.2: Illustration of the Debye-Scherrer cone for the diffraction from one powder line. From [17].

The differential cross section becomes

$$\frac{d\sigma}{d\Omega} = |F_N(\vec{q})|^2 e^{-2W} N \frac{(2\pi)^3}{V_o} \sum_{\vec{\tau}} \delta(\vec{q}-\vec{\tau}) \tag{3.18}$$

If there are crystallites everywhere, it is possible to do the integration over the solid angle. This will give the total scattering power for one particular τ:

$$\sigma_{\vec{\tau}} = |F_N(\vec{q})|^2 e^{-2W} j_{\vec{\tau}} \frac{N}{V_o} \frac{\lambda^3}{sin(\theta)} \tag{3.19}$$

where $j_{\vec{\tau}}$ is the multiplicity. So that if there is more than one scattering vector that has the same length, they cannot be separated in the experiment. Instead they are added up, therefore the number of equal τ is present in expression (3.19). θ is half the scattering angle. The λ^3 term comes from manipulation of the delta function (formal proof on the notes [17]).

When doing an experiment, from measuring the total scattering of one ring, it is possible to know a combination of $|F_N(\vec{q})|^2 j_{\vec{\tau}} \frac{1}{sin(\theta)}$ as usually the wavelength, the N and V_o are constant. By measuring many rings that comes from the scattering on different lattice planes, from the relative intensity and position it is possible to reconstruct what the crystal structure is.

3.5 Diffraction instrumentation

A reactor source produces the neutrons, the moderator slows them down and the neutron guide make sure that the neutrons are transported to the instrumentation. The monochromator (a crystal where the $\vec{d}$ spacing is known) selects one particular λ. The slit determines the scattering angle. Collimators are also used to improve the resolution, they absorb neutrons with the wrong direction.
From the Bragg law

$$n\lambda = 2d_m sin(\theta_m) \tag{3.20}$$

by determining θ_m (d_m is known), it is possible to derive λ. The neutrons hit the sample (powder) and scatter out in Debye-Scherrer cones (see Fig. 3.2).
Another option, used in a TOF source, is to have a chopper that determine the time of flight that will then determine the λ.
The detectors, positioned after the sample, measure at many scattering angles at the same time. Not all the cone is covered because of the limited height of the detectors. This is taken into account in programs that fit the resulting data.

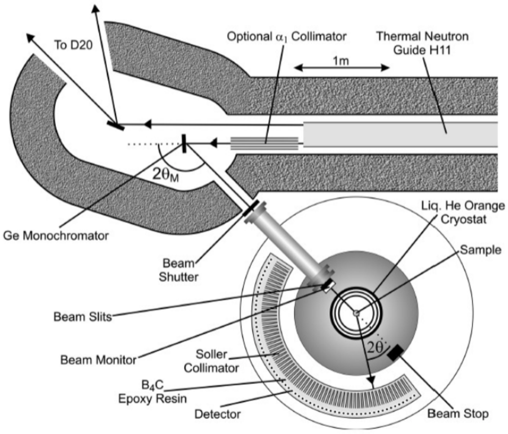

Figure 3.3: Example of Diffraction Instrument, D2B diffractometer at ILL, Grenoble. From [27].

Often, in order to avoid scattering from the container and vacuum chamber around the sample, a radial collimator is employed, so that neutrons that arrive from the side are not able to get through. Only if they arrive from the center, they get through. This improves the background noise, which is usually high as neutrons scatter from anything they encounter on their way.
The spectrum obtained can be plotted as function of $\vec{q}$ or 2θ and it shows lots of peaks that get more smeared at increasing θ as effect of the resolution of the

instrument.

3.6 Powder Diffraction

It is always possible to calculate the scattering cross section from a structure made by some atoms by taking some of the scattering powder and taking into account the positions. In crystalline lattice, as it is an ordered structure, the position is not relevant; therefore the scattering cross section, seen in eq. (3.7), can be separated into the lattice sum and the nuclear structure factor (sum over atoms in the unit cell). For the lattice sum, only if $\vec{q} = \vec{\tau}$ then there is a lattice sum different from zero. So the only place in q space where there is diffraction is on the reciprocal lattice points, as shown in eq. (3.9). This is exactly equal to the Bragg law, derived in eq. (3.10).
Rewriting the structure factor with $\vec{q} = \vec{\tau}$

$$F_{hkl} = \sum_{i}^{N} b_i \cdot e^{2\pi i(h\vec{x}_i + k\vec{y}_i + l\vec{z}_i)} \tag{3.21}$$

where there are the fractional coordinates in the unit cell (from the origin of the unit cell).
It is important to know where in the q space there is scattering, and it allows to calculate the structure factor when it is proportional to the intensity of the Bragg peak.

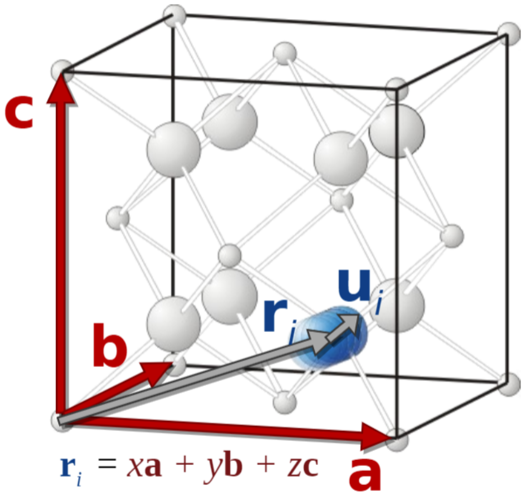

Figure 3.4: Illustration of the crystal unit cell. From [28].

When looking at the information given by the Bragg peak, the position in q space is given by the reciprocal lattice vector, which is determined by the size and symmetry of the unit cell because the position, which is given by τ, is related to the reciprocal lattice vectors. The peak intensity is depending on the structure factor, that is only determined by the content of the unit cell.
In single crystal experiment, the crystal is put in front of the beam and it can be rotated until a reciprocal lattice point is found that satisfy diffraction condition and spots on the detector are shown. The intensity of the Bragg peaks is proportional to the structure factor and the peak positions indicate the unit cell and symmetry. Diffraction can be done both either with X-rays and neutrons. Most of the diffraction measurements are done with X-rays. For single crystal it is used to determine the structure.

$$I_{hkl} = |F_{hkl}|^2 \tag{3.22}$$

In a powder there is a very large number of small crystallites that are completely randomly oriented with respect to each other so instead of spots, on the detector, rings are shown.
Isotropic powder diffraction data collected in 2D are usually integrated to 1D. So the rings are seen as peaks in order to see the different peaks' intensity. The intensity is given by

$$I_{hkl} = \frac{I_o \cdot \lambda^3 \cdot l_s}{8\pi r} \frac{L \cdot V_s \cdot j_{hkl}}{V_o^2} |F_{hkl}|^2 \tag{3.23}$$

where:

- I_o incoming neutron intensity
- λ neutron wavelength
- l_s constant related to detector coverage
- r sample-to-detector distance
- j_{hkl} multiplicity of reflection hkl
- V_o volume of the unit cell
- L Lorentz factor= $\frac{1}{\sqrt{1-\frac{v^2}{c^2}}}$
- V_s volume of the sample

It is derived on the notes [17]. Notice that $NV_c = V_s$ was already used in eq. (3.19). All parameters that are not dependent on scattering angle and crystal structure are grouped into one scale factor

$$I_{hkl} = S \cdot L \cdot j_{hkl} \left|F_{hkl}\right|^2 \tag{3.24}$$

All information about the content of the unit cell is in the structure factor for a given Bragg peak hkl, with the Debye-Waller factor taken into account

$$F_{hkl} = \sum_{i=1}^{N} b_i \cdot e^{2\pi i(h\vec{x}_i + k\vec{y}_i + l\vec{z}_i)} \cdot e^{\frac{-\vec{q}^2 \cdot \langle \vec{u}_i^2 \rangle}{2}} \tag{3.25}$$

It can also be rewritten as

$$F_{hkl} = \sum_{i=1}^{N} b_i \cdot e^{2\pi i(hx_i + ky_i + lz_i)} \cdot e^{-2B_i(\frac{sin\theta}{\lambda})^2} \tag{3.26}$$

where $B_i = 8\pi\langle\vec{u}^2\rangle$.
In general, looking at the effect of temperature, the intensity will drop with increasing temperature (higher exponential of the thermal factor), especially with the increasing of q (or θ). At high T, peaks will move to lower q values because of thermal expansion of the unit cell. To get a very high quality powder diffraction to obtain very precise structure, it is good advantage to do it at lower T because then it shows higher intensity of the Bragg peaks even at high q values and that means that when looking at the structure, there are more data to refine and then one obtains a better idea of the atomic position in the unit cell.
Another important term is the Bragg peak width. The Bragg peak is not really a delta function as instrumental broadening is present, like beam divergence, wavelength distribution, so better the instrument, the more narrow the peaks but there will always be some width. Instrumental broadening limits the resolution and it is hard to separate peaks, and therefore it is harder to extract information from the structure factor. To see for example structure changes, there is the need to have narrow Bragg peaks (high resolution) to be able to determine the transition. There are also sample effects such as grain size that could influence the results.
To sum up the information in the powder pattern are:

- Bragg peak positions: Unit cell size and symmetry
- Bragg peak intensities: Unit cell content
- Bragg peak width: Micro- and nanostructure; size and strain in the crystal grains

Powder diffraction can be used for different analysis:

- fingerprint: check if what has been synthesize has the right structure
- structure solution
- structure refinement: measure a pattern, take a model that is close to the final structure and minimize the difference between them.

In this work, the diffraction technique has been used to study the unsolved structure of $LaPt_2Si_2$, in particular x-ray diffraction.

Chapter 4

Quantum Vibrations and Inelastic Scattering

This chapter is mostly based on the Notes of the Neutron Scattering Course that I took at the University of Copenhagen, Niels Bohr Institute, by Kim Lefmann [17].

4.1 Quantum mechanical description of scattering

Quantum mechanics is needed to describe the scattering in proper details and the inelastic scattering. Take as a reference the description in Fig. 2.4 in which there are plane waves coming in (k_i), a nucleus at position r_j and a final spherical wave (k_f). Plane waves is a good approximation if the assumption of being very far from the scattering center is used. Assuming there is a serie of states $|\vec{k}_i\rangle$ and $|\vec{k}_f\rangle$, in order for $|\vec{k}_i\rangle$ to scatter, the Hamiltonian is defined as $\hat{H} = \frac{p^2}{2m} + \hat{V}$ where the kinetic term (describing particle in free space) is summed to $\hat{V}$. This operator describes the scattering potential, it is in a very small range as nuclear forces act in a length scale of the order of femtometers. The potential from the jth nucleus can be approximated with a delta function, reasonable when the range of the interaction is much smaller than wavelength of the scattering: $\hat{V}_j = a\delta(\vec{r} - \vec{r}_j)$ with a proportional constant a that will be defined.
Writing the Fermi Golden Rule which describes the rate of states i going to states f, a transition probability, the following expression is obtained

$$W_{i \to f} = \frac{2\pi}{\hbar} \frac{dn}{dE_f} \left| \langle k_i | \hat{V} | k_f \rangle \right|^2 \delta(E_i - E_f) \tag{4.1}$$

where $\frac{dn}{dE_f}$ is the density of final states in energy. The term squared is the matrix element between the initial and final state and the interaction. Only states k_f that conserve energy are taken into account. We could calculate the density of states as

$$\frac{dn}{dE_f} = \frac{dn}{dV_k}\frac{dV_k}{dk_f}\frac{dk_f}{dE_f} \tag{4.2}$$

Using

$$V_k = \frac{4\pi}{3}k_f^3 \quad \text{and} \quad E_f = \frac{\hbar^2 k_f^2}{2m} \tag{4.3}$$

It is possible to derive

$$\frac{dV_k}{dk_f} = 4\pi k_f^2 \quad \frac{dE_f}{dk_f} = \frac{\hbar^2 k_f}{m} \quad \frac{dk_f}{dE_f} = \frac{m}{\hbar^2 k_f} \tag{4.4}$$

It is necessary to define boundary conditions, in order to so it is possible to imagine a huge box, with side $L \gg 1$ m, with real space volume $V = L^3 = Y$. It is needed to have wavelength which is an integer fraction of the size of the cube, $n\lambda = L$, or $k_x = n\frac{2\pi}{L}$ where n is a positive integer.
Therefore the following equations are obtained

$$\frac{dV_k}{dn} = \frac{2\pi}{L}^3 \quad \frac{dn}{dV_k} = \frac{L^3}{2\pi} \tag{4.5}$$

Giving

$$\frac{dn}{dE_f} = \frac{Y}{(2\pi)^3}4\pi k_f^2\frac{m}{\hbar^2 k_f} = \frac{Y}{2\pi^2}\frac{k_f m}{\hbar^2} \tag{4.6}$$

Substituting eq. (4.6) in eq. (4.1) and using the expressions for $|k_i\rangle$ and $|k_f\rangle$ already defined in (2.11) we obtain

$$\begin{aligned} W_{i\to f} &= \frac{2\pi}{\hbar}\frac{Y}{2\pi^2}\frac{k_f m}{\hbar^2}\frac{a^2}{Y^2}\left|\int e^{-i\vec{k}_f\cdot\vec{r}}e^{i\vec{k}_i\cdot\vec{r}}\delta(\vec{r}-\vec{r}_j)d^3\vec{r}\right|^2 \\ &= \frac{k_f m}{\hbar^2}\frac{a^2}{\pi}\frac{1}{Y}\left|e^{-i(\vec{k}_i-\vec{k}_f)\cdot\vec{r}}\right|^2 \end{aligned} \tag{4.7}$$

Recalling that the flux is the density times the velocity

$$\Psi = \langle\vec{k}_i|\vec{k}_i\rangle\vec{v} = \frac{1}{Y}\frac{\hbar k_i}{m} \tag{4.8}$$

The goal is to know how many neutrons will scatter in any direction (isotropic), therefore in $d\Omega$ the Fermi Golden Rule becomes

$$W_{i\to f}\Big|_{d\Omega} = \frac{2\pi}{\hbar}\frac{dn}{dE_f}\Big|_{d\Omega}\left|\langle\vec{k}_i|\hat{V}|\vec{k}_f\rangle\right|^2\delta(E_i-E_f)\frac{d\Omega}{4\pi} \tag{4.9}$$

Substituting the derived equation into the differential scattering cross section described in eq. (2.8), we obtain

$$\frac{d\sigma}{d\Omega} = \frac{Ym}{\hbar\vec{k}_i}\frac{1}{d\Omega}\frac{\vec{k}_f m a^2 d\Omega}{\hbar^2\pi Y 4\pi} = \frac{\vec{k}_f}{\vec{k}_i}\frac{m^2a^2}{\hbar^2(2\pi)^2} \tag{4.10}$$

In elastic scattering $|\vec{k}_i| = |\vec{k}_f|$. From the classical derivation (eq. (2.15)), it is known that the differential scattering cross section should be equal to b_j^2, this allows to derive the proportionality constant as $a = b_j\frac{\hbar^2 2\pi}{m}$.
Therefore by substituting the expression for a in the potential, the result for more than one nucleus is $\hat{V}_j = \sum_j b_j\frac{\hbar^2 2\pi}{m}\delta(\vec{r}-\vec{r}_j)$, also known as Fermi pseudo potential, and applying it in the Fermi Golden Rule, gives

$$W_{i\to f}|_{d\Omega} = \frac{k_f m}{\hbar^2}\frac{1}{\pi}\frac{1}{Y}\left|\sum_j b_j e^{-i(\vec{k}_i-\vec{k}_f)\cdot\vec{r}}\right|^2 \tag{4.11}$$

The result obtained are consistent with the classical derivation given in Chapter 2, in particular to the differential scattering cross section found in eq. (2.20).

4.2 Finding the expression for lattice vibrations

Neutrons can create excitations in materials. It is possible to detect the change in energy of the neutron and the scattering angle and thereby learning something about the excitation.
There are several types of motion in materials, motions of the nuclei. The vibrations considered here are the vibrations in the solid lattice. By considering the lattice with the lattice points and the basis, it is possible to use the same notation already defined in the section 3.3 where a nucleus can move from its equilibrium position as $\vec{R}_{ij}(t) = \vec{r}_j + \Delta_i + \vec{U}_{ij}(t)$ where Δ_i is the displacement within the unit cell, $\vec{U}_{ij}(t)$ its a small deviation needed. $\langle\vec{U}_{ij}\rangle = 0$ so that $\vec{r}_j + \Delta_i$ is the equilibrium position.
Assuming there is a potential energy coming from the chemical bondings, potential energy between ions in the lattice (in the Bravais lattice case, one atom per unit cell), it has the following expression

$$V_{jj'} = \frac{1}{2}k_{jj'}\left|\vec{U}_j-\vec{U}_{j'}\right|^2 \tag{4.12}$$

the interaction is quadratic in $\vec{U}$ with a minimum at the equilibrium position.

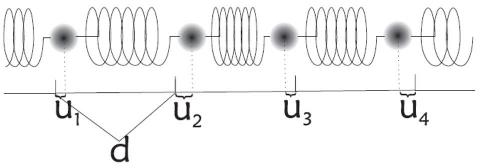

Figure 4.1: A classical illustration of a system showing lattice vibrations in one dimension. The description is done for a Bravais lattice, one atom per unit cell. From [17].

From Fig. 4.1, having masses (all equal) connected by springs, with spring constant all equal to k, result in a net force on the atoms. Assuming periodic boundary conditions then the force on a general nucleus j is

$$F_j = k(U_{j-1} + U_{j+1} - 2U_j) = M\frac{d^2U_j}{dt^2} \tag{4.13}$$

from Newton's second law.

There are N variables, therefore N differential equations to solve. Assuming periodicity in space it is possible to make an educated guess like

$$U_j = A_q e^{iaj\vec{q}} e^{-i\omega_q t} \tag{4.14}$$

the oscillation is periodic in time and space, a is the lattice constant. It is a wave in a discrete medium, oscillations are real so the part that will survive is the real part of the complex exponentials.

Plug the guessed solution in the equation (4.13)

$$\begin{aligned}
M\frac{d^2U_j}{dt^2} =& F_j = k(U_{j-1} + U_{j+1} - 2U_j) \\
M(-iw_q)^2 A_q e^{iaj\vec{q}} e^{-i\omega_q t} &= kA_q e^{iaj\vec{q}} e^{-i\omega_q t}(e^{-iaq} + e^{+iaq} - 2) \\
-Mw_q^2 U_j &= -2kU_j(1 - cos(aq)) \\
w_q^2 &= 4w_o^2 sin^2(\frac{aq}{2}) \\
w_q &= 2w_o \left| sin(\frac{aq}{2}) \right|
\end{aligned} \tag{4.15}$$

where w_o is the classical vibrational frequency from $w_o = \sqrt{k/M}$, w_q is a unique frequency.

In general, eq. (4.13) is a linear differential equation so any superposition will also solve the equation

$$U_j = \sum_q A_q e^{iaj\vec{q}} e^{-i\omega_q t} \tag{4.16}$$

Graphically, the dispersion relation of the vibrations is shown in Fig. 4.2, w_q vs $\vec{q}$, two quantities that are linked. This is sufficient information to classify the system.

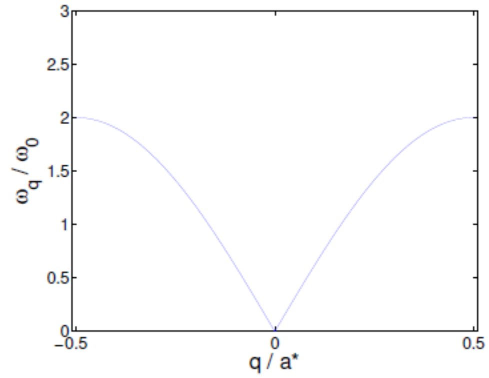

Figure 4.2: Dispersion relation for the nearest neighbour one-dimensional lattice model within one Brillouin zone. From [17].

From quantum mechanics, it is possible to derive the Hamiltonian of the system as

$$H = \sum_q (n_q + 1/2)\hbar w_q \tag{4.17}$$

where n is an integer. It is like an harmonic oscillator for many different modes. Each possible q will generate a mode, and the number of possible q is given by boundary conditions. If the Hamiltonian is solved quantum mechanically for finite T, the average energy of the system/vibrations is $\langle E\rangle = \sum_q (n_B + 1/2)\hbar w_q$ and the average number n for the harmonic oscillator in a thermal bath is the Bose number $n_B = \frac{1}{e^{\frac{\hbar\omega q}{k_B T}} - 1}$ which for low T is almost linear in T.

This term determine the thermal properties of solid, it is an important contribution in heat capacity. Motion of energy or heat transport is governed by phonons, they take energy from the warm part of the material to the cold part. Phonons are important to understand the thermal properties and thermal expansion of the material. More can be seen in [29].

From the boundary conditions it is possible to derive the possible values of q

$$\begin{aligned} e^{i\vec{a}\cdot\vec{q}N} &= 1 \\ \vec{a}\cdot\vec{q}N &= n2\pi \\ \vec{q} &= \frac{n}{N}\bar{a}^* \end{aligned} \tag{4.18}$$

Quantized lattice vibrations are known as phonons. The low frequency part is the sound, the dispersion reach zero linearly and sound is a combination of series of q.

It will propagate with a group velocity of signal $\frac{d\omega}{dq} = c$ with c as the velocity of sound. The low frequency part is of the order of Hz and kHz. At the top of the band is of order 1-10 THz.

Most of the materials are non Bravais lattices. The real space lattice unit cell doubles so the reciprocal space lattice is halved, therefore the drawing of the dispersion relation changes. The other part of the dispersion is still there, still physical but it is folded back, as seen in Fig. 4.3.

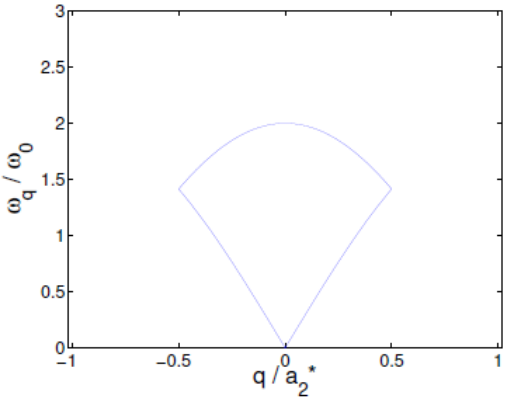

Figure 4.3: Dispersion relation for the nearest neighbour one-dimensional phonon model when the unit cell is doubled without change in the vibration physics. This means that the reciprocal lattice vector is halved with respect to the top panel, $a_2^* = a^*/2$. Note the occurrence of a low (acoustic) and a high (optical) branch. From [17].

If every second atom of Fig. 4.1 has a different mass, there will be a slight perturbation to the motion. The calculation includes twice as many differential equations, two guesses are needed for the motion and the result is that there is this an added part to the dispersion with a gap in between (detailed calculations are done in the notes [17]). In general there would be n modes where n is the number of atoms in the unit cell. All the modes that do not go to zero are called optical while the ones that go to zero are the acoustic, where the sound lives. The name optical comes from the fact that they can be probed with optical methods, light scattering, Raman scattering. Neutron scattering can probe the full dispersion and this is what it has been done in the experimental part.

Two of the most used programs to perform phonon calculations is three dimensions are VASP [30] and phonopy [31]. Generally, the two main steps are the structure relaxation and the phonon calculation. At first, the targeted structure is optimized, in this step it is important to define the k points in the three directions based on the lattice parameters in the unit cell and the ISYM parameter which determines the way VASP treat symmetry [30]. The relaxed structure is then used for the phonon calculations and there are two main methods to perform them: supercell method (finite-difference method) and density functional perturbation theory (DFPT). For this step, an open source package called phonophy is used for phonon calculations at harmonic and quasi harmonic level [31]. It has many features such as phonon band structure, phonon density of states or partial density of state, phonon thermal properties as free energy heat capacity and entropy, group velocity and many others.

U_j becomes a vector, there is polarization index (real space direction of the vibration) to the amplitude, there is a unit vector in the direction of the polarization.

$$\vec{U_j} = \sum_{q,p} A_{q,p} e^{iaj\vec{q}} e^{-i\omega_{q,p}t} \hat{U_j} \tag{4.19}$$

Vibrations can happen in different directions in 3 dimensions there are 3 polarization modes, there are two transverse and one longitudinal. Therefore in reality there will be $3n$ modes, there will be $3(n-1)$ optical modes, the acoustic will split to have 2 transverse acoustics and 1 longitudinal acoustic. Most of the vibration in the optical mode are atoms making counter vibrations inside the unit cell so it is not possible to say what is the direction at q close to zero.

4.3 Inelastic Scattering Theory

Here there is a derivation for the cross section for inelastic scattering in quantum mechanics. Some ingredients need to be included in the previous quantum picture seen in section 4.1, energy transfer is defined as

$$\hbar\omega = E_i - E_f \tag{4.20}$$

The behaviour is collective of the material, the state of the sample is labelled as λ_i and λ_f , before and after scattering.

The previous equations for the states $|k_i\rangle$ and $|k_f\rangle$ becomes equation for the whole systems, neutron plus the sample

$$\begin{aligned} |\lambda_i \vec{k_i}\rangle &= \frac{1}{\sqrt{Y}} e^{i\vec{k_i}\cdot\vec{r}} |\lambda_i\rangle \\ |\lambda_f \vec{k_f}\rangle &= \frac{1}{\sqrt{Y}} e^{-i\vec{k_f}\cdot\vec{r}} |\lambda_f\rangle \end{aligned} \tag{4.21}$$

The inelastic scattering cross section gives how many neutrons are going out in a direction with a particular energy

$$\frac{d^2\sigma}{d\Omega dE_f} = \frac{1}{\psi} \frac{\text{number of neutrons scattered into } d\Omega \text{ in } [E_f; E_f + dE_f]}{d\Omega dE_F} \tag{4.22}$$

Rewriting the Fermi Golden rule, the probability to go from an initial to a final state as

$$W_{i\to f}|_{d\Omega} = \frac{2\pi}{\hbar}\left|\langle\lambda_f\vec{k}_f|\hat{V}|\lambda_i\vec{k}_i\rangle\right|^2\frac{dn}{dE_f}\delta(E_{\lambda_i}+E_i-(E_{\lambda_f}+E_f))\frac{d\Omega}{4\pi} \tag{4.23}$$

with $\hat{V}_j = \sum\limits_j b_j\frac{\hbar^2 2\pi}{m}\delta(\vec{r}-\vec{r}_j)$.

Substituting it in eq. (4.22) and assuming the state of the sample before scattering is at thermal equilibrium, we do not calculate the full cross section but the trasition from a particular λ_i to a particular λ_f like

$$\begin{aligned}\left.\frac{d^2\sigma}{d\Omega dE_f}\right|_{\lambda_i\to\lambda_f} &= \frac{k_f}{k_i}(\frac{m}{2\pi\hbar^2})^2|\langle\lambda_f\vec{k}_f|\hat{V}|\lambda_i\vec{k}_i\rangle|^2\delta(E_{\lambda_i}-E_{\lambda_f}+\hbar\omega)\\ &= \frac{k_f}{k_i}|\sum_j b_j\langle\lambda_f|\int e^{-ik_f\cdot\vec{r}}\delta(\vec{r}-\vec{r}_j)e^{ik_i\cdot\vec{r}}d^3r|\lambda_i\rangle|^2\delta(E_{\lambda_i}-E_{\lambda_f}+\hbar\omega)\\ &= \frac{k_f}{k_i}|\sum_j b_j\langle\lambda_f|e^{i\vec{q}\vec{r}_j}|\lambda_i\rangle|^2\delta(E_{\lambda_i}-E_{\lambda_f}+\hbar\omega)\\ &= \frac{k_f}{k_i}\sum_j\sum_{j'}\langle\lambda_i|e^{-i\vec{q}\vec{r}_j}|\lambda_f\rangle\langle\lambda_f|e^{i\vec{q}\vec{r}_{j'}}|\lambda_i\rangle\delta(E_{\lambda_i}-E_{\lambda_f}+\hbar\omega)\end{aligned} \tag{4.24}$$

the energy that the neutron loses goes in the sample.
Using some mathematical identities like

$$\delta(a) = \frac{1}{2\pi}\int e^{ia}da \quad e^{i\frac{\hat{H}t}{\hbar}}|\lambda\rangle = e^{i\frac{Et}{\hbar}}|\lambda\rangle \quad and \quad \vec{R}_j(t) = e^{iHt/\hbar}R_je^{-iHt/\hbar} \tag{4.25}$$

We reach

$$\frac{d^2\sigma}{d\Omega dE_f} = \frac{1}{2\pi\hbar}\frac{k_f}{k_i}\int\sum_j\sum_{j'}b_jb_{j'}\langle\lambda_i|e^{-i\vec{q}\vec{r}_j}|\lambda_f\rangle\langle\lambda_f|e^{i\vec{q}\vec{r}_j}|\lambda_i\rangle e^{\frac{i(E_{\lambda_f}-E_{\lambda_i})t}{\hbar}}e^{-i\omega t}dt \tag{4.26}$$

The second part of the equation can be written as

$$\langle\lambda_f|e^{\frac{iE_{\lambda_f}t}{\hbar}}e^{i\vec{q}\vec{r}_j}e^{\frac{-iE_{\lambda_i}t}{\hbar}}|\lambda_i\rangle e^{-i\omega t}dt = \langle\lambda_f|e^{\frac{i\hat{H}t}{\hbar}}e^{i\vec{q}\vec{r}_j}e^{\frac{-i\hat{H}t}{\hbar}}|\lambda_i\rangle e^{-i\omega t}dt \tag{4.27}$$

where the position $\vec{r}_j$ is depending on the time, therefore $\vec{r}_j = \vec{R}_j(t)$ as denoted when calculating classical phonons.

The full equation becomes

$$\frac{d^2\sigma}{d\Omega dE_f} = \frac{1}{2\pi\hbar}\frac{k_f}{k_i}\int \sum_j \sum_{j'} b_j b_{j'} \langle\lambda_i|e^{-i\vec{q}\vec{R}_j(0)}|\lambda_f\rangle\langle\lambda_f|e^{i\vec{q}\vec{R}_{j'}(t)}|\lambda_i\rangle e^{-i\omega t}dt \tag{4.28}$$

where it is possible to sum over λ_f. Having $|\lambda_f\rangle\langle\lambda_f| = 1$, it is possible to take the thermal average over all λ_i, the thermal average of a general quantity a is $\langle a\rangle = \sum_j p_j\langle\lambda_j|a|\lambda_j\rangle$ therefore

$$\left.\frac{d^2\sigma}{d\Omega dE_f}\right|_{\lambda_i} = \frac{1}{2\pi\hbar}\frac{k_f}{k_i}\int \sum_j \sum_{j'} b_j b_{j'} \langle e^{-i\vec{q}\vec{R}_j(0)} e^{i\vec{q}\vec{R}_{j'}(t)}\rangle e^{-i\omega t}dt \tag{4.29}$$

Taking the special case of vibrations around an equilibrium position, the phonon approximation gives eq. (3.11), where $\vec{R}_j(t)$ is the sum of a static term and a small displacement. Using this phonon approximation, the inelastic scattering cross section becomes

$$\frac{d^2\sigma}{d\Omega dE_f} = \frac{1}{2\pi\hbar}\frac{k_f}{k_i}\int \sum_j \sum_{j'} b_j b_{j'} e^{-i\vec{q}\vec{r}_j} e^{i\vec{q}\vec{r}_{j'}} \langle e^{-i\vec{q}\vec{U}_j(0)} e^{i\vec{q}\vec{U}_{j'}(t)}\rangle e^{-i\omega t}dt \tag{4.30}$$

It is possible to make a classical calculation from eq. (4.30), where the displacements are very small, therefore the average is treatable with Taylor expansion, as $\langle e^{-i\vec{q}\vec{U}_j(t)}\rangle \approx 1 - i\vec{q}\vec{U}_j(t) - \frac{1}{2}(\vec{q}\vec{U}_j(t))^2$ which is the same approximation done in section 3.3 assuming the potential to be parabolic, so higher order terms are not taken into account.

It is assumed to have a Bravais lattice, all $b_j = b$, moreover $U_j(t)$ is assumed to be classical so that the eq. (3.11) is treated classically (writing $j' - j = \delta$). The lattice has translational symmetry, so the inelastic cross section cannot depend on j therefore the expectation value cannot depend on j.

$$\begin{aligned}\frac{d^2\sigma}{d\Omega dE_f} = N\frac{b_j^2}{2\pi\hbar}\frac{k_f}{k_i}\int \sum_\delta e^{i\vec{q}\vec{r}_\delta}\langle 1 + i\vec{q}\vec{U}_\delta(t) - \frac{1}{2}(\vec{q}\vec{U}_\delta(t))^2 - i\vec{q}\vec{U}_o(0) + \\ + (\vec{q}\vec{U}_o(0))(\vec{q}\vec{U}_\delta(t)) - \frac{1}{2}(\vec{q}\vec{U}_\delta(t))^2)\rangle e^{-i\omega t}dt\end{aligned} \tag{4.31}$$

Averaging over all configurations is the same as averaging over all phases of the phonons, therefore $\langle\vec{U}_o(0)\rangle = 0$, also using the assumption that if we would take into account orders greater than two, we would get $1 - (\vec{q}U_o(0))^2 \rightarrow e^{-\langle\vec{q}U_o(0))^2\rangle} \rightarrow e^{-2W}$. Substituting the Debye-Waller factor inside the expression would lead back to the differential cross section already seen previously, ω can be integrated out and will cancel with $\frac{1}{2\pi\hbar}$. The Debye-Waller factor is an attenuation, therefore diffraction decreases due to the motion, due to the phonons.

$$\frac{d^2\sigma}{d\Omega dE_f} = N\frac{b_j^2}{2\pi\hbar}\frac{k_f}{k_i}\int\sum_{\delta} e^{i\vec{q}\vec{r}_\delta}\langle(\vec{q}\vec{U}_o(0))(\vec{q}\vec{U}_\delta(t))\rangle e^{-i\omega t}dt \tag{4.32}$$

It is possible to define

$$\vec{U}_\delta(t) = \hat{e}A_k\mathbb{R}\{i\vec{k}\vec{r}_\delta e^{-i\omega_k t}e^{i\phi}\} \tag{4.33}$$

where $\hat{e}$ is a polarization vector, A_k is an amplitude, ϕ is an unknown phase, and the frequency w_k is of the phonon.
By substituting the expression for $\vec{U}_\delta(t)$ in the cross section equation, by averaging over ϕ, and defining the identities $\int e^{i(\omega_k-\omega)t}dt = 2\pi\delta(\omega_k-\omega)$ and $\sum_\delta e^{i(\vec{q}-\vec{k})\vec{r}_j} = N\delta(\vec{q}-\vec{k}+\vec{\tau})$, the result leads to

$$\frac{d^2\sigma}{d\Omega dE_f} = (q\hat{e})^2 N b_j^2\frac{k_f}{k_i}\frac{\langle A_k^2\rangle}{4}(\delta(\vec{q}-\vec{k}+\vec{\tau})\delta(\hbar\omega-\hbar\omega_k)+\delta(\vec{q}+\vec{k}+\vec{\tau})\delta(\hbar\omega+\hbar\omega_k)) \tag{4.34}$$

$\vec{q}$ is the phonon momentum transfer, $\vec{k}$ is the phonon momentum, $\delta(\vec{q}-\vec{k}+\vec{\tau})$ gives momentum conservation, while $\delta(\hbar\omega-\hbar\omega_k)$ gives energy conservation.
$\delta(\hbar\omega+\hbar\omega_k)$ imply that the neutron gains energy and $\delta(\vec{q}+\vec{k}+\vec{\tau})$ (phonon)momentum, and that the neutron absorbs a phonon. Term $\langle A_k^2\rangle$ is a thermal average, the amplitudes gets higher with the temperature increases, more phonons correspond to higher amplitude. In the quantum calculation case, everything is exactly the same except that $\langle A_k^2\rangle$ disappears (average thermal population). Moreover a factor $n_B(\frac{\hbar\omega_k}{k_BT})+1$ is present in front of the energy loss term (first deltas) and a factor $n_B(\frac{\hbar\omega_k}{k_BT})$ is present in front of the energy gain term (second deltas). In the energy gain, the neutron absorbs a phonon, however if the temperature is zero, there are no phonons, which implies that the cross section must be zero. In the energy loss, a phonon is generated at zero temperature, this is what gives the $'+1'$ (emission).

Chapter 5

Characterization of the $LaPt_2Si_2$ sample

5.1 Information about the sample

The single crystalline samples were synthesized by collaborators Prof. Zakir Hossain of the Indian Institute of Technology, Kanpur, India and Dr. Arumugam Thanizhavel of the Tata Institute of Fundamental Research, Mumbai, India. They have also performed the basic characterizations of the sample quality by using in house X-ray diffraction and bulk magnetic methods (structure, superconducting transition, etc.).

Until now, the vast majority of the results on this system have been reported only on polycrystalline samples [9, 12, 13], but the very recent synthesis of good quality single crystals allows further investigations to clarify the nature of the interplay between the CDW and SC in $LaPt_2Si_2$ [32]. The single crystals of $LaPt_2Si_2$ were grown using the Czochralski pulling method [32] by using high-purity elements La (99.9%), Pt (99.9%) and Si (99.9%). To optimize the conditions of the growth, a tungsten rod has been utilized and the crystal was pulled at a constant rate of 10 mm/h. In order to ensure that the crystal structure meet the requirement of a single-phase nature, powder X-ray diffraction (XRD, crushed single crystal) with Cu-K_α radiation has been performed.

Scanning electron microscopy (SEM) along with energy dispersive X-ray spectroscopy (EDX) were used to check the composition and homogeneity of the crystal. In addition, with the Laue X-ray diffraction it was possible to orient the crystal along the desired crystallographic direction, as will be shown in Chapter 8. With a spark erosion cutting machine, the initial crystal has been divided into 5 different pieces.

An overview of the structure parameters is given in Table 5.1 [32]. The final crystal used for the INS experiments was $\emptyset = 6$ mm, L = 21 mm, having a total mass $m = 3.9759 \pm 0.0002$ g. This high-quality piece was selected and cut out from a much larger single crystal, which is shown below in Fig. 5.1.

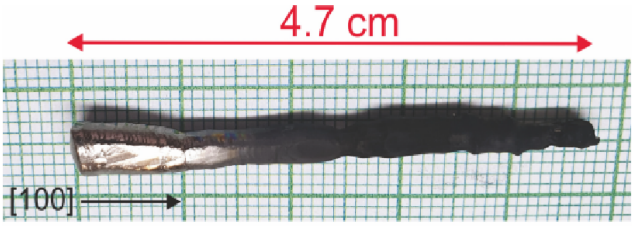

Figure 5.1: Our initial $LaPt_2Si_2$ crystal, before cutting, with the [100] direction along the crystal.

Structure	$CaBe_2Ge_2$-type tetragonal
Space group	P4/nmm
Lattice parameters	
a	4.285 (Å)
b	4.285 (Å)
c	9.831 (Å)
$\alpha = \beta = \gamma$	90°
V_{cell}	180.5 (Å^3)

Table 5.1: A general overview of the sample crystal information: structure, space group lattice parameters and volume of the primitive cell.

5.2 Study on resistivity

Several studies on the resistivity were done in previous works [1] [15] [33] [9] [12]. The measurement of the resistivity as function of temperature seen in Fig. 5.2 is in accordance with the previous literature. On the left it is possible to observe the superconducting nature of the material, as the resistivity has a sharp drop to zero below 1.6 K. It is possible to observe a transition around 100 K, related to the CDW. The measurement was done for both cooling and heating. The hysteresis in resistivity of $LaPt_2Si_2$ between cooling and heating data confirms the first order nature of the phase transition.

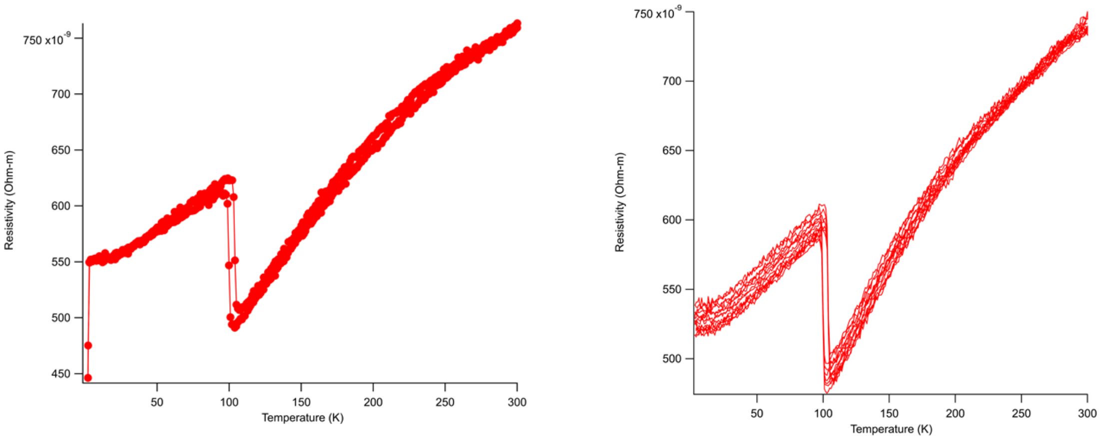

Figure 5.2: Resistivity measurements on $LaPt_2Si_2$ along the c axis for increasing and decreasing temperature. Right: magnetic field in the range 0.01 to 9 Tesla is applied.

The resistivity data were collected at Paul Scherrer Institute (PSI) by the PhD student Elisabetta Nocerino, KTH Royal Institute of Technology, Stockholm. The data have been collected using the equipment at Physical Properties of Materials lab at PSI with the support of Dr. Maria Luisa Medarde Barragan and PostDoc Klein Yannick Maximilian.

5.3 Raman scattering characterization

5.3.1 Motivation

There are no previous Raman measurement in the literature on $LaPt_2Si_2$. Theoretical calculations show that CDW and SC coexist in the (Si_2–Pt_1–Si_2) layer. Also the calculations of the phonon dispersions predict phonon-softening instabilities, which should lead to a structural instability that could be observed with Raman spectroscopy [7, 8]. The two peculiar mechanisms occuring in $LaPt_2Si_2$ are:

- $\sim$ 1.22 K the material becomes superconducting. The Fermi surface exhibits two gaps of different magnitude [13];
- $\sim$ 85 K CDW transition occurs. This is a first order structural transition. From the literature [1], the diffraction patterns show the occurrence of satellite Bragg peaks corresponding to the wave vector q $\approx$ [0.36, 0, 0)]. The satellites have their maximum intensity at 85 K, disappear above 175 K and almost vanish below 85 K [1].

Thanks to Raman spectroscopy across the CDW transition, it is possible to study the temperature evolution of the CDW and extract the magnitude of the electronic gap opened by the CDW at the Fermi surface Δ_{CDW} [34]. The CDW manifests itself as a modification of the shape of the peak of the Raman mode (i.e. broadening of FWHM, or reduction of the integrated intensity).
The knowledge of Δ_{CDW} is crucial to address several important questions such as if the CDW can be understood within a scenario of weakly interacting electrons, where the mean-field theory is used, or what is the relationship between CDW and SC that can be understood through a comparison of the magnitudes of their band gaps.
The aim is to determine the temperature dependence of the CDW order parameter by observing the frequency shifts of the lines in the Raman spectra as a function of temperature. The frequency shifts of the Raman lines are indeed proportional to the square of the CDW order parameter [35]. Moreover, it is possible to determine the magnitude of the Δ_{CDW} by observing the line widths of the Raman lines as a function of T. The FWHM of the Raman lines are related to the lifetime of the corresponding phonons. Similarly to what had been observed in the superconductors [36], the opening of a CDW gap at the Fermi surface prevents phonons with energies smaller than the gap from relaxing through the excitation of an electron. This results in an increase of the phonon's lifetime with a consequent narrowing of the corresponding Raman line.

5.3.2 Raman set up

Raman scattering consists in inelastic scattering of photons by matter. In general, a light beam scatter on a sample and it can be transmitted without any modification or it is absorbed (depending on the wavelength of the light and the nature of the sample). Most of the incident beam is scattered elastically, therefore with the same frequency as the incident photons but different direction, this is called the Rayleigh effect. Instead a smaller percentage of the light is scattered inelastically

(Raman effect), meaning that there is both an exchange of energy and a change in the light's direction: having an energy different (usually lower) from those of the incident photons [37].
Raman scattering can be thought of as a two photon process. The electrons have different vibrational levels, they are defined by specific energy differences. When an incident monochromatic light interacts with an electron in the sample, the electron absorbs energy from the incident photon and it raises to a virtual state of energy, see Fig. 5.3. The energy transferred is given by $E = h\nu_i$ with ν_i as frequency of incident photon. The electron then falls back to an energy level by losing energy. If the energy lost is equal to the energy of the incident photon then the electron falls back to its initial level and in this process emits another photon. Since the energy lost is equal to the energy of the incident photon, their frequency is the same (Rayleigh scattering).
Sometimes electrons when losing energy from the virtual state can fall back to a different vibrational level, in this case the energy lost by the electron is different from the energy absorbed from the incident photon. As a result the photon emitted by the electron has a different energy and therefore frequency (Raman scattering).

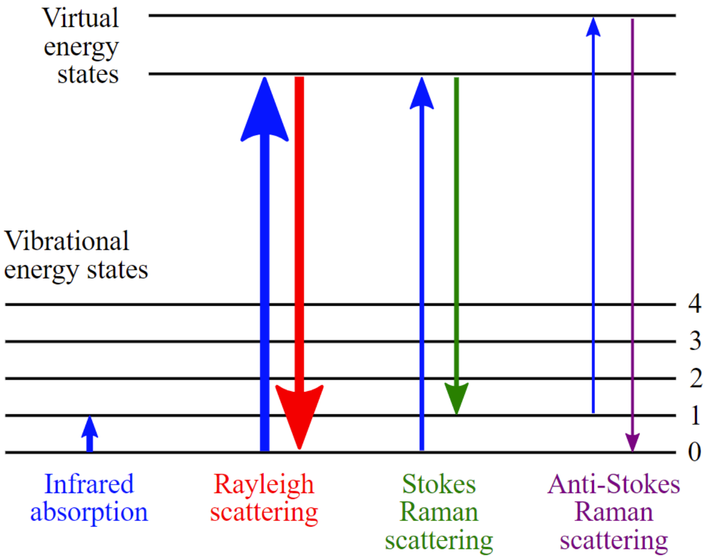

Figure 5.3: Energy-level diagram showing the states involved in Raman spectra. From [38].

Depending upon the final energy of the electron or the final vibrational level of the electron, Raman scattering can be separated into Stokes lines and Anti Stokes lines. If the frequency of the scattered photon is less than the frequency of the incident photon, Stokes lines are observed on Raman spectrum. This happens when electron absorbs energy. Similarly when frequency of emitted photon is greater than incident photon, Anti-stokes lines are observed, this means that energy is released by the electron [39].

The Raman spectra gives the structural fingerprint by which molecules can be identified. By studying the spectra one can identify the rotational levels and thus a particular molecule. The spectrum is used for material identification and analysis.

The measurements on Raman scattering has been done at Chalmers University, by Elisabetta Nocerino, PhD student at KTH with the support during the measurements of Ezio Zanghellini, Senior Research Engineer at Chalmers. The measurement conditions on the $LaPt_2Si_2$ single-crystal were:

- T range: 10 –300 K
- Wavelength: 514.531 nm
- Range: $\sim$ 0-600 cm^{-1}
- Instrument: Dilor XY 800
- Power: 60mW
- Detector: LN2-cooled CCD

In general in a light scattering set up, a source of monochromatic light, usually from a laser, is used, which is driven by the optics to the sample. The laser light interacts with molecular vibrations, phonons or other excitations in the system, resulting in the energy of the laser photons being shifted up or down. The shift in energy gives information about the vibrational modes in the system. After the sample there are other optics to gather the signal to the spectrometer. The photons are then seen with a photo detector.

The sample that has been used was a smaller piece (see insert in Fig. 5.4) compared to the one used in the INS scattering.

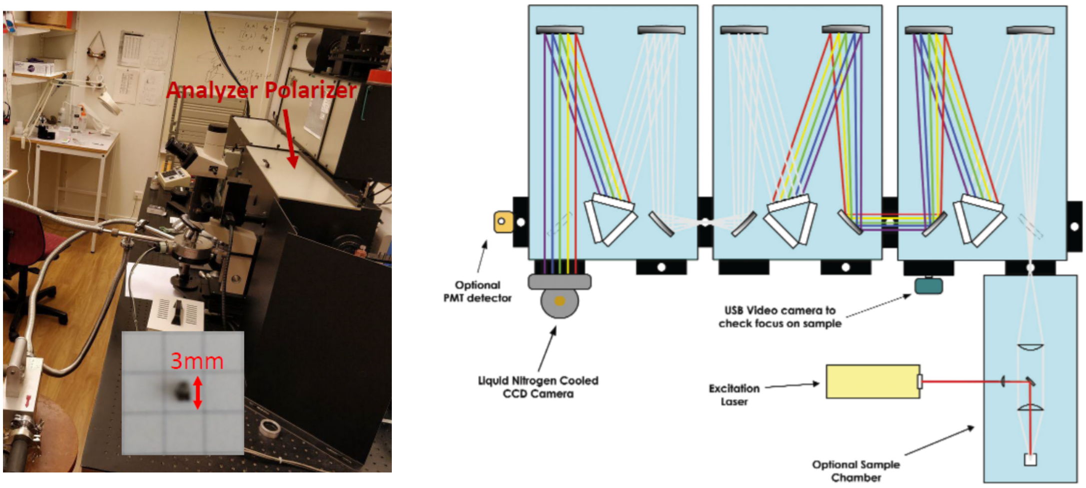

Figure 5.4: Left: Raman Instrumentation, Dilor XY 800 at Chalmers University (Göteborg). In the insert, it is possible to see the sample used during the experiment. Right: Typical Experimental Setup for Raman scattering. From [40].

A skectch of the instrumentation set up used during the experiment is seen in Fig. 5.4. Dilor XY 800 has different specificity that can be used, depending on the material analysed as seen in Fig. 5.5. CCD (charged-coupled device) is thermally cooled with liquid Nitrogen. A Glan–Taylor prism is used to polarize the light.

Instrument	Laser Lines [nm]	Sampling	RR Filters	Spectral Analysis	Detectors	Ranges [cm^{-1}]
Dilor XY 800	514.5 488 476.5 458	micro macro	DS	F800	CCD (L-N_2)	< 10
			DS St-aSt			∓ 10 ÷ ∓ 320
			notch	F300		< 80

Figure 5.5: Raman Instrumentation, Dilor XY 800 specifics.

Usually, the Rayleigh scattering is present, it is stronger than the Raman scattering, close to the laser line. This can be a problem as it might overfill some channels. In order to get rid of the Rayleigh scattering, Double subtractive (DS) spectrometer is used. The first 2 stages of the monochromator are acting as a big notch filter that allows just a certain amount of signal to go through, with a certain frequency. Then the intermediate slit cuts off some of the frequencies, only a notch goes through. After that, the frequencies are recombined so that the final notch go all through the final slit of the double subtractive system. The entrance and final slit define how sharp the edge of the notch is. The notch has then to be disperse, and this is done with a final spectrometer phase. The CCD detector transforms the incoming photons into photo electrons, which is a quantum effect. Therefore the counting of photons can happen.

5.3.3 Data Analysis and Discussion

Based on the crystalline structure, it is possible to derive the expected Raman mode. They are the vibrational modes allowed by the symmetry of the crystal from the group theory. Of the allowed modes, only some of the them effectively react to a Raman excitation, and they are called Raman active (they are the ones visible) [41] and they are calculated by programs online (e.g. VASP [30], or from crystallographic server like [42]) from the unitary cell of the crystal [43].

Polarized Raman spectroscopy can be useful in the study of oriented samples such as single crystals. The polarizability of a vibrational mode is not equal along and across the bond. Therefore the intensity of the Raman scattering will be different when the laser's polarization is along and orthogonal to a particular axis. As this technique is referred to the crystalline axis, it is impossible to be applied in powder samples. X,Y and Z are the position of the polarizators, that can be turned and oriented in different directions. By polarizing light it is possible to chose one mode only. The horizontal plane of the sample is the a-b (X and Y axis), wile the short plane in height is the c axis (Z axis). Polarization is written with the Porto notation [44], e.g. X(YY)X where outside the parenthesis there is the polarization of the incoming and outgoing beam while inside there are the incoming polarization of the laser beam and of the outgoing Raman signal.

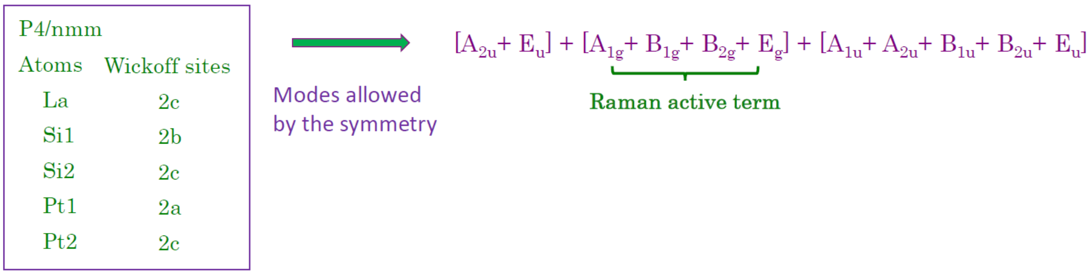

P4/nmm

Atoms	Wickoff sites
La	2c
Si1	2b
Si2	2c
Pt1	2a
Pt2	2c

$$\longrightarrow [A_{2u}+E_u]+\underbrace{[A_{1g}+B_{1g}+B_{2g}+E_g]}_{\text{Raman active term}}+[A_{1u}+A_{2u}+B_{1u}+B_{2u}+E_u]$$

Figure 5.6: Raman active modes for $LaPt_2Si_2$. Calculated with [42].

By polarizing the beam, the mode is selected. As the Z axis is the only axis known, the Z(XY)Z is the only polarization allowed [39]. Other polarization were tried out, for example at 45 degrees, but nothing relevant has been seen, as displayed on the graph of Fig. 5.7.

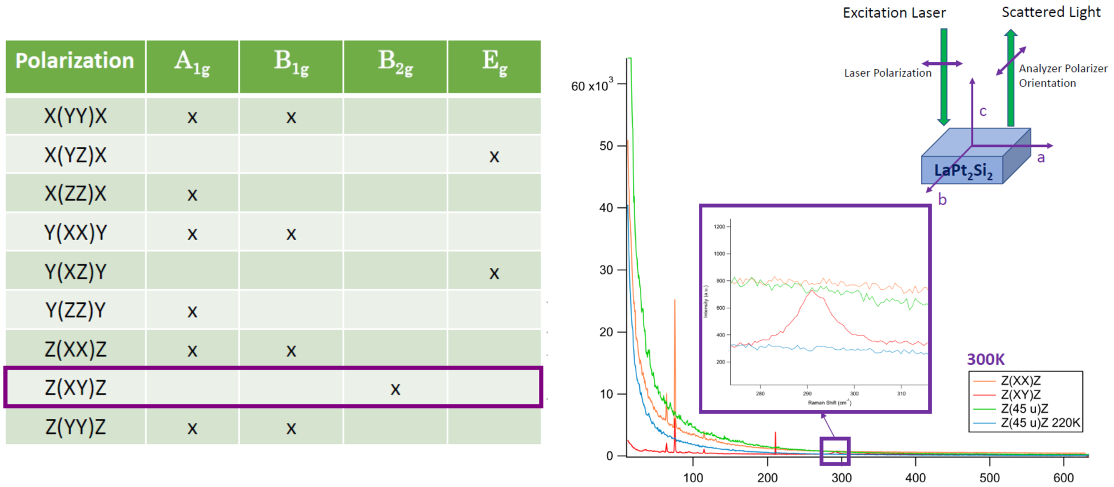

Polarization	A_{1g}	B_{1g}	B_{2g}	E_g
X(YY)X	x	x		
X(YZ)X				x
X(ZZ)X	x			
Y(XX)Y	x	x		
Y(XZ)Y				x
Y(ZZ)Y	x			
Z(XX)Z	x	x		
Z(XY)Z			x	
Z(YY)Z	x	x		

Figure 5.7: Left: Possible Raman polarizations for LaPt$_2$Si$_2$. Z(XY)Z is the one of interest in our case as Z is the c axis of the crystal and the one that we can identify. Right: Plot of intensity (a.u.) vs. Raman shift (cm^{-1}) for different polarizations at 300K. A zoom on the B_{2G} mode for Z(XY)Z polarization is present. A small insert on the top right corner explains briefly how polarization looks like.

Calculations on the expected modes for Z(XY)Z polarization give as a result the B_{2G} mode (left of Fig. 5.7) [42], therefore it has been assumed that the only visible peak is exactly the B_{2G} mode. In the plot of Fig. 5.7, just below 100 cm^{-1}, there are also some sharp spikes which do not belong to the sample, they come from either noise or instrumentation. It is possible to see them also on the left hand side of the plots in Fig. 5.8, they do not vary with the temperatures.

Once the B_{2G} mode is selected, then the temperature ranges has been changed. The background has been subtracted from the data, also the dark counts which are the photons from the environment, they are visible also when the beam is off.

The peak at approximately 160 cm^{-1}, i.e. 20 meV, seen in Fig. 5.8, increases with the temperature, therefore it seems not to be related with the structure transition. It could be related to some misalignment of the sample (c axis was not perfectly parallel to the incoming beam). It is weaker compared to the B_{2G} mode but it has a similar trend in temperature.

In Fig. 5.8, a polynomial background has been subtracted and the correction for the factor of occupancy of Bose-Einstein has been done. The Bose correction takes into account the change of population of the vibrational states as function of temperature.

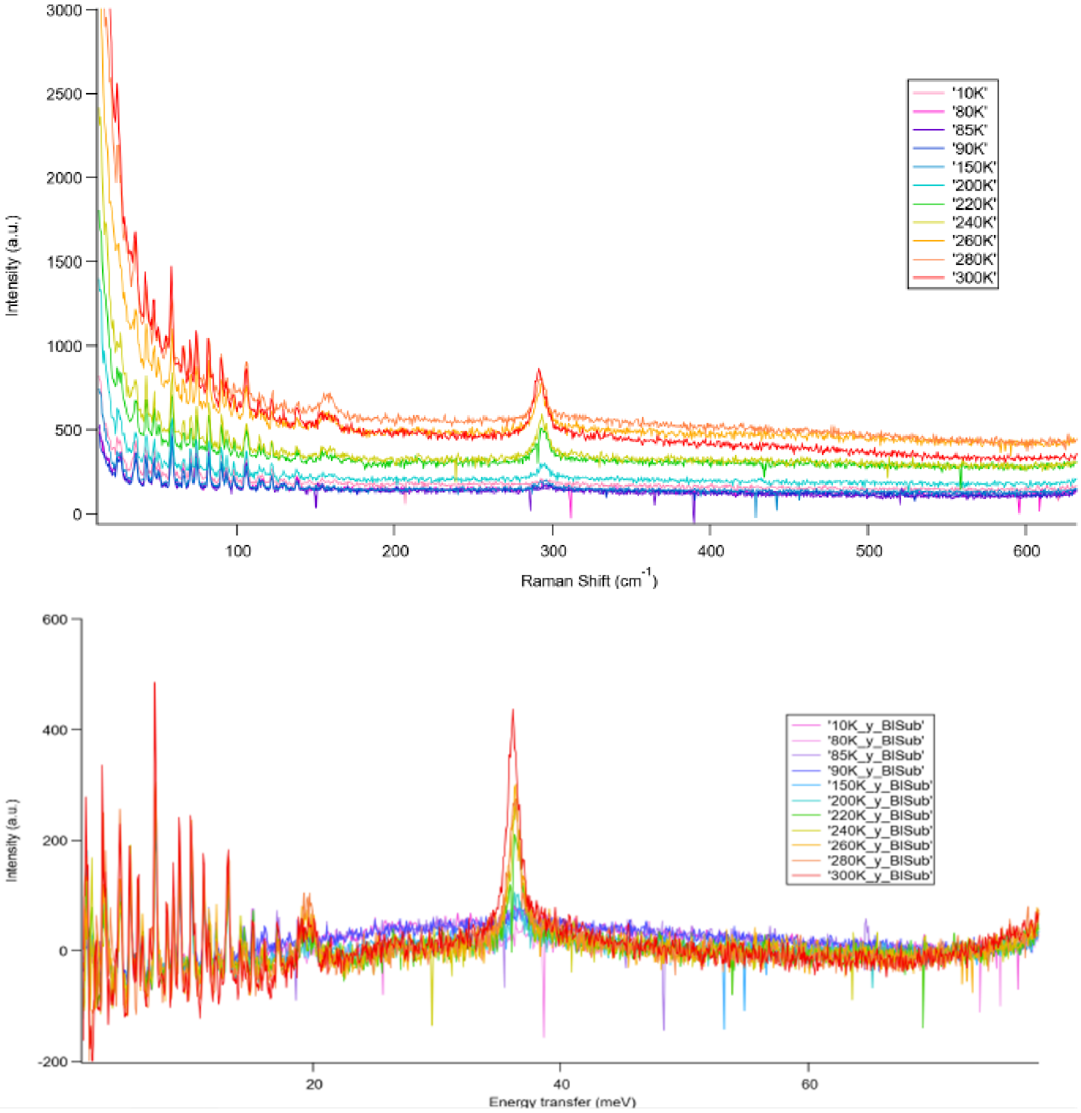

Figure 5.8: Raman scattering at different temperature measurements. On the second plot, Raman shift is converted from cm^{-1} to meV.

The B_{2G} mode is clearly visible at around 300 cm^{-1} and it is present at all temperatures (Fig. 5.8).

The fit of the data was done with a Lorentzian function, which is standard for Raman data [34]. The fit is temperature dependent and it is displayed in Fig. 5.9. The parameters analysed are the amplitude of the peak (amp), the FWHM and the position of the center as seen in Fig. 5.10.

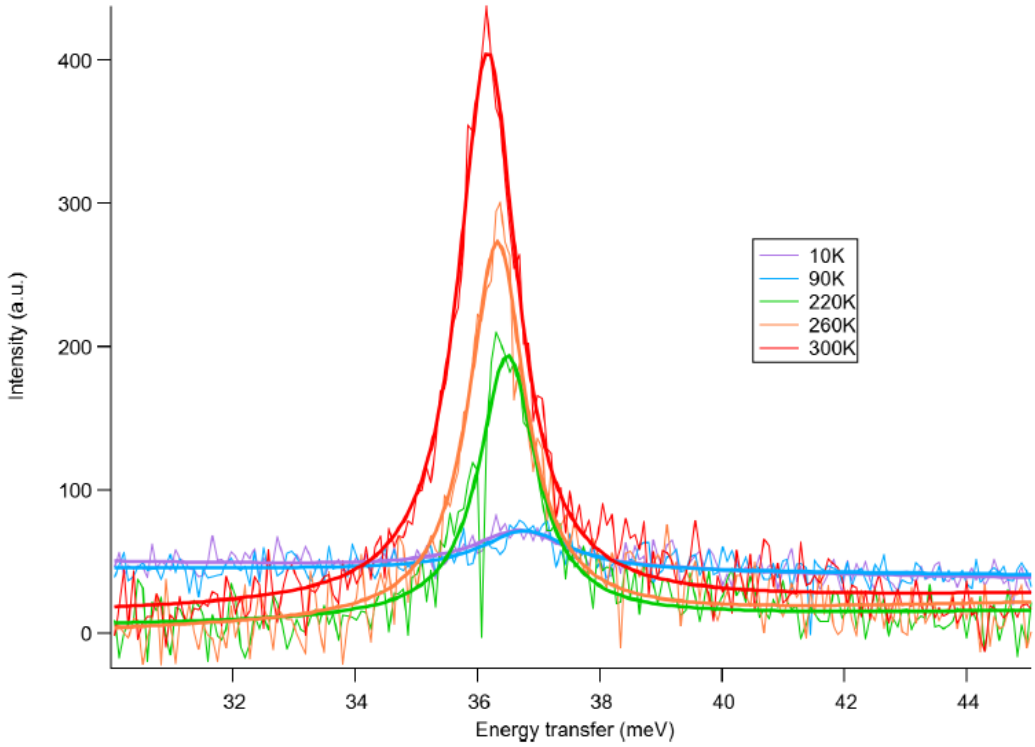

Figure 5.9: Lorentzian fit of the B_{2G} mode selected at different temperatures.

From Fig. 5.10, it is possible to observe that the center and the FHWM are shifting with respect to the temperature. At 85K there is something anomalous, this could be the fingerprint of the CDW at 85K.

The FWHM behaviour is consistent with the literature results [1], where the satellites have their maximum intensity at 85 K, disappear above 175 K and almost vanish below 85 K. The broadening of the FWHM is consistent with the opening of the gap at the Fermi surface [34].

The frequency for the Raman mode shows a kink around 85 K and then decreases linearly as the temperature increases. Due to the weakness of the mode below 100K it was not possible to follow the temperature dependence of the CDW order parameter below the transition. The linear temperature evolution of the phonon frequency above the putative CDW transition could be a thermal effect due to the fluctuations of the inter atomic potentials resulting from thermal expansion and phonon phonon coupling.

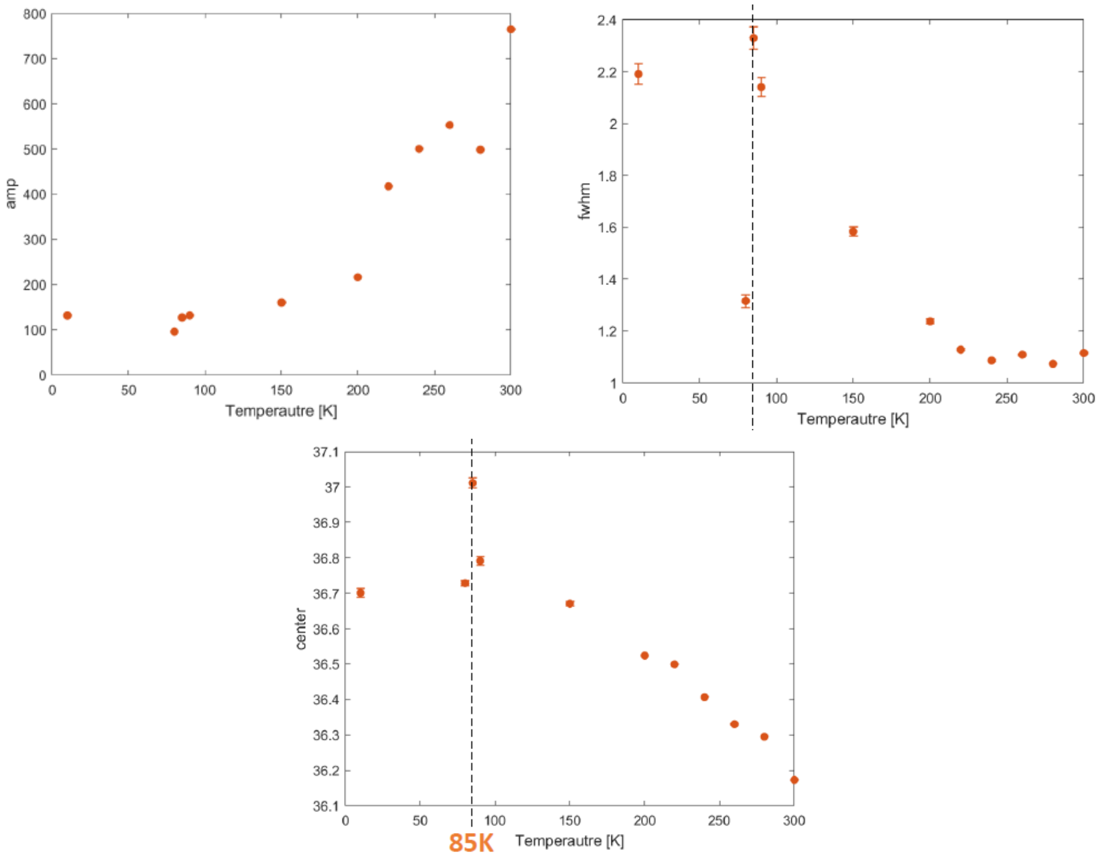

Figure 5.10: Fit results for the three parameters, height, fwhm and center as function of temperature.

To conclude, the data need to be completed, however, the FWHM plot shows a clear constant dependence above 200K and a clear increase below 200 K, which lead us to the conclusion that the CDW is present. The anomaly at 85 K is compatible with the occurrence of a structural transition associated with a CDW transition, as reported in the literature.

Chapter 6

Single Crystal X-rays Diffraction on $LaPt_2Si_2$

6.1 Background and motivation

X-ray powder diffraction (XRD) is an analytical technique primarily used for crystal structural studies and can provide information on unit cell dimensions and atomic positions. XRD is based on constructive interference of monochromatic X-rays and a crystalline sample, when conditions satisfy Bragg's Law ($n\lambda = 2dsin\theta$), see Fig. 3.1. This law links the wavelength of electromagnetic radiation to the angle of diffraction and the lattice spacing in a crystalline sample. The diffracted X-rays are then detected and the counts rates are analyzed. By scanning the sample through a range of 2θ angles, all the diffraction directions of the lattice should be seen due to the random orientation of the crystallites in the powder material, as seen in Fig. 3.2. By converting the diffraction peaks to d-spacing, it is possible to identify the material, as each one has a set of unique d-spacings.

The relevant theory of diffraction has been discussed in Chapter 3 for neutrons: this can also be applied to X-rays.

All XRD studies of $LaPt_2Si_2$ that are seen in the literature [1] [32] were all done with in-house instrumentation. A structural study of the polycrystalline material revealed a structural transition from high-T tetragonal to low-T orthorhombic symmetry at T = 112 K, showing a clear splitting of the (220) reflection peak into two subpeaks with nearly equal intensity below T = 100 K [12].

It has been suggested that also in the case of single-crystalline $LaPt_2Si_2$ [32], the formation of the CDW state could be associated with the structural phase transition. The nature of the CDW transition in this compound is still not fully clarified.

In the last XRD measurement done by Falkowski et al. [1], the structure has been refined within the tetragonal $CaBe_2Ge_2$ structure (with space group P4/nmm) in a T range 5–300 K, showing that the tetragonal symmetry in single-crystalline LaPt$_2$Si$_2$ is preserved down to low temperatures.

The crystalline structure of the single crystal seems to be something still unsolved. Unfortunately, there was no possibility to make a high-resolution synchrotron experiment. At a large scale facility, lower T could have been reached also with higher resolution and this could lead to the observation of the very weak crystalline structure changes. Instead, there was the chance to perform an in-house XRD experiment and have our own data on XRD to study.

6.2 Instrumentation

The experiment and the acquisition of the data was done by the PhD student Elisabetta Nocerino from KTH Royal Institute of Technology, at Stockholm University, Department of Materials and Environmental Chemistry (MMK) with the support of Dr. Andrew Kentaro Inge.

Typical Diffraction instrumentation has been discussed in chapter 3, paragraph 3.5.

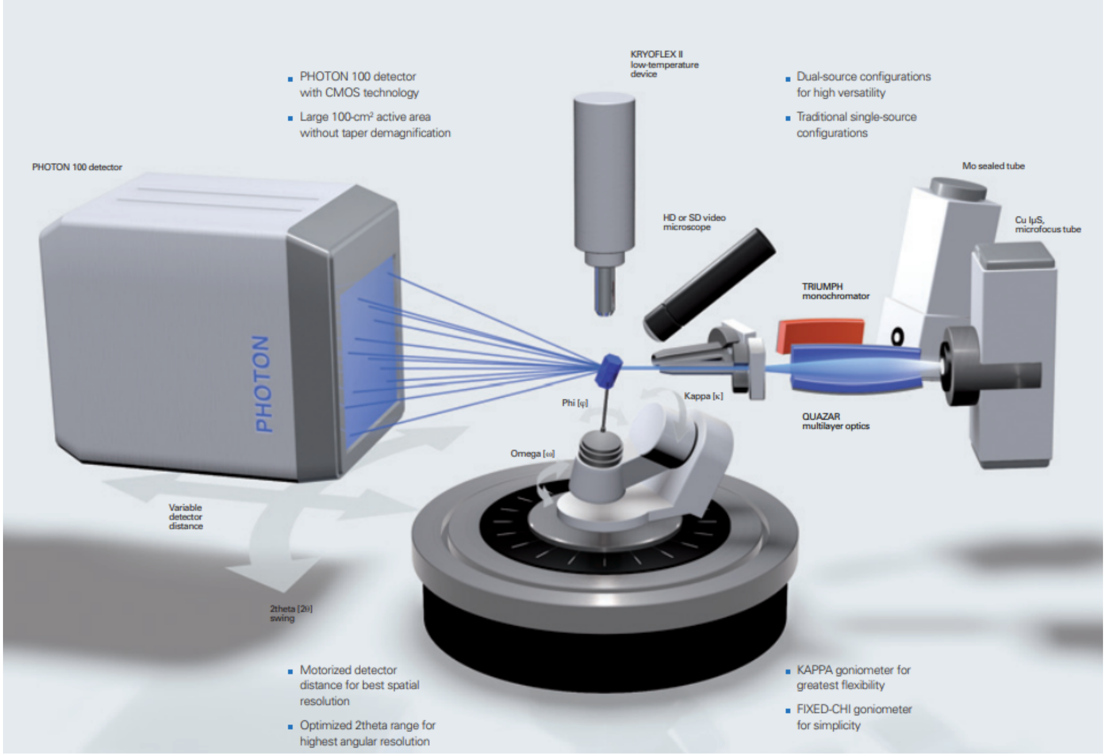

Figure 6.1: Diffractometer geometry of D8 Venture Bruker Diffractometer. From [45].

The instrumentation used is a D8 Venture Bruker Diffractometer, an illustration is shown in Fig. 6.1. It has a Mo source that goes through a monochromator, selecting a wevalength of $\lambda = 0.61063$ Å. The slit determines the scattering angle. Collimators and other optics are also used to improve the resolution.
Our smallest crystal ($1 \times 1 \times 1$ mm^3) was crushed and mounted on a glass needle with glue under the microscope. The X-rays hit the sample that has been cooled with a liquid Nitrogen blower cryo-system, with a T range of 80-300 K. The pump is responsible for the gas flow through the flexible vacuum insulated transfer line, into the Cryostream cold head. The liquid nitrogen passes through a heater, which evaporates most of the liquid into gas. This gas then flows outward along one path of the heat exchanger, through the temperature and flow controller, to arrive at the pump. This gas flows back into the Cryostream cold head where it is re-cooled along the second path of the heat exchanger.
Photon detectors, positioned after the sample, count the scattered photons. A photon detector has a surface that absorbs photons and produce an electrical signal proportional to the number of photons absorbed.

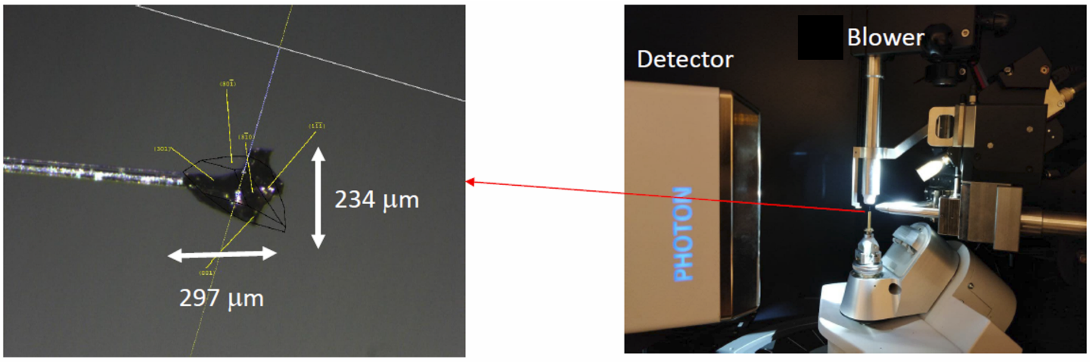

Figure 6.2: Left: $LaPt_2Si_2$ sample used in the XRD experiment. Right: Positioning of the sample in the set up.

For the measurement strategy, it was assumed that there was no symmetry, therefore every angle was taken, the angular scan covered the full 3D range with steps of 1.2 deg, the sample was rotated with a goniometer. Each angle was acquired for eight seconds, a whole scan at a fixed T took approximately two hours.

6.3 Data analysis results

The program used for data treatment is APEX3, data reduction included absorption correction for strong absorbers. Heavy elements as the ones present in $LaPt_2Si_2$ can easily absorb photons.

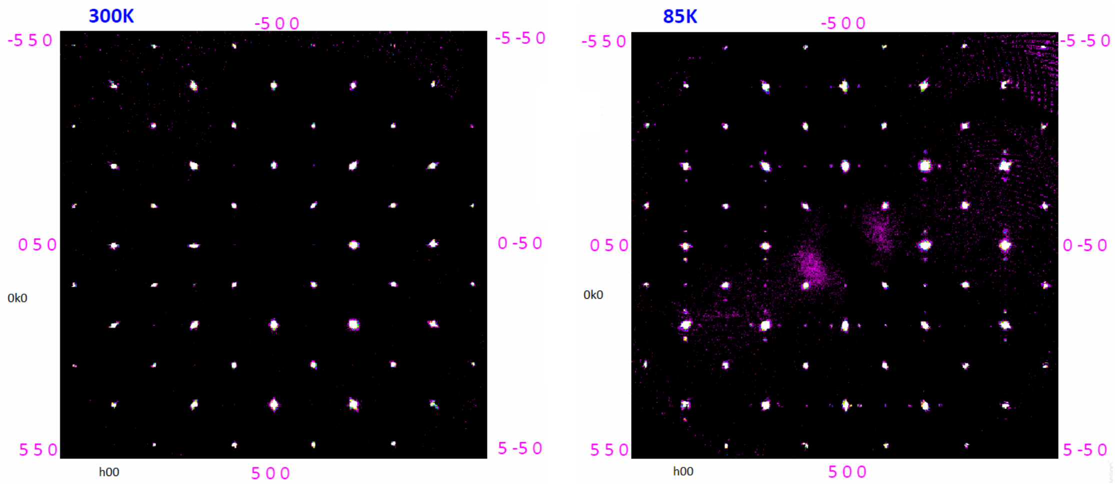

Figure 6.3: 2D Maps of the Bragg reflections in the hk0 plane. Left: Data at 300 K. Right: Data at 85 K. The purple colour is the intensity scale, dark purple is low intensity, light purple is high intensity.

In Fig. 6.3 at 85 K, some small reflections appear periodically around the big Bragg reflections. They have a periodicity of (0.36, 0, 0) all over the map which is the fingerprint of a structural change. During theoretical calculations done by Dr. Johan Hellsvik from PDC Center for High Performance Computing, KTH, Stockholm, Sweden, it was observed that it was not certain whether the primitive cell has space group P4/nmm or I4/nmm [8]. Thanks to this experiment, it was possible to observe that the unit cell is most definitely primitive (P), there is no match for body centered (I) cell. This unit cell was used for all temperatures, however at 85 K the program had some difficulties in recognizing the cell compared to the other temperatures, which could indicate a structural change of the unit cell.

The halo (diffuse scattering), seen as two broad blobs close the the center of the right panels (at 85 K) in Fig. 6.3, Fig. 6.4 and Fig. 6.5, is coming from the liquid Nitrogen used in the blower cryo-system.

From the other planes, h0k and 0kl, seen in Fig. 6.4 and Fig. 6.5, no additional Bragg peaks were observed between 300 K and 85 K, the 2D maps are shown for completeness.

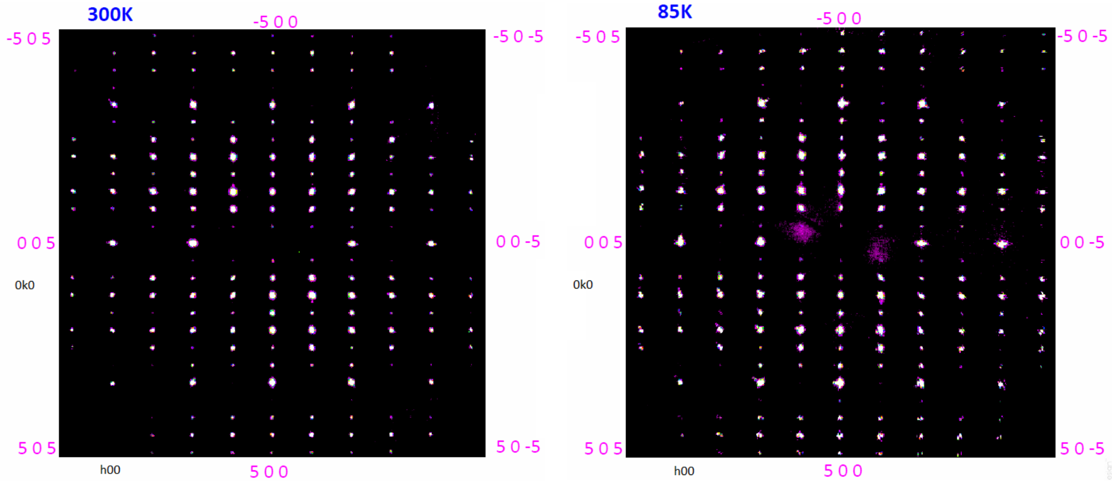

Figure 6.4: 2D Maps of the Bragg reflections in the h0l plane. Left: Data at 300 K. Right: Data at 85 K.

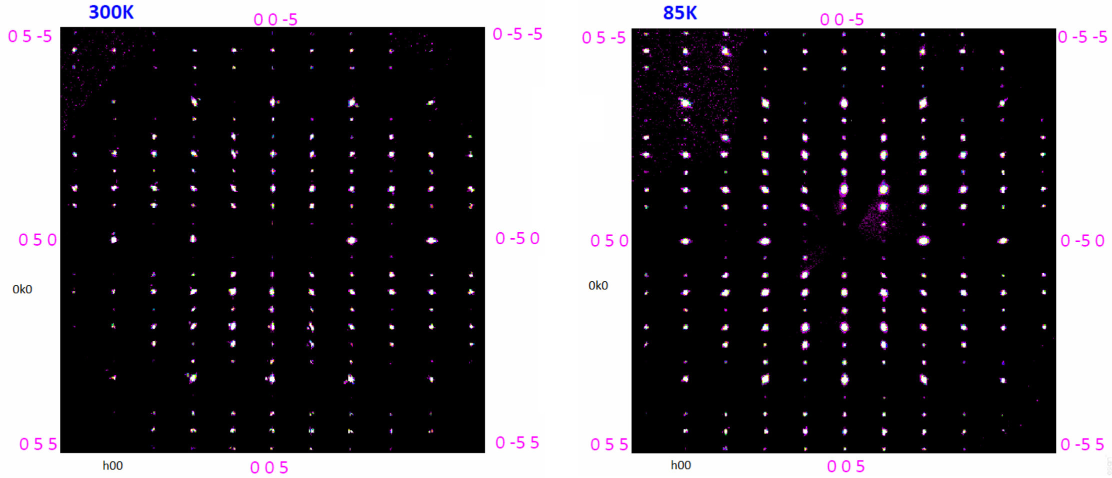

Figure 6.5: 2D Maps of the Bragg reflections in the 0kl plane. Left: Data at 300 K. Right: Data at 85 K.

On the left of Fig. 6.6, the 2D map acquisition has been overlapped with the calculated Bragg positions according to the unit cell P4/nmm (green spots). The fractional peaks (satellites) are instead not matched by the chosen unit cell.
By using APEX3 it was not possible to identify the integrated intensities at the fractional coordinates. In order to overcome this problem, the unit cell was tripled in the *ab* plane by multiplying the coordinates by a factor three. With the tripling in size it is possible to index also the small peaks, the ones around the big Bragg spots, as seen on the right of Fig. 6.6. The program gives as output an hkl

file, where there are the list of Bragg reflections, with their related coordinates, intensities and errors. The program calculates the integrated intensity (area under the peak) of the Bragg spots inside the green circles.

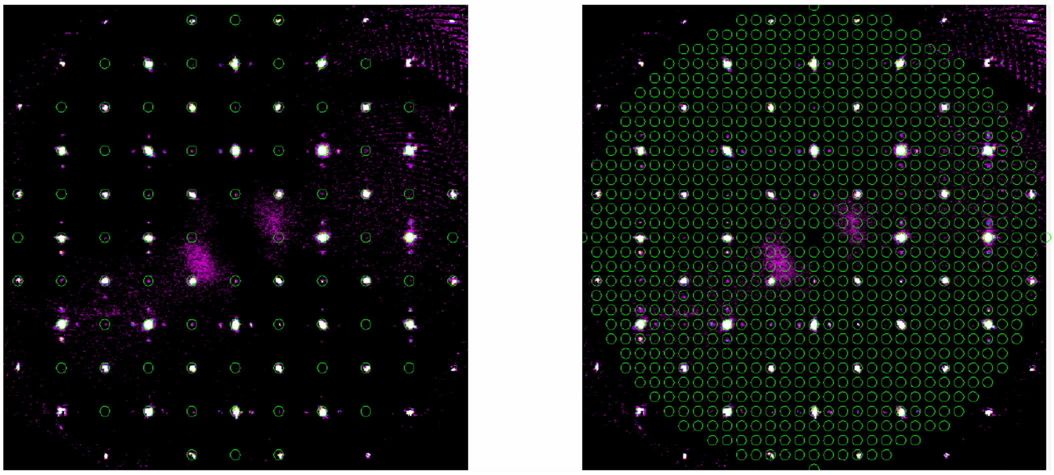

Figure 6.6: The plane is $h00$ and $0k0$. Left: integrated intensity of the Bragg spots in the original primitive cell. Right: in order to estimate the intensity of the satellites, the unit cell was tripled along the a and b direction. The unit cell is now: P4/nmm where a = b = 12.8412 Å and c = 9.83070 Å.

On the right of Fig. 6.7, the integrated intensity of two super structural peaks, the (-0.33, 2, 0) and the (2, -0.33, 0), has been plotted as function of temperature. The measurements with respect to the temperature were done at room temperature first, then the sample was cooled down to 80 K, and then the data acquisition was done while increasing the temperature. Unfortunately the statistics at room temperature was not sufficient to include it in Fig. 6.7.
The intensity on the right of Fig. 6.7 seems rather jumpy and unphysical, and it could be influenced by experimental inaccuracies, such as the temperature control (N2 nozzle cooling is not as stable as a closed cryostat used in synchrotrons). There is indeed a maximum at 85 K, where the satellites appear in the previous literature [1], but it is a local maximum. By going up in temperature, another maximum is reached around 100 K. From 120 K upward, the acquisition was done with a bigger step in the temperature range due to lack of time.
From the 2D map at 200 K, it is not possible to see by eye the superstructure peaks therefore the intensity should be zero. This lead to the conclusion that what is seen around 200 K in Fig. 6.7 should be considered as background level. There is also an instrumental effect, all the peaks that are equivalent reflections should have the same intensity, instead they changed, but this can be due to instrumental error. The error bars on the right of Fig. 6.7 are the sigma value that is calculated

through the program and appear in the output file.

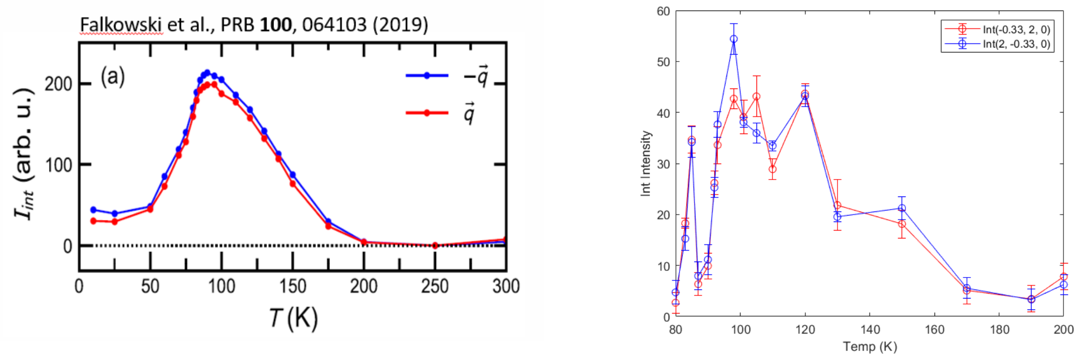

Figure 6.7: Left: temperature dependence of integrated intensity of the satellites that appear at 85 K, from Falkowski paper [1]. Right: the integrated intensity of two superstructural peaks as function of temperature from XRD data.

Comparing the XRD data with the Falkowski paper data, the results overall looks quite similar, however, our data have more structure (up and down within a few K temperature, also between 85 K and 90 K there is an heavy drop not present in the paper). This needs to be further investigated. There are several differences in the trend, for example the intensity at 80 K and 200 K is the same for our data but not for the Falkowski measurements. The intensity ranges cannot really be compared as the normalization procedure and the statistics are different. In the paper it is mentioned that they had a limited angular coverage, therefore it is possible that they did not see the whole evolution of the structure.

The transition from tetragonal to orthorhombic cannot be seen by eye from the 2D maps, the position of the peaks are the same (green circles), what is changing is the intensity of the equivalent peaks.
On the structure, there is a check that can be done as in tetragonal symmetry, equivalent reflections should have the same intensity [46]. By taking the symmetry class of tetragonal unit cell, certain symmetry operations that should be equivalent, for example the intensity hkl should be equal to -khl. In orthorhombic (lower symmetry) instead this permutation does not hold anymore. Thus, it is worth taking one Bragg spot's equivalent reflections and check between the several temperatures if the intensity changes. If the intensity change between the two coordinates then they are not equivalent anymore, therefore there is no tetragonal symmetry [46].

The intensity of the (2,1,0) and (-1,2,0) peaks are plotted in Fig. 6.8. These two intensities should be equivalent in a tetragonal symmetry, not in the orthorhombic one.

It is possible to observe that the intensity of the two peaks are equal in the whole range within the calculated error except at 85 K where the values are very different and exceed the error bar values. In order to determine a change in the symmetry in an accurate way, a structural analysis with a refinement is needed. To conclude, at 85 K there might be an hint of a possible change of symmetry but this cannot be said with certainty. Further investigation is needed.

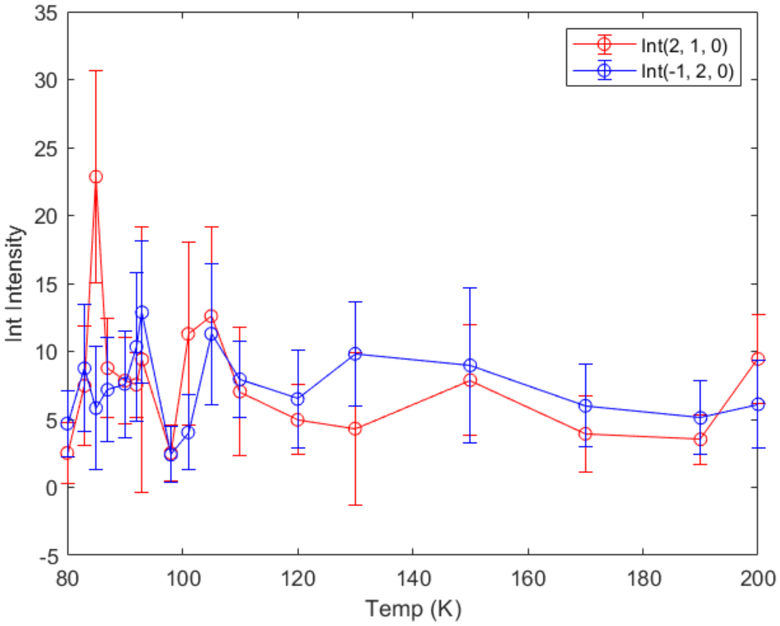

Figure 6.8: Integrated intensity of two equivalent peaks (2,1,0) and (-1,2,0) in the tetragonal symmetry (hkl=-khl) as function of temperature.

Chapter 7

Inelastic Neutron Scattering: Experimental background and setup

7.1 Experimental setup

7.1.1 J-PARC - Japan Proton Accelerator Research Complex

The Japan Proton Accelerator Research Complex J-PARC is a joint project between two organizations, High Energy Accelerator Research Organization (KEK) and Japan Atomic Energy Agency (JAEA). The facility is located in Tokai village in the northern region of Ibaraki prefecture, Japan.
J-PARC is a research facility, which consists of a series of proton accelerators and the experimental facilities that make use of the high-intensity proton beams. It is a multi-purpose and multidisciplinary facility open to users from all around the globe. A unique variety of secondary particle beams, such as neutrons, muons, pions, kaons and neutrinos are produced by colliding proton beams with different target materials (spallation reactions). The application of those beams cover different fields of research, from nuclear and particle physics to material and life science [47].
J-PARC consists of three proton accelerators:

- a 400 MeV linear accelerator (Linac) currently operating at 180 MeV
- a rapid-cycling synchrotron (RCS) with a total energy of 3 GeV
- a 50 GeV main ring (MR)

In each case, target materials and designs are employed to maximize the production of the desired secondary particle beam. During normal operation mode, over 90% of the protons accelerated in the RCS are directed to the neutron and muon production targets in the Material and Life Science Experimental Facility (MLF) [47]. The remaining protons are transported to the main ring for further acceleration before being extracted via one of the two main ring extraction ports that take them to other facilities and the related experiments. Depending on whether the protons come out from the slow extraction port, fast extraction port or are generated in pion decay processes, they are sent to different experiments [47]. The proton beam cascades the graphite target of muons and reaches to the target for neutrons [48]. The Material and Life Science Experimental Facility (MLF) provides the world's highest flux of neutrons and muons by proton-impact nuclear spallation reactions with a 3 GeV proton synchrotron of 1MW beam power. With a total of 23 neutron beam lines and 4 muon beam lines, the MLF facility has rapidly become a world leading center of materials and life science research [48], an overview of the entire research complex is provided in Fig. 7.1.

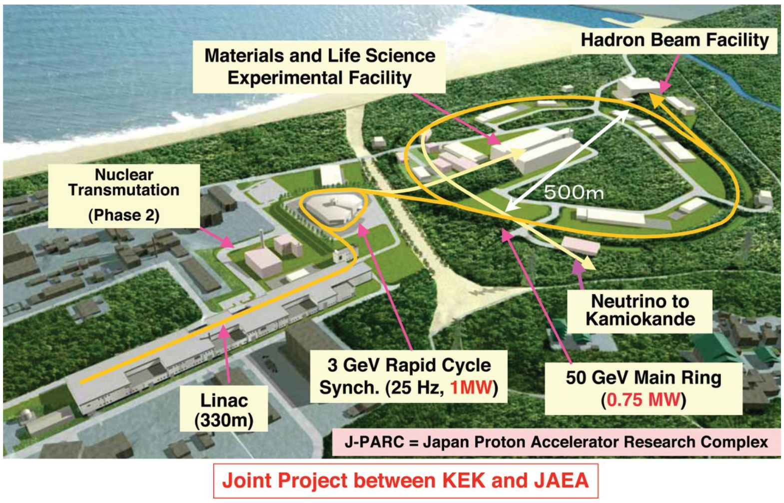

Figure 7.1: The entire view of the Japan Proton Accelerator Research Complex (J-PARC), adapted from [49].

.

7.1.2 HRC - The High Resolution Chopper Spectrometer

The inelastic neutron scattering (INS) studies of the $LaPt_2Si_2$ single crystalline sample were performed by using the High Resolution Chopper Spectrometer (HRC) in the MLF facility of J-PARC. This equipment provides opportunities to perform dynamical studies of materials with high resolution over a wide energy-momentum space. Three types of inelastic neutron scattering experiments can be performed with the HRC: high-resolution experiments in a conventional energy-momentum space, eV neutron spectroscopy, and neutron Brillouin scattering (NBS). Specifically, we used it for high-resolution inelastic neutron scattering [50].

The instrument is located to face a decoupled moderator that has an area of 100 x 100 mm^2. The moderator will send out neutrons in all directions. At first, the neutron beam goes through to a T0 chopper, which reduces the background noise produced from the high-energy neutrons. To increase the neutron flux at the sample, supermirror guides tubes are used. Then, in the neutron beam line leading up to the HRC instrument, a polychromatic pulsed neutron beam from the moderator gets monochromatized using a Fermi chopper. When an incident pulsed neutron beam goes through the slits in the rotating chopper, an initial energy (E_i) is selected and the beam pulse also becomes well-defined in time.

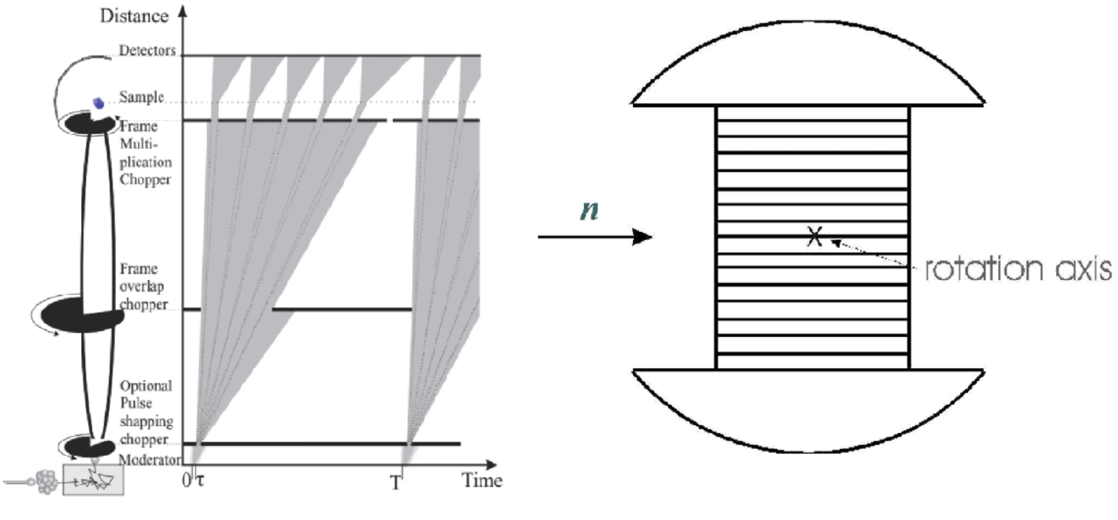

Figure 7.2: Left: Sketch of the main elements of the cold chopper spectrometer. Picture is not to scale. Time-of-flight diagram illustrating the selection of neutron pulses by choppers, with the spectrometer running in repetition rate multiplication (RRM) mode with N = 5. From [51]. Right: Geometry of a straight Fermi Chopper. From [52].

The distance of the Fermi chopper and the sample from the source are 14 and 15 m, respectively. When the neutrons arrive at the sample position, they are scattered by the sample, leading the initial state neutrons going into the final (scattered) state, which is measured using the analyzer and detector array that covers a wide range of different scattering angles. The detector array consists of ^{3}He position sensitive detectors (PSDs) that have a length of 2.8 m and a diameter of 19 mm, located at 4 m from the sample position and can cover scattering angles up to $\psi = 62°$ for conventional experiments. In addition, another detector array of ^{3}He PSDs are located at L=5.2 m and cover scattering angles down to $\psi = 0.6°$ for NBS. Each PSD is mounted with its length direction oriented vertically.

A collimator system composed of slits of vertical Cd sheets is installed in order to redirect the outgoing neutrons. One of two collimators with collimation angles of 1.5° and 0.3° can be selected. The collimators reduce the background noise at low angles down to ψ=3° for conventional experiments, and ψ=0.6° for NBS, respectively.

The scattered neutrons are analyzed through their time-of-flight (TOF) as well as the scattering angle (ψ), and the detected neutron counts are converted to the dynamical structure factor $S(\vec{Q},\omega)$ as function of the momentum transfer $\vec{Q}$ and the energy transfer E. An overview of the instrument is provided in Fig. 7.3 [53].

The High-Resolution Chopper (HRC) in J-PARC offers a very good compromise between resolution (ΔE/E$_i$ $\geq$2.5%) and neutron energy (5 $<$ E$_i$ $<$ 500 meV), as well as wide angular coverage for the detector banks (ψ = 3 - 62° horizontal and ±20° vertical) that can be chosen for a high-resolution experiments in conventional energy-momentum space. Moreover, there are two Fermi choppers that can be chosen depending on the experiment conditions in order to optimize the experiments, an high-intensity chopper (Fermi A) and an high-resolution chopper (Fermi B). Each of them is composed of a slit package, which is a layered assembly of several components that includes shielding plates and spacers (spacer width w) sandwiches by curved walls (wall curvature R). The cross-section of the slit package of a vertical slit is of 75 mm in width x 64 mm in height, with a length of 100 mm. It is inserted in a cylindrical rotor, with a diameter of 125mm, that rotates around the vertical axes with a frequency range f = 100 - 600 Hz [54]. The neutron pulse length, the opening time, and the flight length, combined with the basic equation $v = \frac{L}{t}$ determine the initial velocity of the neutron v_i. By error propagation it is possible to get $dv^2 = (\frac{dL}{t})^2 + (L\frac{dt}{t^2})^2$. Usually the second term dominates, giving $dv = L\frac{dt}{t^2}$. Figure 7.4 provide an overview of the differences in terms of intensity and energy resolutions, as a function of E_i, with respect to different frequency settings for Fermi A and Fermi B choppers [53]. In order to reach all the temperatures needed, a 1K refrigerator (range 1-300K) has been used.

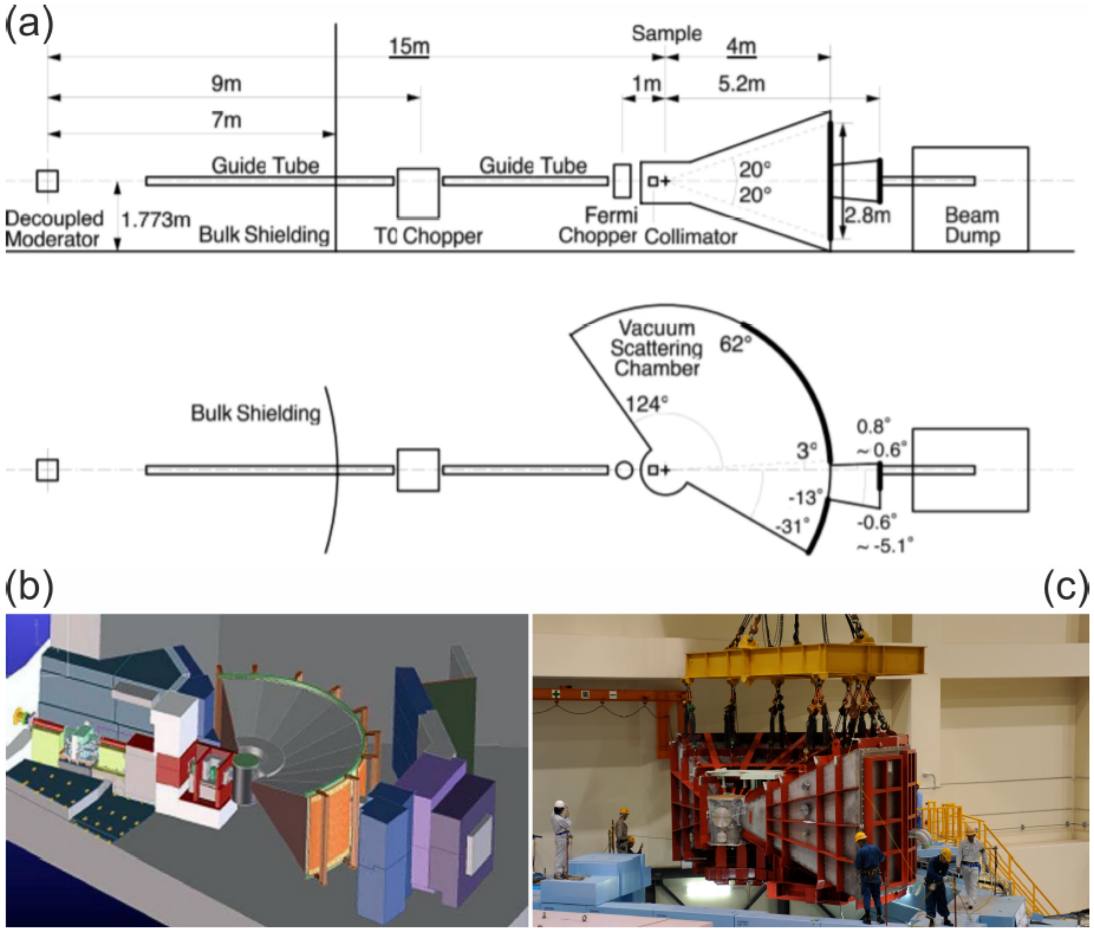

Figure 7.3: (a) Layout of HRC. Thick lines indicate the detector arrays of ^{3}He position sensitive detectors. In the side view (upper figure), the values of the lengths are indicated. In the top view (lower figure), the values of the scattering angles (ϕ) are indicated. From [53]. (b) 3D-CAD of the HRC instrument [55]. (c) Installation of the High Resolution Chopper Spectrometer (HRC) at J-PARC. From [56].

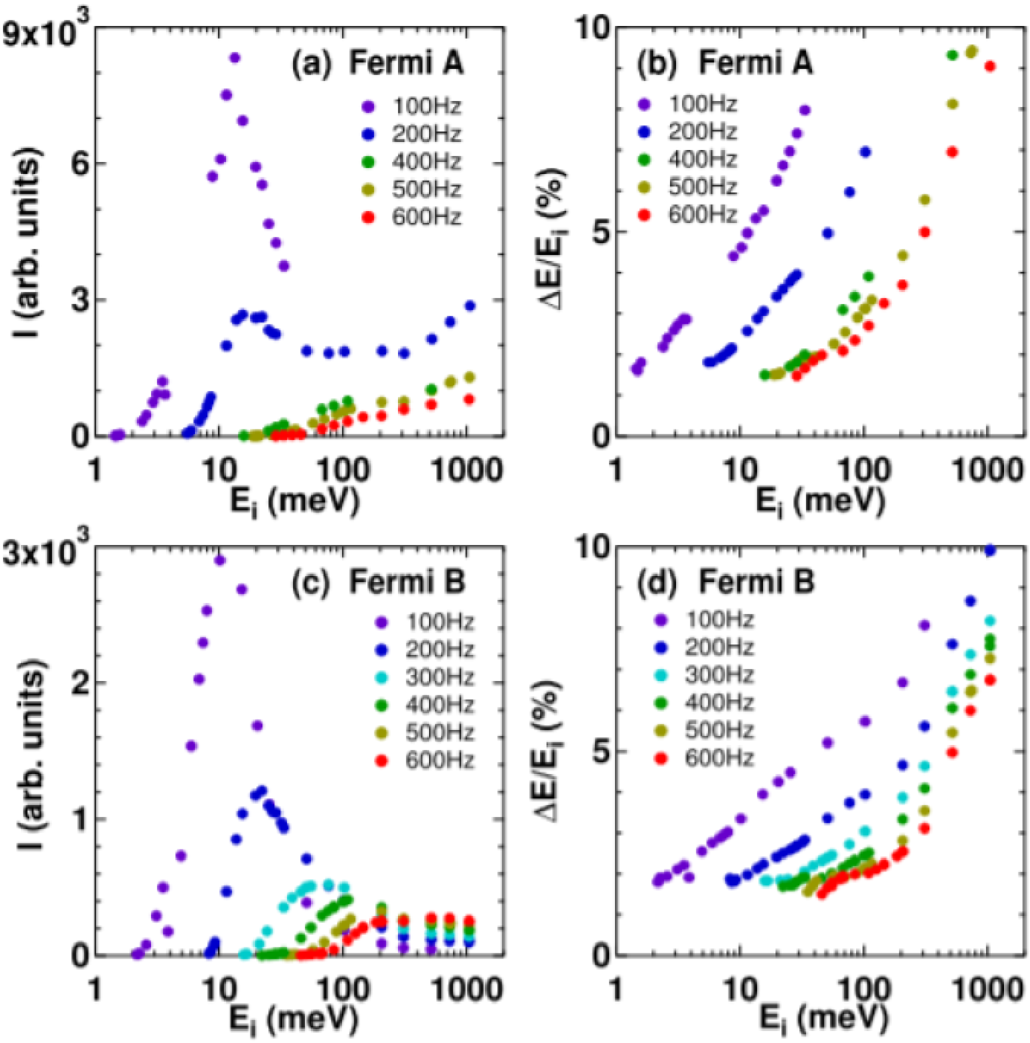

Figure 7.4: Performance of Fermi choppers on the HRC. Intensity I and energy resolution $\Delta E/E_i$ are plotted as a function of E_i for selected rotation frequency f: Fermi A, the high intensity Fermi chopper, with w=2.4 mm and R=1.3 m in (a) and (b), and Fermi B, the high-resolution Fermi chopper, with w=1.2 mm and R=1 m in (c) and (d). From [53].

7.2 Experimental plan

The experimental plan consisted in collecting the full phonon spectra map of $LaPt_2Si_2$ by acquisition of a full 4D $\vec{S}(Q_x, Q_y, Q_z, \omega)$ INS data set (through sample rotational scans) at three different temperatures:

- base-T = 3 K< T_{SL} = 10 K: superlattice phase
- T = 85 K: close to the CDW transition
- T = 220 K: compromise between T_{CDW} and room temperature

The first step consisted in getting a full map of the sample phonon spectra at 85 K with $\omega = 180°$ azimuthal rotation and $\Delta\omega = 2°$ (scan of all even then odd angle values), with a fixed energy for the incoming neutrons of $E_i \approx 60$ meV, using the Fermi A chopper, with a 200 Hz frequency, which yielded the best compromise for intensity vs. resolution (see Fig. 7.4).
In this first scan, every angle was measured for 3 minutes, yielding a total of 3 hours measurement for the complete initial map. By analysing the preliminary scan, it has been decided to proceed with a $\omega = 90°$ and $\Delta\omega = 1°$ measurements, with a $\vec{K}_i$ // [110] in order to coincide to [100] after the orthorhombic transition. In order to have 30 minutes of scan per angle, each of the chosen temperatures have been scanned for other 27 minutes per angle of rotation.
Due to the high background signal, empty can measurements have been performed for 2.5 hours per each temperature of interest in order to subtract the aluminium background of the sample container. 2.5 days were needed in order to acquire the full 4D map for each of the three temperatures, leading to a 7.5 days for the experiment in total.
Lastly, the raw data have been reduced using the HANA software [57], in order to analyze and fit them with DAVE [58]. The fit was not always easy to perform, due to the high signal to noise ratio, this is noticeable especially in the 3 K and 220 K fitted data.
The experiments at HRC, J-PARC, has been possible thanks to our local contacts Professor Takatsugu Masuda, Shinichiro Asai and Shunsuke Hasegawa from The Institute for Solid State Physics, Tokyo University, which helped setting up the experiment and provided support for the data analysis. Moreover, the instrument scientist of HRC (J-PARC Center), Shinichi Itoh.

Chapter 8

Alignment of the $LaPt_2Si_2$ sample

8.1 Crystal Alignment preliminary to INS

The aim of this process is to align the crystal in the desired scattering geometry (crystal directions), before conducting the INS experiment. The following preliminary studies, with a focus on the X-Ray Laue technique and sample preparation took place at the Institute of Solid State Physics (ISSP) of the University of Tokyo. The high energy transmission Laue setup had been used to get a preliminary overview of the five different samples.

The X-rays generated from this equipment have 450 kV of power at nominal working conditions. This high energy ensures the investigation of both the material surface and the bulk. The physics behind has been described in Chapter 3, and in particular for X-rays in Chapter 6. The polychromatic X-rays hit the sample, and if the Bragg condition is satisfied, then a Bragg point would appear on the detector. By rotating the sample as well as moving and tilting it along the X and Y directions [Fig. 8.1(a)], the reciprocal lattice points that satisfy the diffraction condition are found, as it is shown in Fig. 8.2(a), which appeared as a luminescent rings, meaning that the X-ray beam was almost parallel to a high symmetry crystal direction.

With geometrical considerations it was also possible to find the [100] direction, even though there is no difference between [100] and [010], since the primitive lattice vectors a and b have the same length in a tetragonal cell.

The Laue technique is not accurate for every sample. The sample taken into account was quite thick and therefore the Bragg peaks map was not very clear. In order to improve the alignment, X-ray diffraction was performed, Fig. 8.1(b), in order to establish the position of the different crystal planes. When X-rays arrive on the sample, photons would scatter on the crystal planes parallel to one axis of the sample (in this case the c axis), if the c axis is effectively aligned then the Bragg reflection should be in a specific coordinate in space, defined by the 2θ angle. Initially, with an ω-scan it has been possible to distinguish the crystal directions and so with a 2θ scan it was possible to find the peaks of interest for each crystal axes. By indexing the discovered peaks as (220), (200), (020), (040) and (400), leading to the identification of the respective crystal axes. After the alignment, the $LaPt_2Si_2$ crystal was initially mounted on an aluminium holder using thin Al wire [Fig. 8.1(c)]. At this point, the sample has been placed again in the transmission Laue for the final alignment [Fig. 8.1(d)], by using the same procedure as before. The Laue is used in order to do again a quick check of the alignment after the mounting, the support is on a material that can still be rotated in case of misalignment. Every time the sample is rotated a new check has to be done.

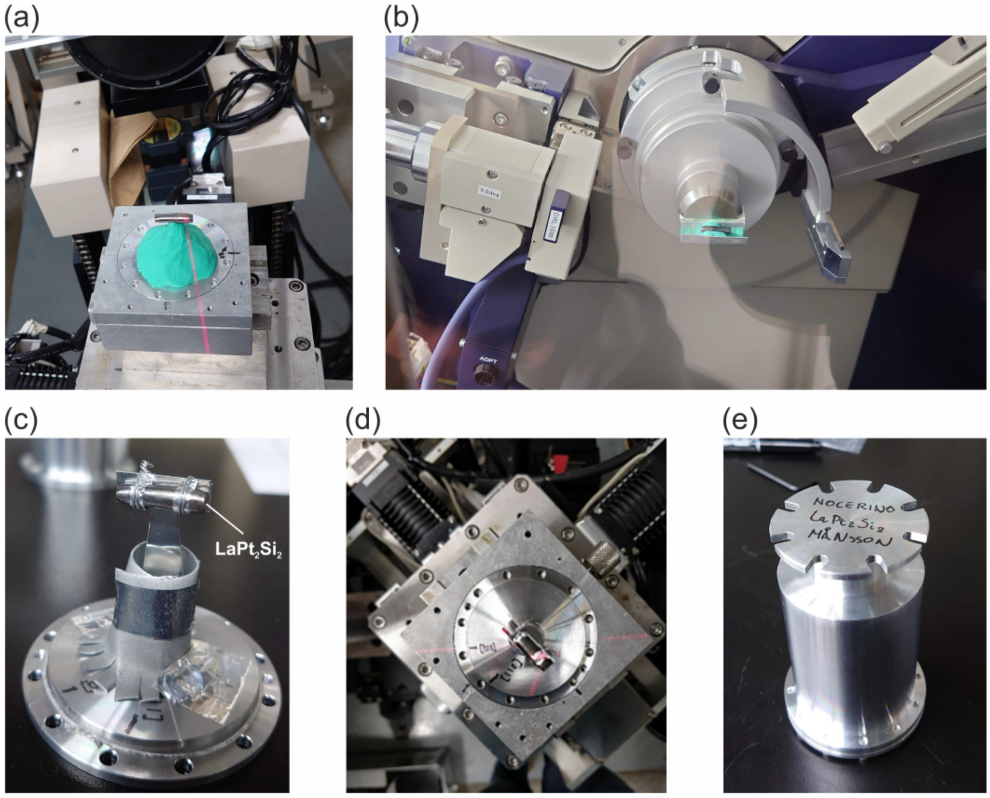

Figure 8.1: (a) Sample aligned in transmission Laue setup. (b) Sample mounted in the XRD machine. (c) Assembling of the sample onto the sample holder. (d) Final alignment of the crystal on holder. (e) Complete sample assembling with thin aluminium canister covering the sample.

Only one out of five crystal was suitable for further investigation and data from this crystal are shown in Fig. 8.2. After a proper alignment, only a luminescent ring as one bright spot should be visible, but in this case, additional rings were present due to the presence of other domains [Fig. 8.2(b)]. In addition, depending on where the scan was set, different results were obtained, leading to the conclusion that the material itself had a certain amount of crystallites of different orientation. There was no possibility to improve it, except for having a better crystal. Nevertheless, this method ensures an high level of precision and the maximum tolerance of misalignment is set at 1-2°. During the final alignment, a Cd shielding of the sample holder base was attached to reduce background signal.

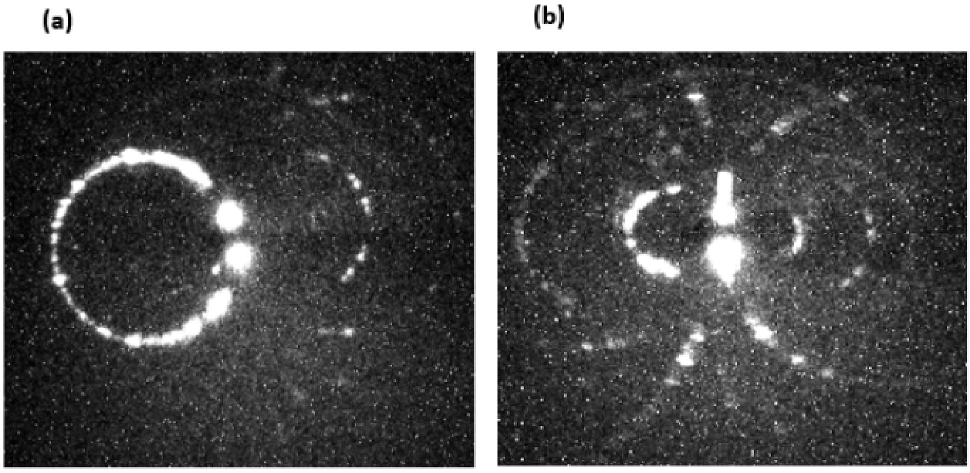

Figure 8.2: (a) Preliminary alignment along [110], the luminescent ring was in good agreement with the results from the Laue simulator. (b) The final alignment along [110].

The Laue simulator software was used in order to analyze the pattern of different crystalline directions starting from the structural data (primitive lattice vectors, volume of the unit cell etc.) and it was possible to compare them with the data collected.

Finally, the sample has been mounted into the aluminum sample holder canister [Fig. 8.1(e)] in pure He atmosphere and closed using an indium sealing. The He atmosphere is needed in order to cool down the sample to 3K without having scattering with particles in the atmosphere and most importantly to keep a thermal coupling between the sample and the surroundings. All other gases will freeze at 3 K temperature, and therefore fail to form a thermal contact.

Chapter 9

Data Analysis and Results on INS

9.1 Introduction to Data Analysis

The data analysis has been performed using DAVE, Data Analysis and Visualization Environment by NIST. The data set is a full 4D $\vec{S}(Q_x, Q_y, Q_z, \omega)$ map that in the reciprocal space are identified by a 3D position vector (H,K,L) and as fourth dimension the energy, therefore it is not easy to visualize it.

In order to display two dimensional cuts, two directions have been used in a 2D plane while a partial integration on the other two dimensions have been performed (see the top of each cut). The data have been collected for 90 different angles. The background removal is essential to have accurate and clear results in terms of phonon spectra (this can be seen in Fig. 9.8 and Fig. 9.13). At first, it has been tried to map the entire background signal to see if any significant feature was present and use it for comparisons. This was not possible because when collecting the empty can measurements, only one angle has been measured, assuming that in this configuration the neutrons beam would scatter identically for all rotation angles (the crystal was not present).

However, if it is assumed to be in a powder diffraction configuration, it is possible to plot some features of the background only. In Fig. 9.1 it has been plotted the background at 3K treated like a powder with two different intensity ranges. It is possible to see that the signal suddenly stops therefore it is not inelastic, hence this can represent a multiple elastic scattering reaching the detectors.

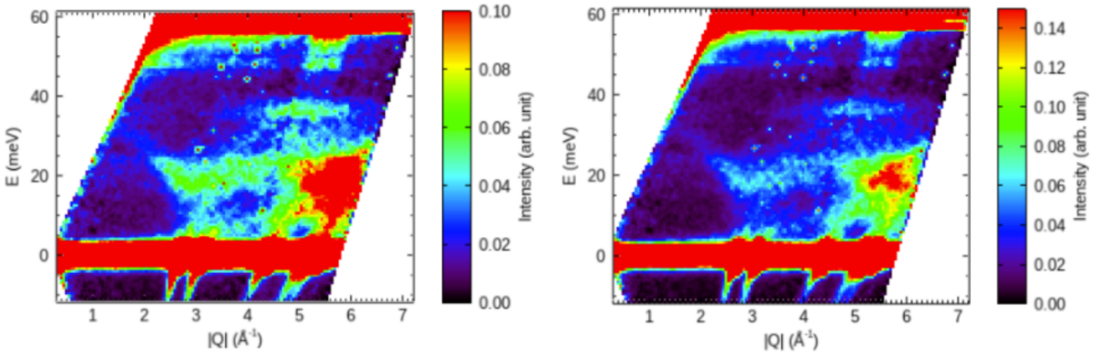

Figure 9.1: Plot of the background at 3K treated like a powder using Dave program. Left: Intensity range [0, 0.1]. Right: Intensity range [0, 0.15].

9.2 Phonons at base temperature 3K

In order to have an overview of the phonon spectra, several cuts in the H-K plane have been performed. At first, the phonon spectra were studied at different energy ranges of approximately 2 meV interval each that could be seen in Fig. 9.2, 9.3, 9.4 and 9.5. The figures are ordered in a decreasing energy order from 30meV to 4meV. By eye inspection, it is possible to see that for example at 30meV, it is not clear where the Bragg points are and if phonons are present, instead by lowering the energy, more features appear, leading to conclude that the range between 6-8 meV was a good one to investigate. The L range is kept symmetrical and close to zero in order to have sharper features but some analysis on broader L ranges is also shown later (e.g. in Fig. 9.11 and Fig. 9.15).
In Fig. 9.7, it is possible to see the two phonons centered at H=0 and H=2 and both at approximately K=-2 on this axis. These two regions are analyzed in details in the next paragraphs. Depending on the intensity range used, it is possible to see more clearly one of the phonons analysed; usually the H=0 is clear at smaller intensity ranges while the H=2 at larger intensity ranges where the H=0 disappears. This is due to the fact that the H=0 signal is close to the (020) Bragg peak while H=2 signal is close to the (220) Bragg peak therefore, as the intensity is proportional to $|Q|^2$, the H=2 phonon will have twice the intensity value.
On DAVE program, the smooth kernel for smoothing the 2D slice data can be changed, the default kernel is [[0.1,0.2,0.1], [0.2,0.8,0.2], [0.1,0.2,0.1]]. The smoothing is done by convoluting the rebinned data with a smoothing kernel. During this analysis, the smoothing factor used is 2, it provides a good compromise between the pixelling and the continuum between the data. From now on, when not specified, all the data have been plotted performing the background subtraction in order to cancel the features due to the scattering of the neutrons with the can of the sample.

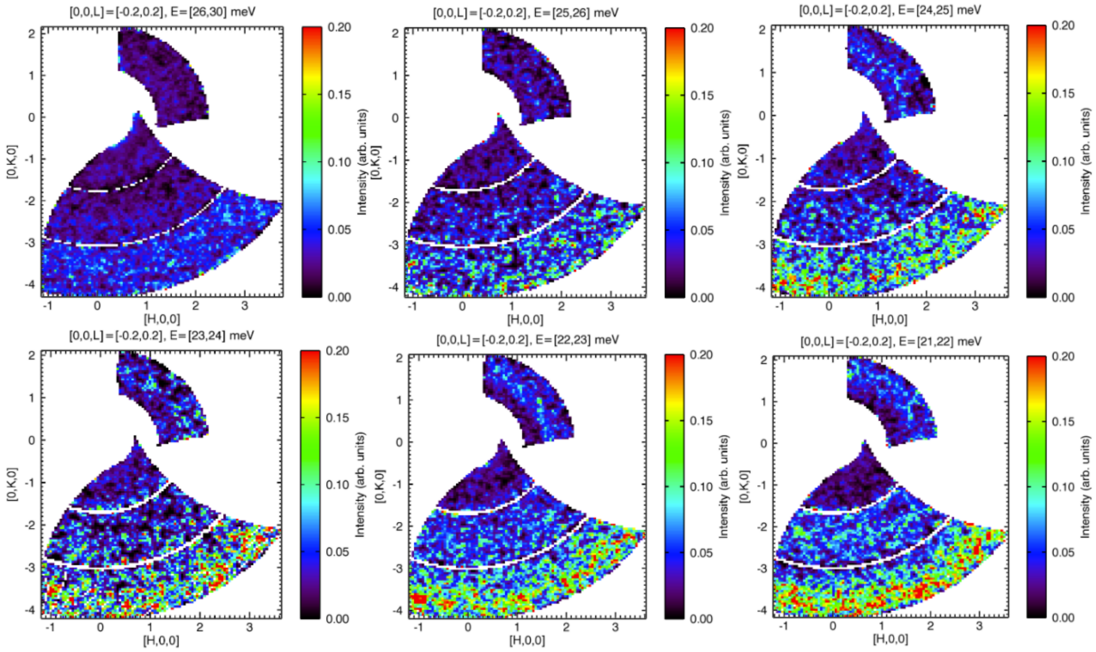

Figure 9.2: 3K overview of the phonon spectra without background subtraction in the energy range $\hbar\omega = 21 - 30$ meV, in decreasing order.

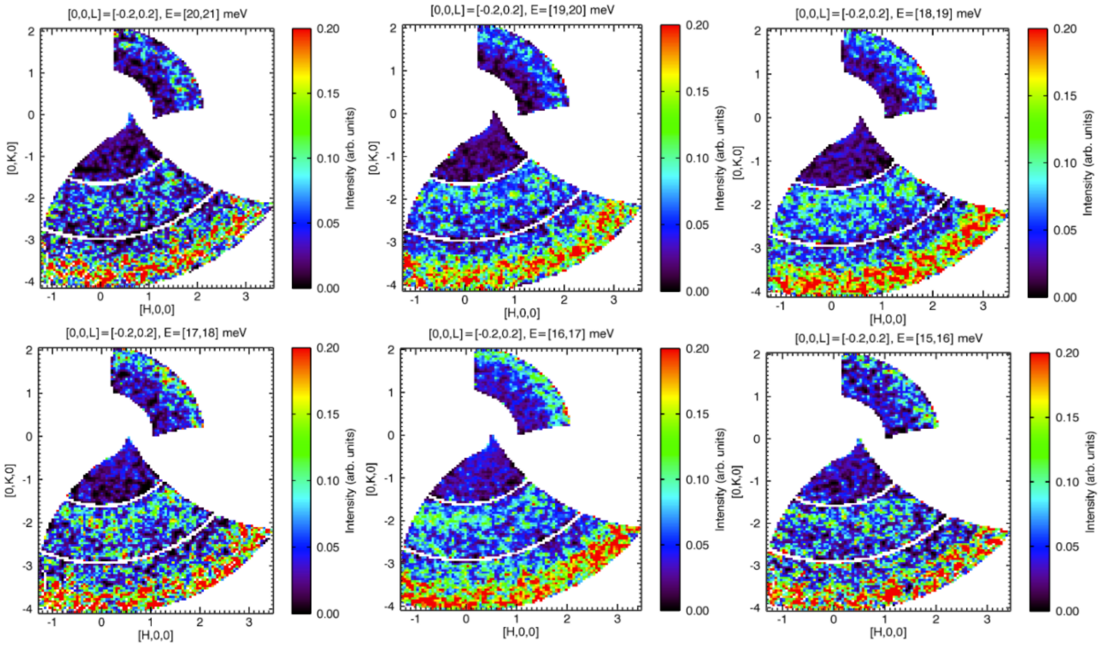

Figure 9.3: 3K overview of the phonon spectra without background subtraction in the energy range $\hbar\omega = 15 - 21$ meV, in decreasing order.

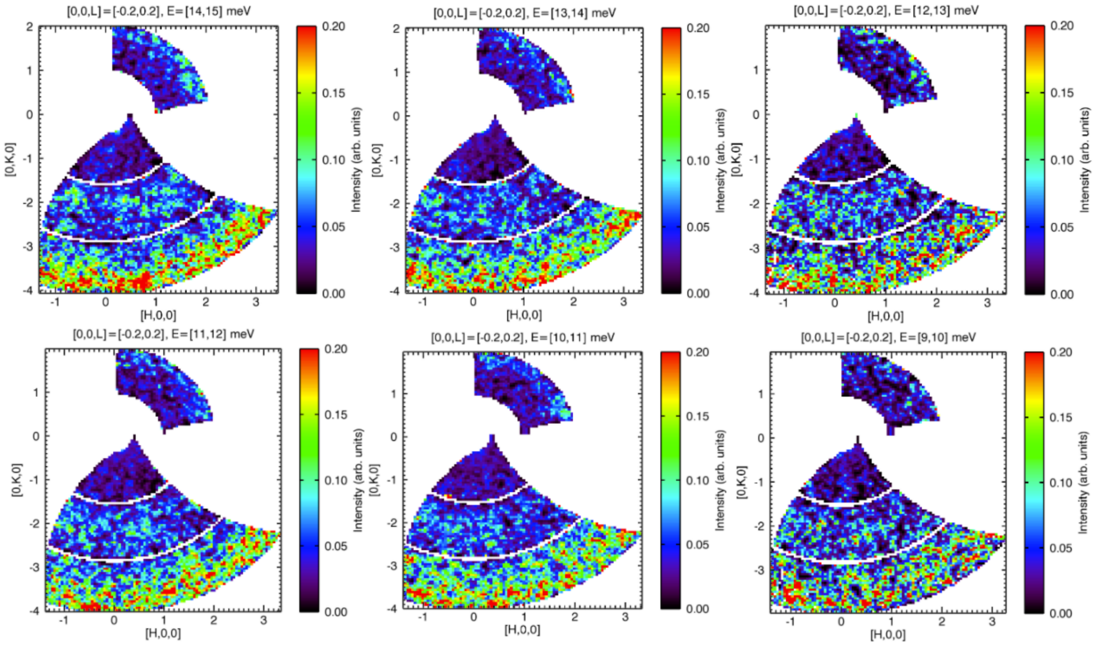

Figure 9.4: 3K overview of the phonon spectra without background subtraction in the energy range $\hbar\omega = 9 - 15$ meV, in decreasing order.

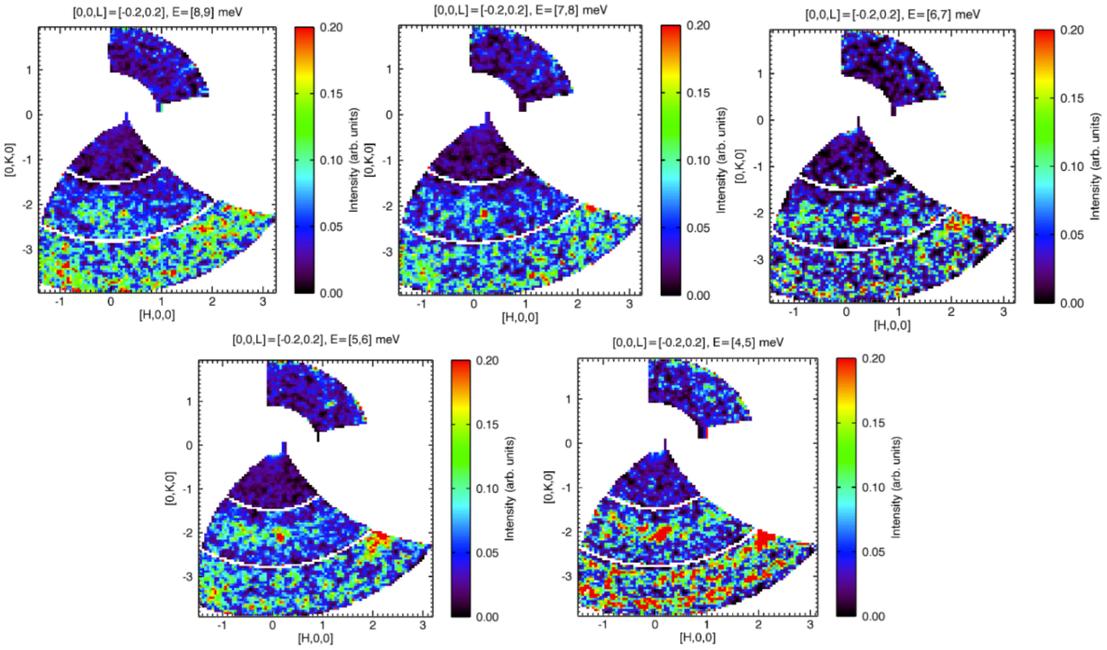

Figure 9.5: 3K overview of the phonon spectra without background subtraction in the energy range $\hbar\omega = 4 - 9$ meV, in decreasing order.

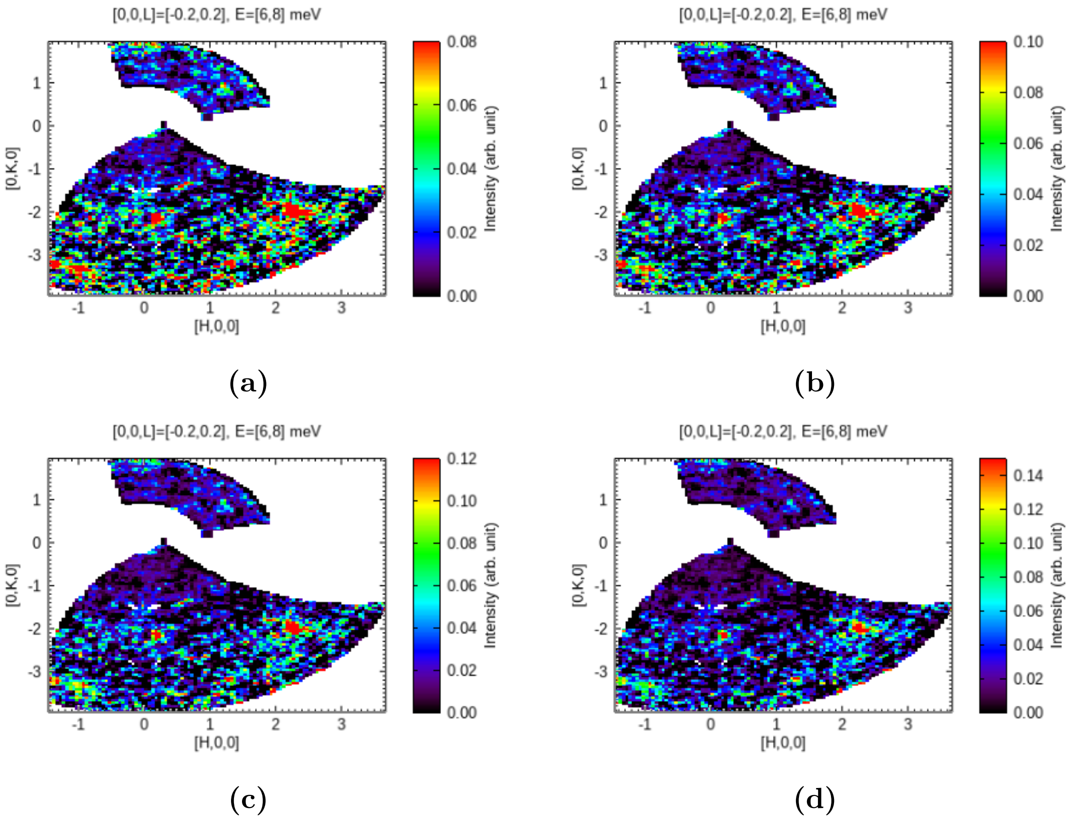

(a)

(b)

(c)

(d)

Figure 9.6: 3K overview of the phonon spectra with background subtraction at increasing intensity ranges (see scale on the right).

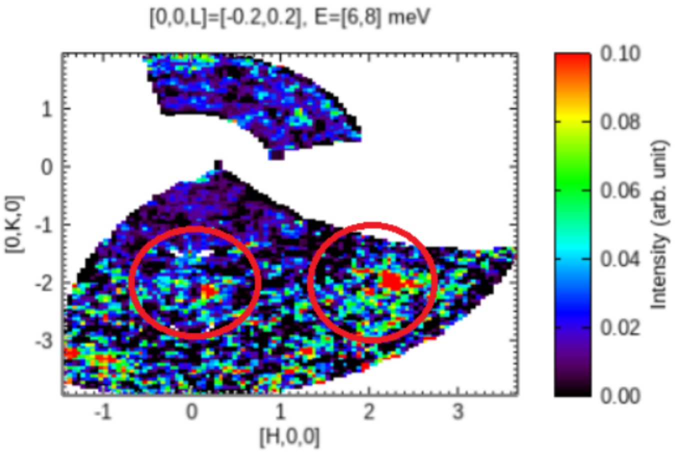

Figure 9.7: 3K overview of the phonon spectra with circles on the two phonons at H=0 and H=2, and both at approximately K=-2, analysed in the next paragraphs.

9.2.1 Phonon at H=0

In order to analyse the whole 3D space, the dispersion has been plotted along three main directions (H,K,L), at first near the localized phonon around H=0 and K=-2, with an integration range of ±1 along both the K and L directions and then further intervals are discussed. Several cuts have been done in the analysis process, here the most relevant ones are presented.

Dispersion along the K direction

The whole energy range has been plotted along the K direction with and without the background in Fig. 9.8. The green blur present at approximately 20 meV on the left of Fig. 9.8 is disappearing when subtracting the background hence it is linked to the empty can and not to the single crystal studied. In Fig. 9.8 the intensity ranges are changed from left to right, in order to clearly see the features. The left of Fig. 9.8, with intensity between 0-0.10 a.u., leads to a very intense blur which does not allow to see any phonon branch. A zoom on the relevant energy range is done in the next cuts, neglecting the negative energy values and also the values above 30 meV, that does not seem to contain any feature of interest.
In Fig. 9.8, (0, -2, 0) Bragg peak is clearly seen, both if the color scale is zoomed out and by the "tails" going out from it top left and bottom right.

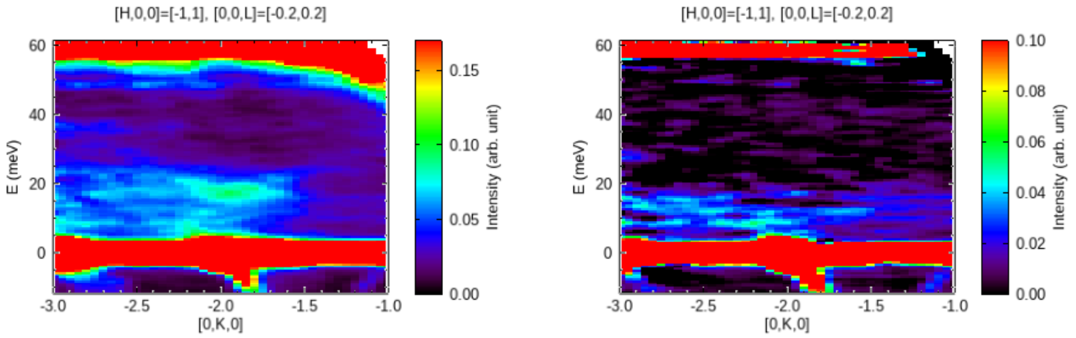

Figure 9.8: Comparison between E along K. Left: Without background subtraction. Right: With background subtraction.

In Fig. 9.10 it is possible to see the phonon dispersion along the K axis for a range between 0-30 meV. The same result is shown for two different intensity ranges, 0-0.08 a.u. on the left and 0-0.10 a.u. on the right column. In Fig. 9.10(c) and (d), the H range is halved and the features appear more clear. Both the acoustic and optics modes are visible, especially in Fig. 9.10(c) where the right acoustic branch is coming out sharply from the phonon and the optics mode form a double bridge shaped branch on the top, creating almost a complementary shape as shown in Fig. 9.9.

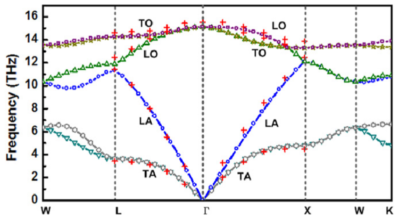

Figure 9.9: A phonon dispersion relation for Silicon. It has been used to have a reference of the shape of the dispersion relation when following the flow of the discussion. From [59].

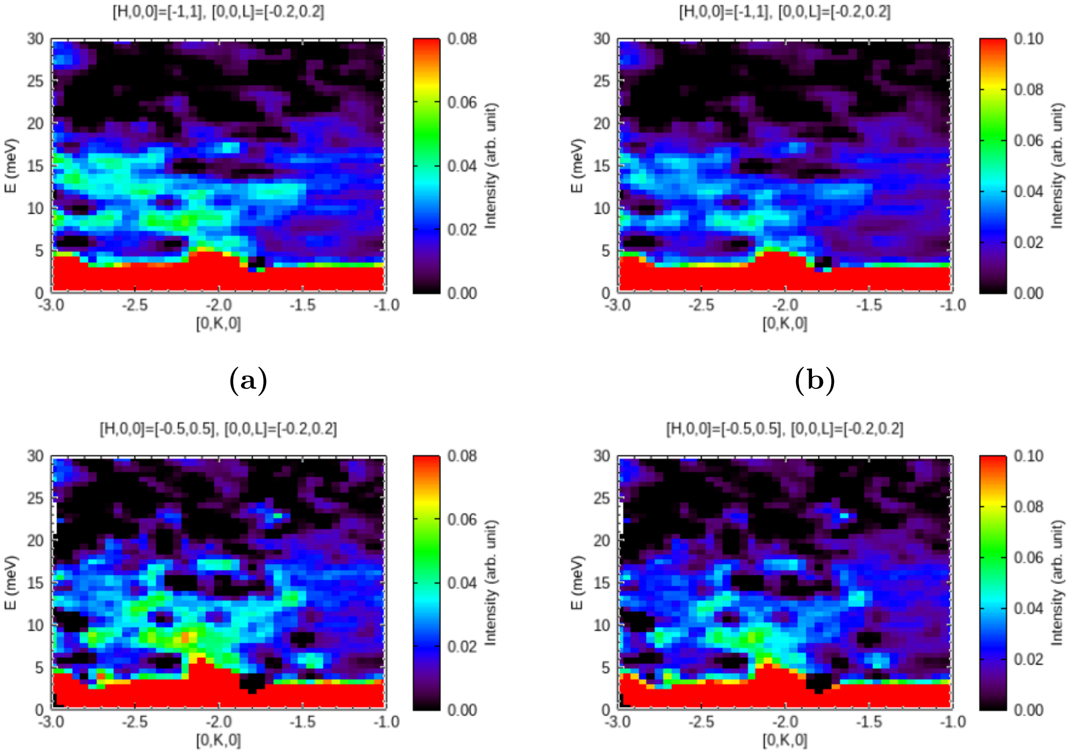

(a)

(b)

(c)

(d)

Figure 9.10: (a) Dispersion along K with intensity range [0,0.08]. (b) Dispersion along K with intensity range [0,0.10]. (c) H range is halved for intensity range [0,0.08]. (d) H range is halved for intensity range [0,0.10].

The green clouds at approximately 15meV, shown on the left of Fig. 9.10(a),

disappears when the H range is halved, linking the 15meV modes to the values of higher H.
The same cuts have been taken with double the L range as seen in Fig. 9.11. This however does not seem to improve the features; instead they appear more broad and unclear. This seem to prove that it is better to take a narrower L range symmetric and closer to the origin. From Fig. 9.11(c) and (d) the acoustics branches are quite clear and visible. Moreover, the blur present around 15meV is not disappearing like in Fig. 9.10(c), which links it also to value of high L.

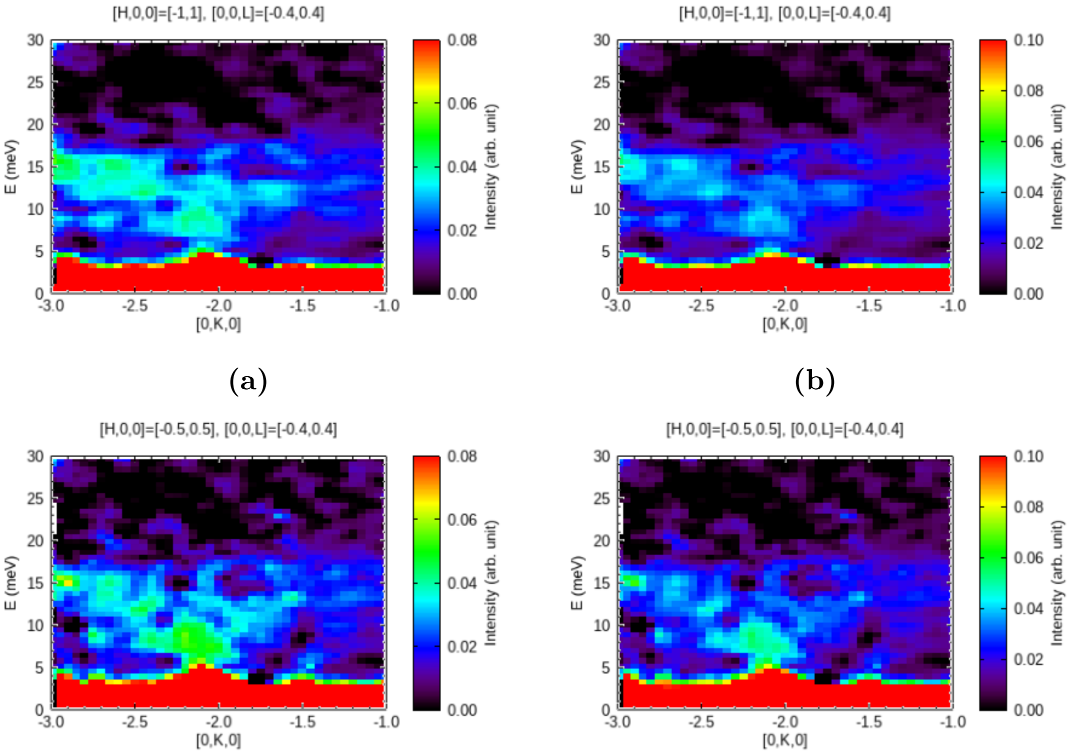

(a) (b)

(c) (d)

Figure 9.11: Dispersion along K. The L integration range is doubled with respect to figure 9.10. (a) Dispersion along K with intensity range [0,0.08]. (b) Dispersion along K with intensity range [0,0.10]. (c) H range is halved for intensity range [0,0.08]. (d) H range is halved for intensity range [0,0.10].

By narrowing down the H range around [-0.2, 0.2], the intensity of the acoustic modes become more sharp and strong when L=[-0.2,0.2], moreover, the uncertainty is reduced compared to before by integrating on a narrower range (see Fig. 9.12). Instead on the right of Fig. 9.12 the features are not as clear as when using a narrower range of L, however the left acoustic branch is quite continuous.

The analysis leads to the conclusion that along the K axis the shape and intensity of the features is more clear in Fig. 9.10(c), compared to the other cuts studied. There are two sharp acoustic branches coming out of the Bragg point and signs of optical branches around 12-13 meV that seem to fall on the acoustic modes. More optical modes could be present around 15 meV and slightly above.

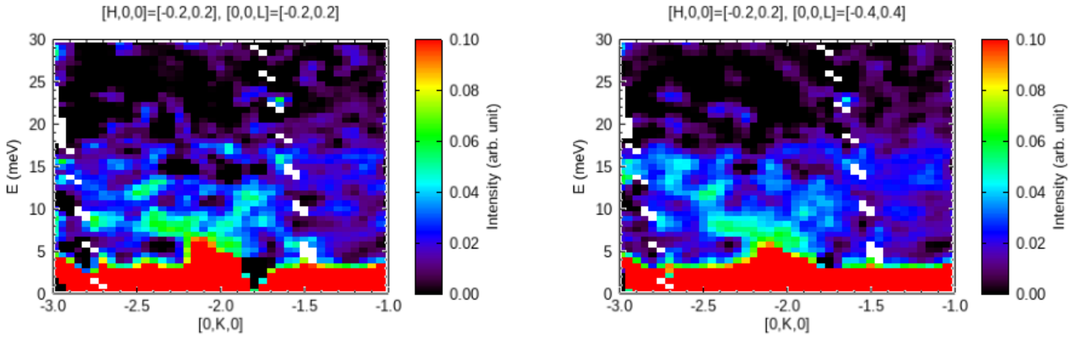

Figure 9.12: Dispersion along K. The H integration range is narrowed down to [-0.2,0.2] with respect to figure 9.10. Left: L range is [-0.2,0.2]. Right: L range is [-0.4,0.4]. The white pixels are probably due to detector tube failure, as they have a regular shape at the same angle.

Dispersion along the H direction

When plotting the dispersion along the H axis without background subtraction [left of Fig. 9.13], there is a strong 20 meV signal that disappears with background subtraction, as seen on the right of Fig. 9.13. Instead a 10-15 meV signal arises when subtracting the background, linking the previous 20 meV signal to the empty can and not the single crystal. On the right of Fig. 9.13, it is possible to observe the weak signal emerging after the background subtraction, accordingly the intensity is lower (see the scale on the right).
Similarly to the energy analysis along the K direction, the intensity range needs to be different in order to be able to see clearly the features.
A zoom between 0-30 meV has been done in order to concentrate the attention on the energy range of interest.

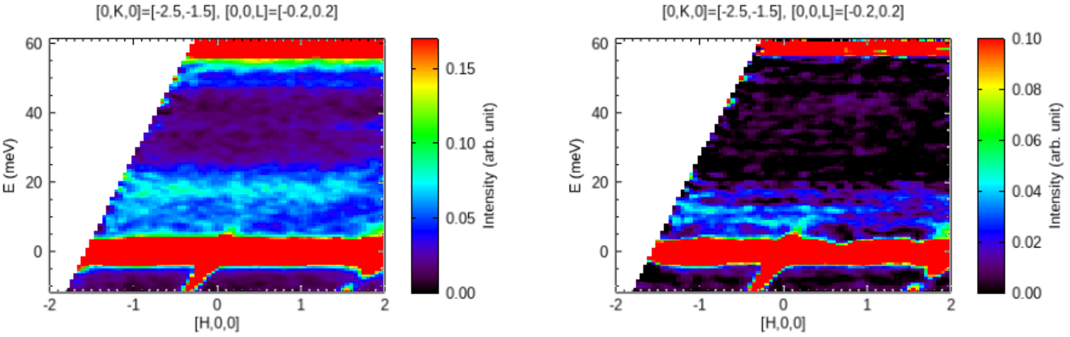

Figure 9.13: Comparison between E along H. Left: Without background subtraction. Right: With background subtraction.

Also in Fig. 9.14 a zoom on the energy range between 0-30 meV has been performed in the range H=[-1,1]. The same result is shown for two different intensity ranges, 0-0.8 a.u. on the left and 0-0.10 a.u. on the right column. There is a lower mode that may have a dispersion down to zero at the Bragg point, which makes it an acoustic mode.

In Fig. 9.14(c) and (d), the K range is narrowed down compared to Fig. 9.14(a) and (b). The features seem to improve in intensity but not in sharpness. The branches appear more flat compared to the previous K direction analysed, especially the left one, they are likely optical branches with very weak dispersion.

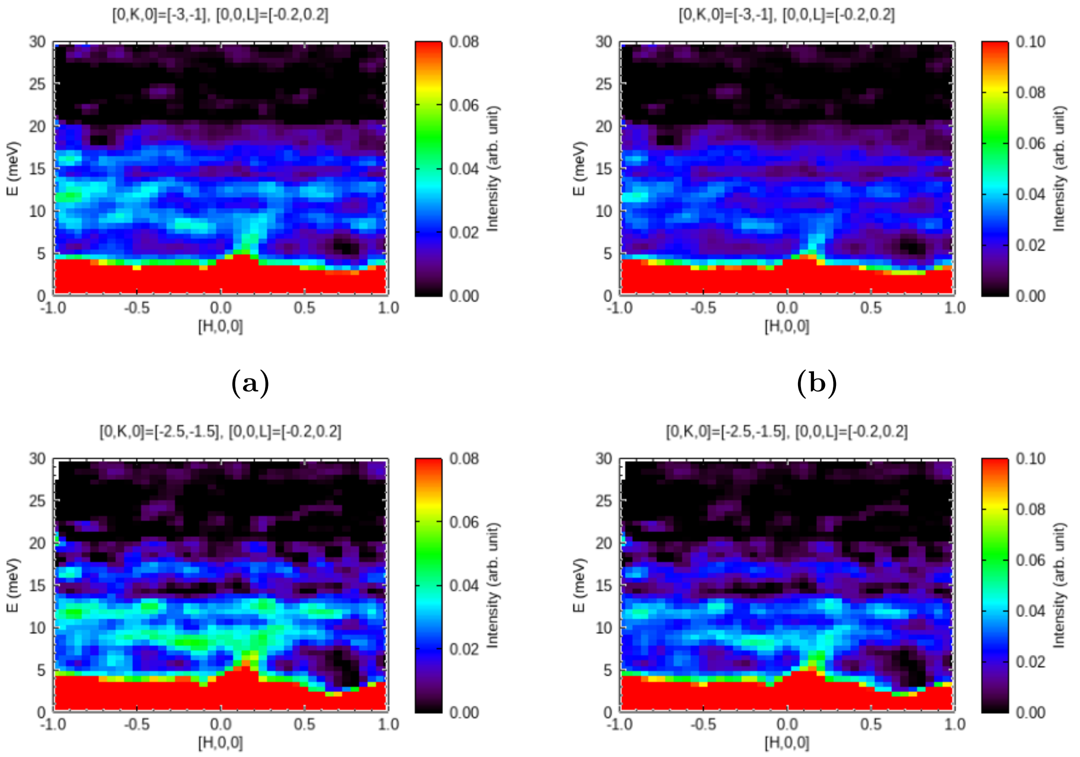

(a) **(b)**

(c) **(d)**

Figure 9.14: (a) Dispersion along H for intensity range [0,0.08]. (b) Dispersion along H for intensity range [0,0.10]. (c) K range is halved with respect to (a) and (b), for intensity range [0,0.08]. (b) K range is halved with respect to (a) and (b), for intensity range [0,0.10].

The same cuts have been taken with double L range as seen in Fig. 9.15, the modes appear more broad but, at the same time some, features get more clear, e.g. it is now clear that there is nothing at 20 meV. Fig. 9.15(d) shows clear acoustics branches. Optics lines are more visible thanks to the intensity increase, especially in Fig. 9.15(a). Continuity between the features building the branches is more clear in these results. The intensity range used here is lower than usual as at a range between 0-0.1 a.u. the features were already disappearing.

In Fig. 9.16 it is possible to see that by narrowing down the K range around [-2.2, -1.8], it does not seem to improve the sharpness of the feature. On the right of Fig. 9.16 the acoustic branches seem less pixelled compared to the left. The right hand side of the acoustics branch seems almost to split in two at higher energy. Optics modes are imperceptible.

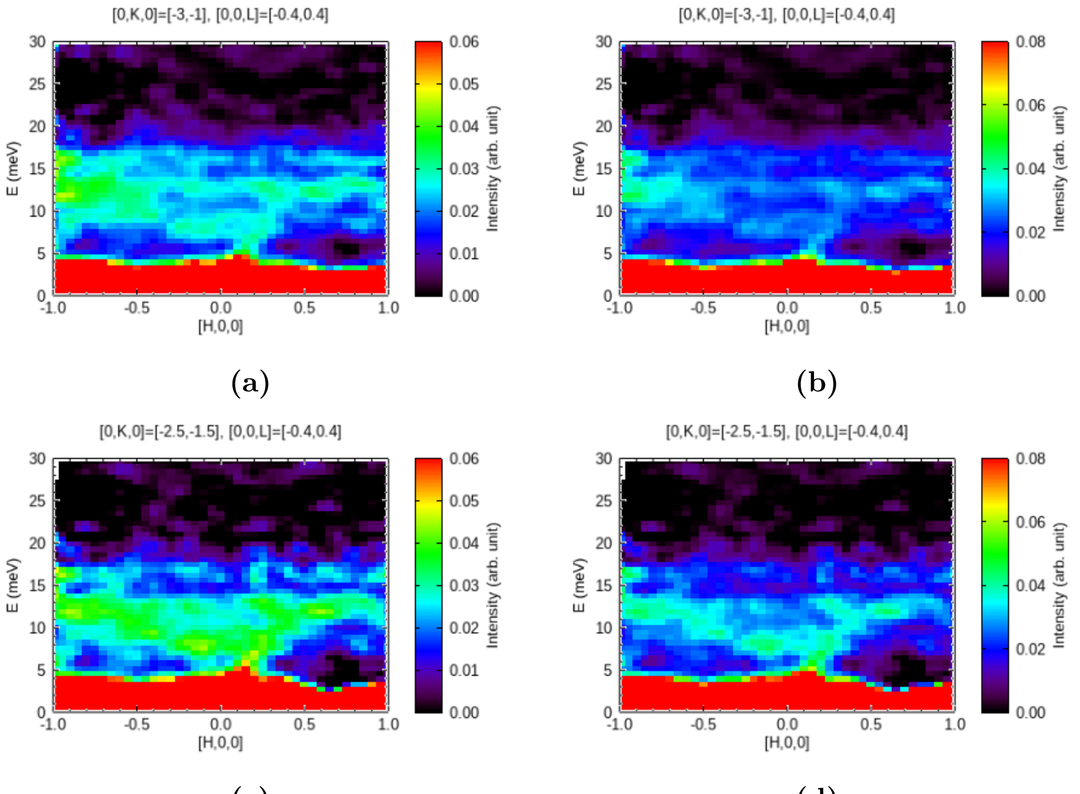

(a) **(b)**

(c) **(d)**

Figure 9.15: L range is [-0.4, 0.4]. (a) Dispersion along H for intensity range [0,0.08]. (b) Dispersion along H for intensity range [0,0.10]. (c) K range is halved with respect to (a) and (b), for intensity range [0,0.08]. (d) K range is halved with respect to (a) and (b), for intensity range [0,0.10].

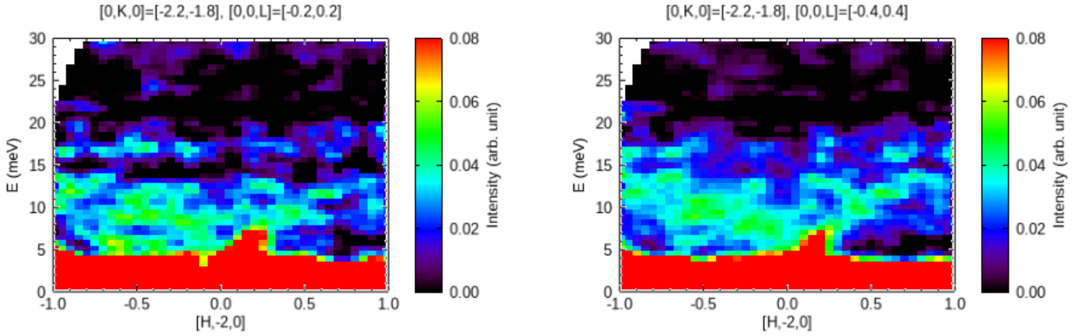

Figure 9.16: K range narrowed down to [-2.2,-1.8]. Left: Dispersion along H with L range [-0.2,0.2]. Right: Dispersion along H with L range [-0.4,0.4].

The analysis leads to the conclusion that along the H axis the best features can be seen in Fig. 9.14(c) and 9.15(d). There are two strong acoustic branches coming out of the Bragg point (unclear for the left branch), but they are very flat compared to the dispersion along K. Weak flat optical branch between 10-15 meV might be present. Another possible optical branch could be present just above 15 meV.
A general overview of the modes along the H axis is shown in Fig. 9.17 where at H=0 there are flat acoustic and optical modes whereas at H=2 a clear and sharp branch of the acoustic modes appears. As the intensity is proportional to the square of $\vec{Q}$, in this case to H^2+K^2, the intensity at high values of H is larger compared to intensity at low value of H, the features are much more visible on the right of Fig. 9.17. In order to have a homogeneous range of intensity it would be necessary to divide all the data by the respective H^2+K^2.

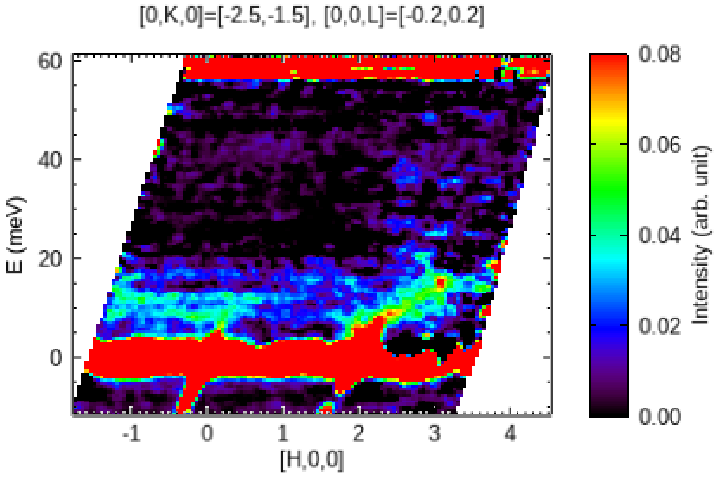

Figure 9.17: Energy overview along the entire H axis, features for both phonons at H=0 and H=2 appear.

Dispersion along the L direction

It is not easy to see the phonon dispersions along the L direction, the H and K integration ranges are also quite big as seen in Fig. 9.18.

At first, the L range [-1,1] has been selected, as it shows good visibility of the phonon dispersion relation.

On the left of Fig. 9.18, the entire energy range is plotted while on the right of Fig. 9.18 the energy has been zoomed in the range of interest. The acoustic branches are quite clear and resembling nicely the dispersion relation fit (see Fig. 9.9), blur is present. Some higher branches at around 15 meV could be linked to the optical modes.

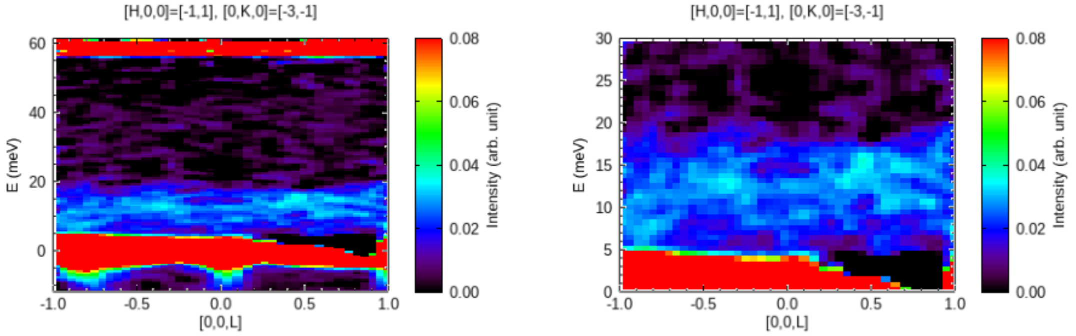

Figure 9.18: Left: Dispersion along L for intensity range [0,0.10]. Right: Dispersion along L for intensity range [0,0.10].

In Fig. 9.19(a) and (b) the H range is narrower while in Fig. 9.19(c) and (d) instead the K range is narrower, both with respect to Fig. 9.18. This lead to sharper features and more clear branches. Therefore decreasing the interval of integration of H and K leads to an improvement of the plot and something more similar to what is expected is found (see Fig. 9.9).

The outcomes suggests to plot other cuts with both H and K range even more narrower, and this has been done in Fig. 9.20. This seems to go towards an improvement of the visibility of the acoustics and optical branches of interest.

The analysis leads to the conclusion that along the L axis the best features can be seen on the left of Fig. 9.20, since it is possible to see more clearly two branches (around 8 meV and 12 meV). The dispersion along the L direction is the one that better seems to fit the dispersion relation for the acoustic modes. Optics mode are more visible along the K and H directions.

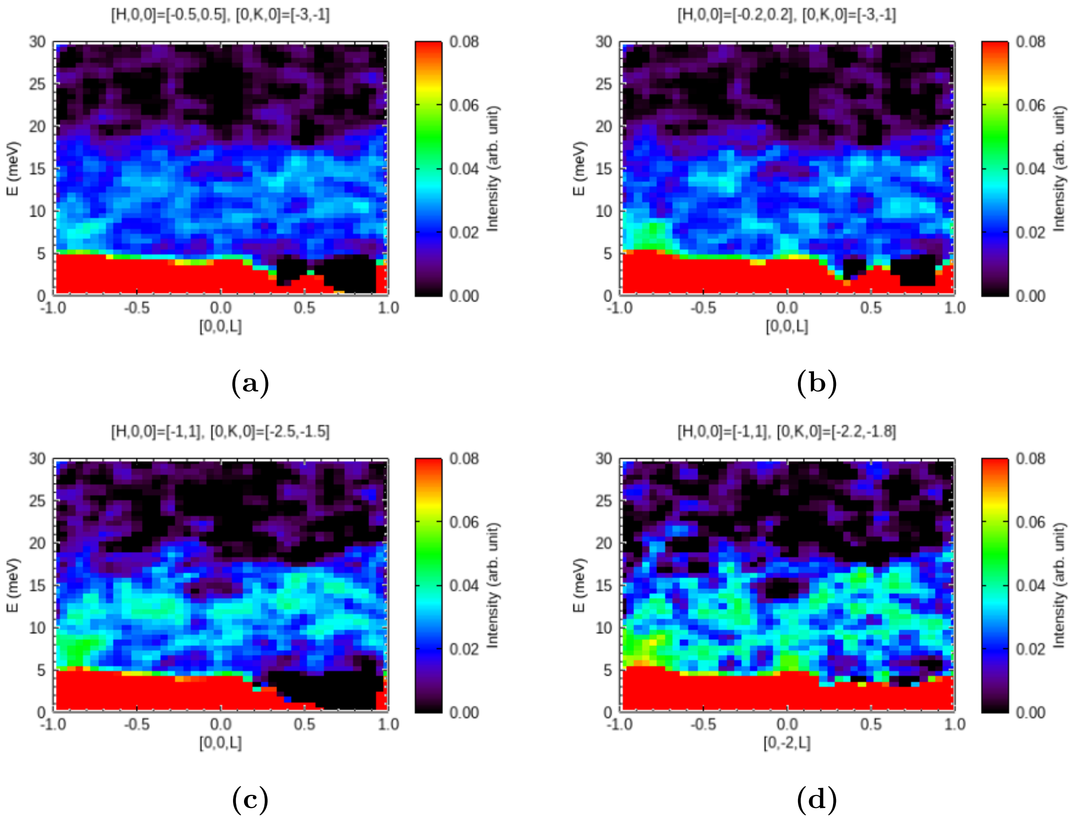

(a) **(b)** **(c)** **(d)**

Figure 9.19: (a) H range halved and K range kept constant, with respect to Fig. 9.18. (b) H range halved again and K range kept constant. (c) K range halved and H range kept constant, with respect to Fig. 9.18. (d) K range halved again and H range kept constant.

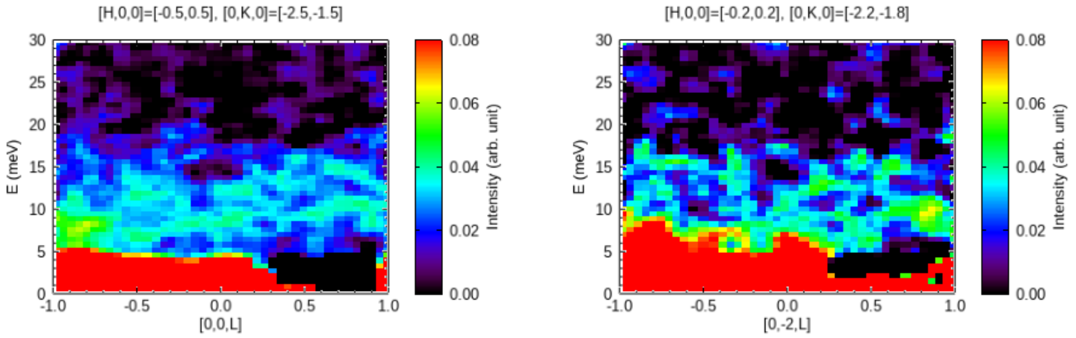

Figure 9.20: Left: Both H and K range are halved from their initial value used in Fig. 9.18. Right: Both H and K range are decreased from their values on the left.

9.2.2 Phonons at H=2

Dispersion along the K direction

In Fig. 9.21 it is possible to see the features at two different intensity ranges on the left and right column. The left acoustic branch appears sharp and clear, the right branch curvature is also visible and its shadow seems to have a consistent shape with the dispersion relation expected. The left branch has higher intensity compared to the right one, as already said previous, because the intensity is proportional to $\vec{Q}^2$ therefore as we take the absolute value and the direction is squared, this is giving an higher contribution at lower values of K, the direction in Q which is analyzed. The optical modes are very weakly visible in these intensity ranges, in order to see them it would be necessary to increase the intensity range but this would lead to hard differentiation of the features appearing in the figures. The blur between 10 and 17meV on the left of Fig. 9.21 could be related to the presence of the optical branches, moreover, around 15 meV there seems to be a weak optical branch along the entire K direction.

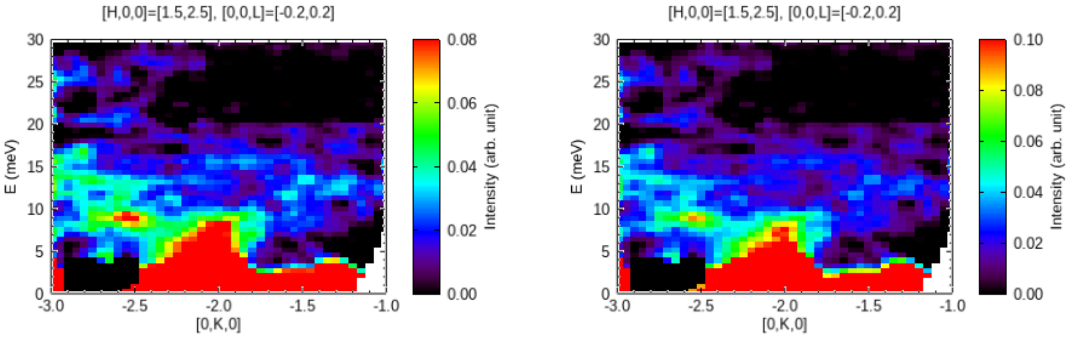

Figure 9.21: Right: Phonon spectra in the range [0,30]meV with I= [0,0.08]. Left: Phonon spectra in the range [0,30]meV with I= [0,0.10].

The same cuts have been performed doubling the L range to [-0.4,0.4], however no mayor improvements have been observed, the blur is a little bit more intense but the shape and intensity of the features seems to be the same as before, as shown in Fig. 9.22.

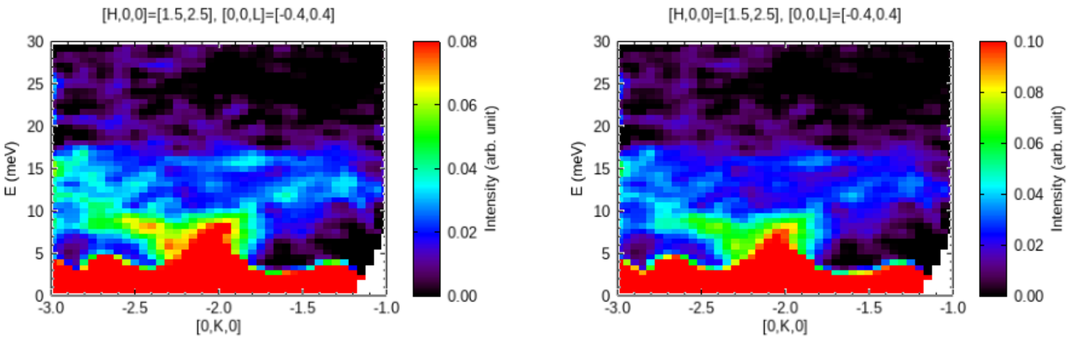

Figure 9.22: L integration is doubled. Left: Phonon spectra in the range [0,30]meV with I= [0,0.08]. Right: Phonon spectra in the range [0,30]meV with I= [0,0.10].

In Fig. 9.23 the H range is narrowed down to [1.8,2.2] for two different L ranges on the left and on the right. This is decreasing the continuity of the acoustic branches compared to the previous cuts.
In conclusion, the best cuts along K direction for the H=2 phonon can be seen on the left of Fig. 9.21 and of Fig. 9.22, where the acoustic branch sharply comes out of the Bragg point and there is a hint for optical modes at higher energies.

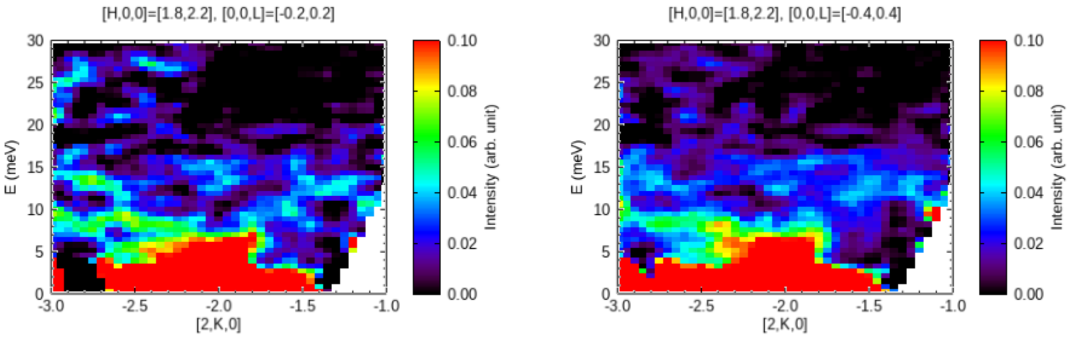

Figure 9.23: H is narrower to [1.8,2.2]. Left: Phonon spectra along the K direction with L range [-0.2,0.2]. Right: Phonon spectra along the K direction with L range [-0.4,0.4].

Dispersion along the H direction

Moving to the H direction, in Fig. 9.24, it is possible to observe the acoustic branches. The right branch has higher intensity for the same dependence of the intensity to $\vec{Q}^2$ already mentioned above; this time it is on the right as the H values taken into account are positive. In general, if there is a very strong branch only at one side out from the Bragg peak, there could be a risk that the scattering is a non-physical artefact of the instrument (a "spurion"). Therefore, in order to make sure that the scattering is physical, there needs to be also a hint of scattering on the other side. This seems to be evident on the left of Fig. 9.24 and Fig. 9.25 where an additional feature is present. Another check that has been done was to change the intensity range in order to be able to see the branch on the left.

The optical branches are instead poorly visible. The intensity range should be decreased even more to see them clearly but this would result in disordered features appearing from the phonon branches without a clear distinction between the acoustic and optical modes. The same cuts have been performed at two different intensity ranges on the left and right column of Fig. 9.24.

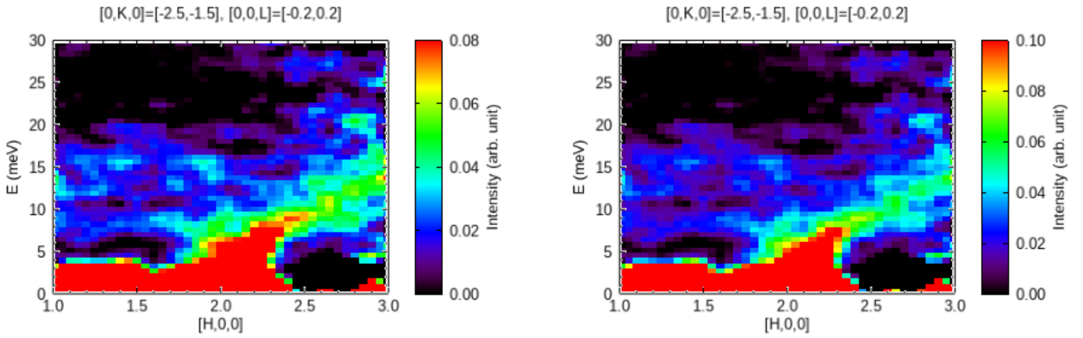

Figure 9.24: Left: Phonon spectra in the range [0,30]meV with I= [0,0.08]. Right: Phonon spectra in the range [0,30]meV with I= [0,0.10].

In Fig. 9.25 the L range has been doubled to [-0.4,0.4]. The width of the acoustic branch is quite wide.

Some cuts have been performed also at a very narrow range around K=-2 (centre of the phonon) with both L=[-0.2,0.2] and L=[-0.4,0.4]. The intensity increases and it is not possible to see any improvements compared to the previous analysis.

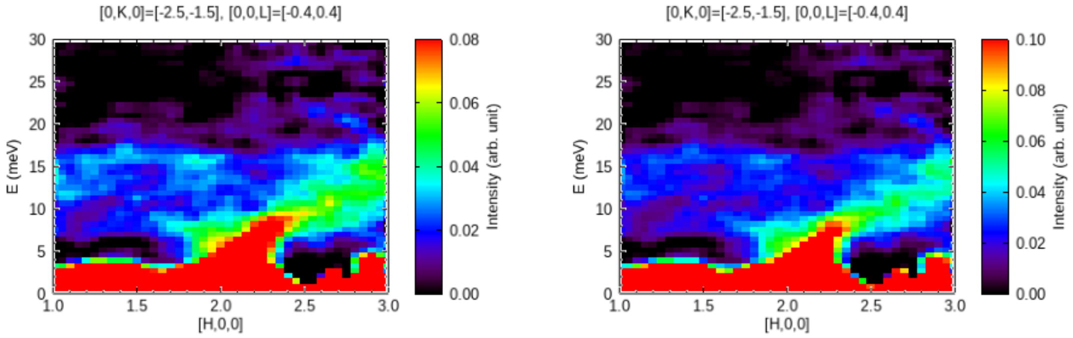

Figure 9.25: L integration is doubled. Left: Phonon spectra in the range [0,30]meV with I= [0,0.08]. Right: Phonon spectra in the range [0,30]meV with I= [0,0.10].

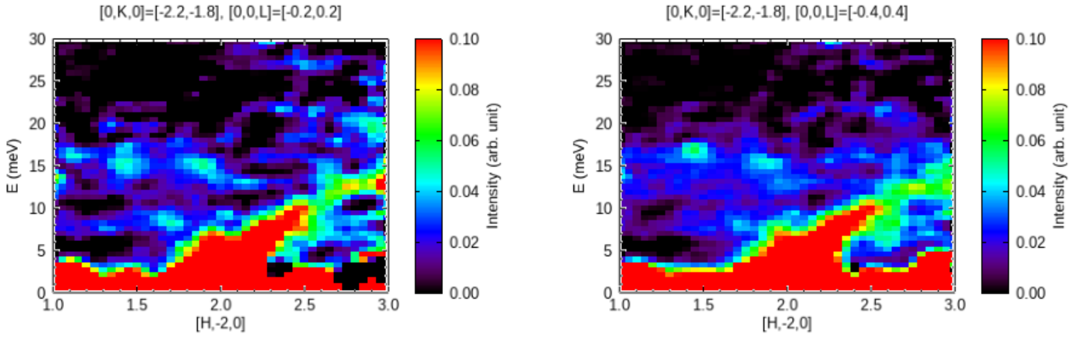

Figure 9.26: K is narrower to [-2.2,-1.8]. Left: Phonon spectra along the H direction with L range [-0.2,0.2]. Right: Phonon spectra along the H direction with L range [-0.4,0.4].

Dispersion along the L direction

Along the L direction, the phonon modes are much more clear compared to the previous cuts along H and K, leading this to be the preferred direction in order to see the phonon dispersion relation.
Compared to the previous directions, the smoothing factor has been here decreased to 1 in order to have a better overview of the phonon spectra in terms of quality of the figures, however this increases the pixelling and the discontinuity between the features.
Once the phonon has been localized, the integration on the H and K direction has been narrowed down, to see if any improvements in the features appear. In Fig 9.27(a) and (b) it is possible to observe clear acoustic branches coming out of the Bragg point, however the features with high intensity are many therefore the

branches are still hidden, moreover there is not a clear distinction between acoustic and optical branches at first sight. The integration ranges of H and K are different on the left and right of the figure in order to see if any relevant changes occur. The narrower the H range, the more clear the dispersion relation seems to be.
In Fig 9.27(c), the acoustic branches are sharp and clearly visible and close to the dispersion relation expected. Optical branches instead are poorly visible however the disappearance of the features in between the acoustic branches makes the figure more clean and the acoustic branches more clear. Around 15 meV there is a concentration of brighter features which could be signatures of optical modes.

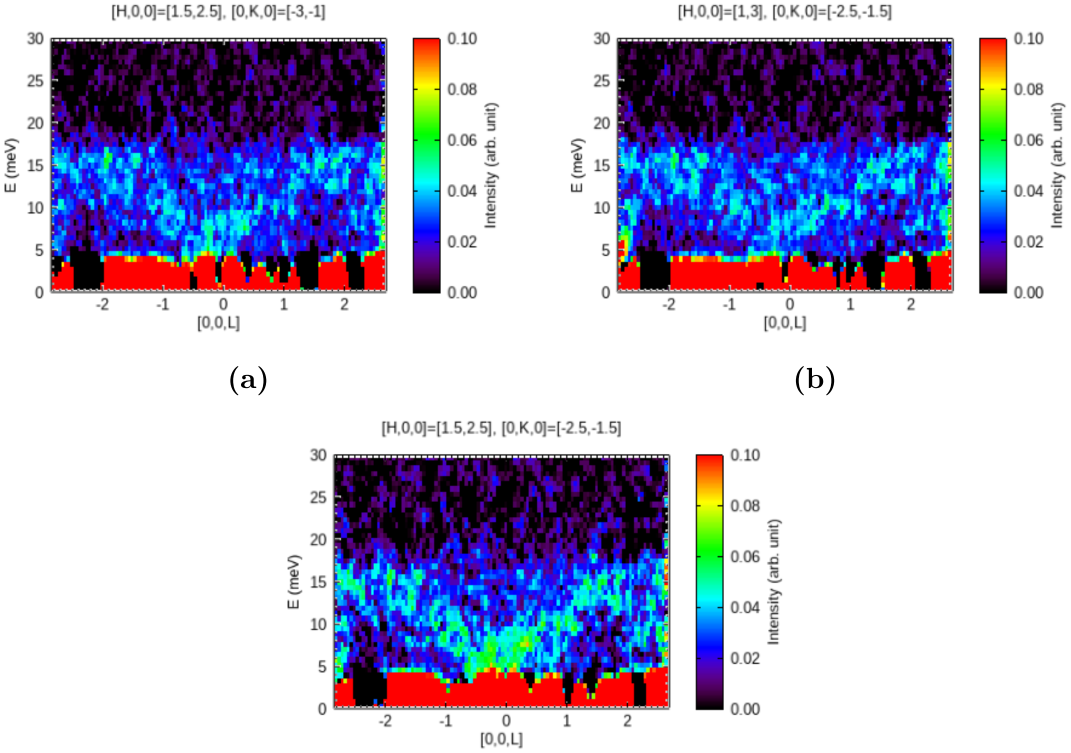
[H,0,0]=[1.5,2.5], [0,K,0]=[-3,-1]

[H,0,0]=[1,3], [0,K,0]=[-2.5,-1.5]

[H,0,0]=[1.5,2.5], [0,K,0]=[-2.5,-1.5]

(a) **(b)**

(c)

Figure 9.27: Phonon spectra in [0,30]meV range along the entire L direction with background subtraction. (a) H range is [1.5,2.5] for intensity range [0,0.10]. (b) K range is [-2.5,-1.5] for intensity range [0,0.10]. (c) Phonon spectra along the entire L range with energy [0,30] meV, H=[1.5,2.5] and K=[-2.5,-2.5].

In Fig. 9.28 the cuts of the phonon spectra have been done with a range of ±0.2 around the centre of the phonon situated at H=2 and K=-2, at first only along one of the two integrated directions (see Fig. 9.28(a), (b)) and then for both directions (see Fig. 9.28 (c)). Fig. 9.28(a)and (b) look all quite similar with clear acoustic

branches and slightly visible optical branches around 15 meV. There is a clear improvement compared to Fig. 9.27 in intensity and sharpness.
Where both intervals are narrowed down in Fig. 9.28(c) the intensity and pixelling increases leading to branches less visible compared to the previous cuts but the optical one seems more evident.

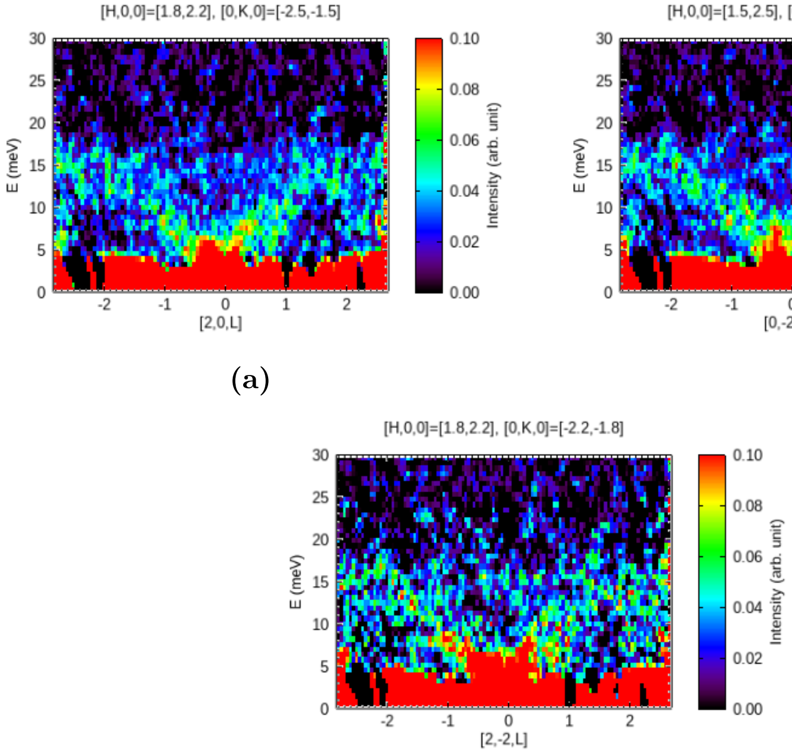

(a) **(b)**

(c)

Figure 9.28: The integration range around H and K has been narrowed down to an interval very close to the centre of interest. (a) H range is [1.8,2.2] for intensity range [0,0.10]. (b) K range is [-2.2,-1.8] for intensity range [0,0.10]. (c) Phonon spectra in H=[1.8,2.2] and K=[-2.2,-1.8] for intensity range [0,0.10].

9.3 Comparison with 85 K and 220 K

The same type of analysis seen for the dispersion relation at 3 K has also been performed at 85 K and 220 K. Here only the most relevant results will be presented, assuming that some of the best integration ranges along the three dimensions in the space have been found. Moreover, several 1D cuts along the dimension in space taken into account (x axis) of 2 meV have been done in order to select the points in space with highest intensity (white points in the maps) and therefore see where the branches should be, however this is only a guide for the eye. The results of the investigation are illustrated in this paragraph.

9.3.1 Phonon at H=0

Dispersion along the K direction

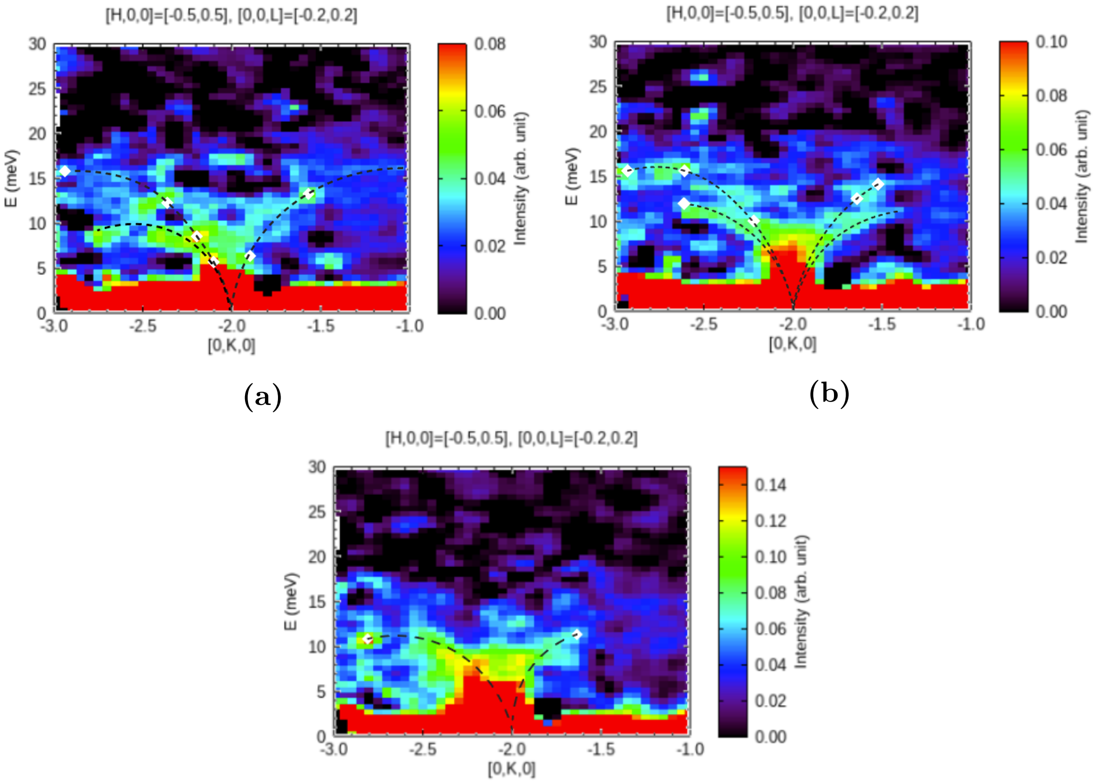

(a) (b)

(c)

Figure 9.29: (a) Dispersion along K at 3 K with intensity range [0,0.08]. (b) Dispersion along K at 85 K with intensity range [0,0.10]. (c) Dispersion along K at 220 K with intensity range [0,0.15].

In Fig. 9.29, the dispersion relation along K at three different temperatures has been plotted. In all the three plots, also some weak optical modes are visible, around 12-13 meV and 16 meV. The optical branch is less visible at 220 K where instead only the left acoustic branch is clearly visible, the right one is only partly there, this should be due to the dependence of the intensity to $\vec{Q}^2$. The branches come out of the Bragg point, which is at K=-2 and H=0. Along the K direction, it is expected to see the longitudinal acoustic modes.

Dispersion along the H direction

Along the H direction, the acoustic branches are clearly visible for both Bragg points (0,-2,0) and (2,-2,0). The plot in Fig. 9.30 shows the dispersion relation along the entire H direction.

In Fig. 9.30(b) a nice continuous line between the two acoustic branches of the left and right Bragg points is present. The red "tails" going out from its top left and bottom right show the position of the point of interest. Above 20 meV, almost no features are present, therefore that intensity range is almost never taken into account in this work.

As the temperature is increased, the features appear more blurred and the branches are less sharp.

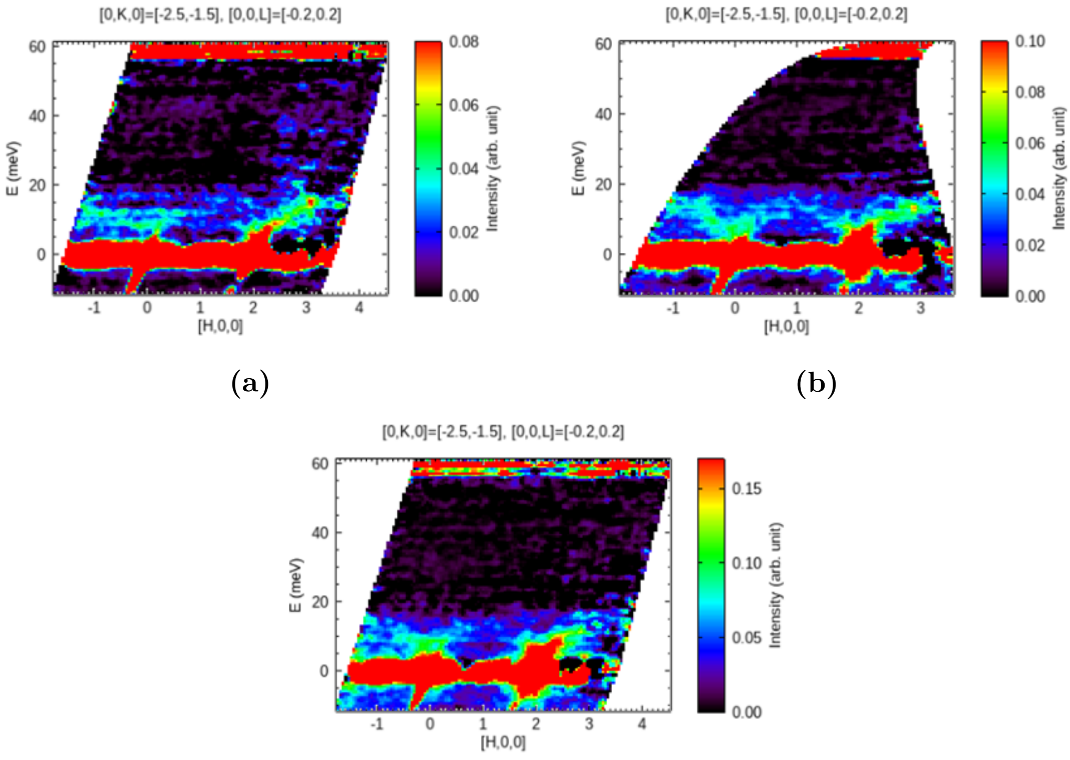

(a) **(b)**

(c)

Figure 9.30: Dispersion overview along the entire H axis, features for both phonons at H=0 and H=2 appear. (a) At 3 K. (b) At 85 K. (c) At 220 K.

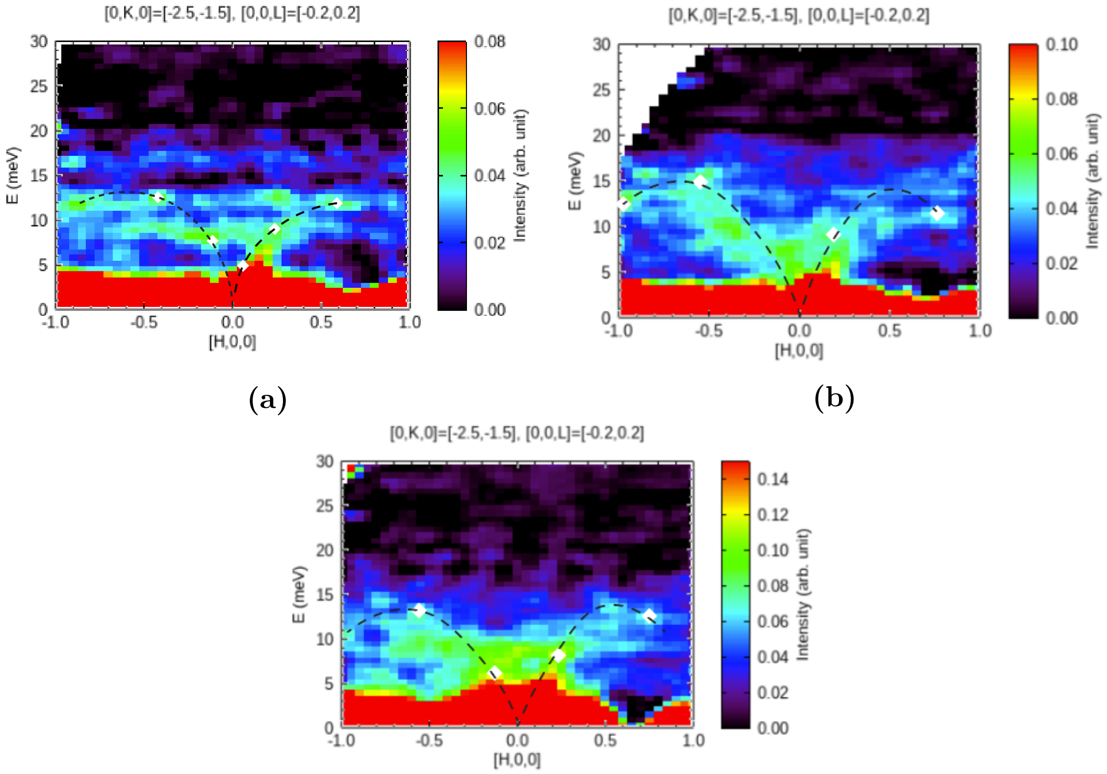

(a) **(b)**

(c)

Figure 9.31: (a) Dispersion along H at 3 K with intensity range [0,0.08]. (b) Dispersion along H at 85 K with intensity range [0,0.10]. (c) Dispersion along H at 220 K with intensity range [0,0.15].

By concentrating on the Bragg point at H=0 studied in this paragraph, it is possible to plot its dispersion relation along the H axis, as seen in Fig. 9.31. At 3 K, there are several strong intensity lines around 8 meV and 12-13 meV which could be signatures of optical modes. They tend to disappear or merge with other features as the temperature is increased, at the same time the acoustic branches become more visible and broad. Along the H direction the longitudinal modes are seen. Below 10 meV the calculations show that the acoustic and optic branches should start to overlap, making it very challenging to distinguish them.

Dispersion along the L direction

By taking H=0 and K=-2 as the center, and plotting the dispersion relation along the L direction, the features appear broad and random. The only one in which it is possible to observe by eye potential acoustic and optical branches is the one at 3 K (Fig. 9.32(a)).
It will be seen that in the case of H=2, K=-2 instead this direction will be the one where the acoustic branches will be more visible and sharp.

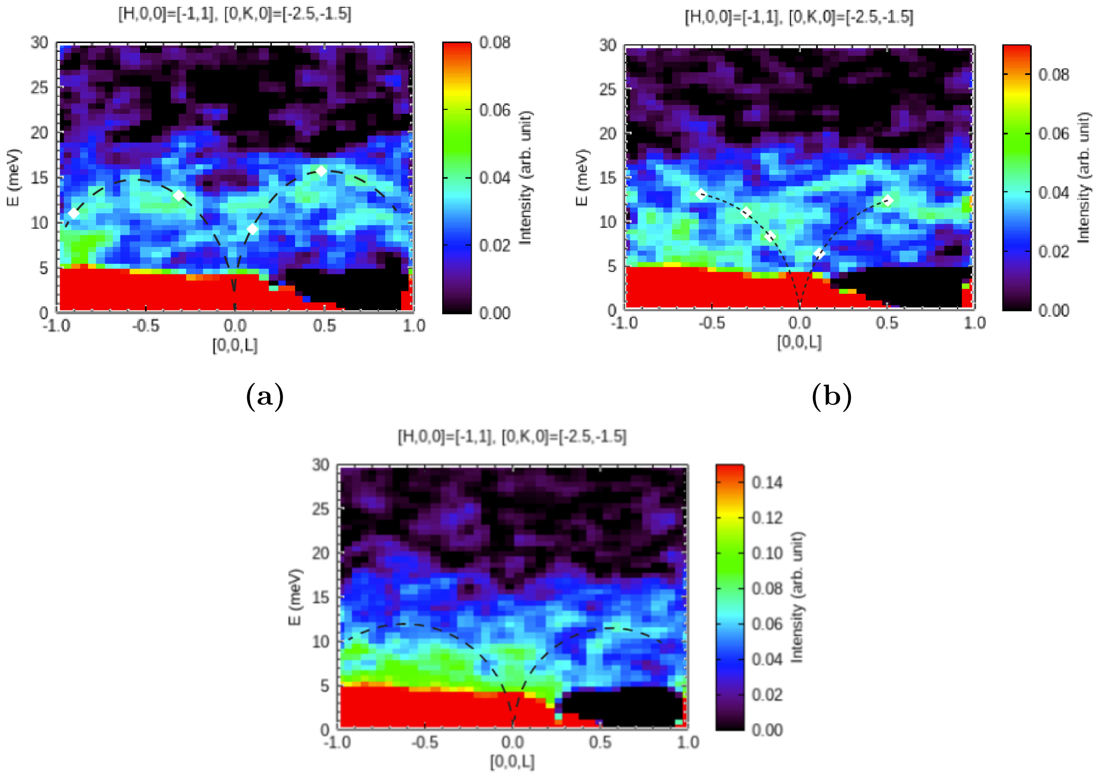

(a)

(b)

(c)

Figure 9.32: (a) Dispersion along L at 3 K with intensity range [0,0.08]. (b) Dispersion along L at 85 K with intensity range [0,0.09]. (c) Dispersion along L at 220 K with intensity range [0,0.15].

9.3.2 Phonons at H=2

Dispersion along the K direction

The same study has been done for the other Bragg point of interest, at H=2 and K=-2. In Fig. 9.33, the intensity appears very high around the center of the branches, going also up to almost 10 meV. Some weak optical branch could be seen in Fig. 9.33(a) around 15 meV.
As the temperature increases, the features are more broad and unclear.
The features along the same direction appeared more sharp and clear when investigating the region around H=0 and K=-2, as shown in Fig. 9.29.

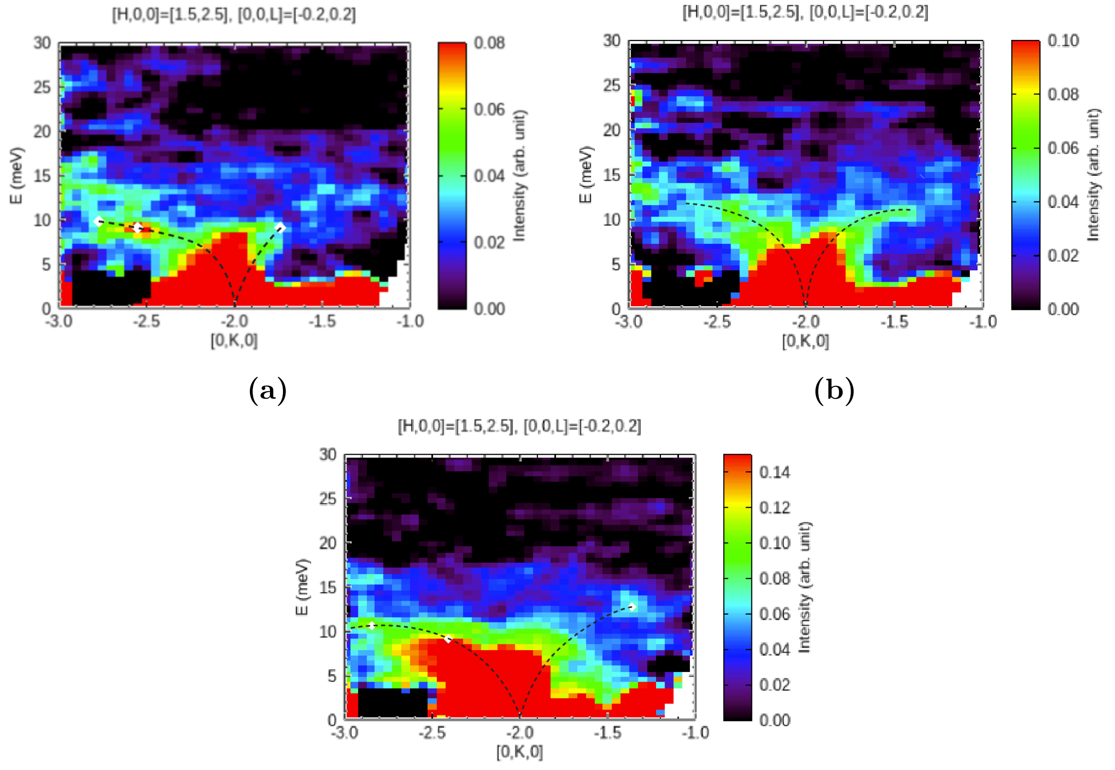

(a) **(b)**

(c)

Figure 9.33: (a) Dispersion along K at 3 K with intensity range [0,0.08]. (b) Dispersion along K at 85 K with intensity range [0,0.10]. (c) Dispersion along K at 220 K with intensity range [0,0.15].

Dispersion along the H direction

Along the H direction, especially in Fig. 9.34(a) and (c) there is a clear dependence of the intensity of the square of the $\vec{Q}$ space, leading to a strong right acoustic branch while the left one is only present around the Bragg point.

At 3 K, around 15 meV on the right of the Fig. 9.34(a), some optical branch seem to appear and weakly propagate along the rest of the H direction.

At 85 K, both the acoustic branches are visible.

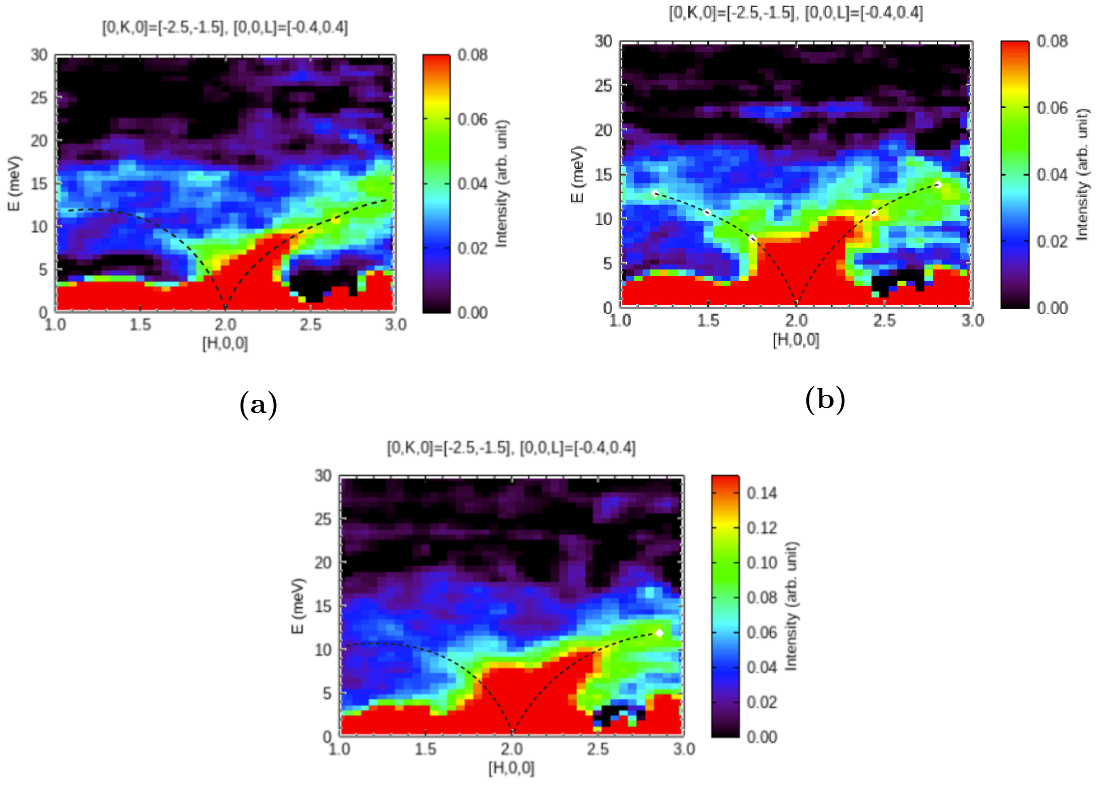

(a)

(b)

(c)

Figure 9.34: (a) Dispersion along H at 3 K with intensity range [0,0.08]. (b) Dispersion along H at 85 K with intensity range [0,0.08]. (c) Dispersion along H at 220 K with intensity range [0,0.15].

Dispersion along the L direction

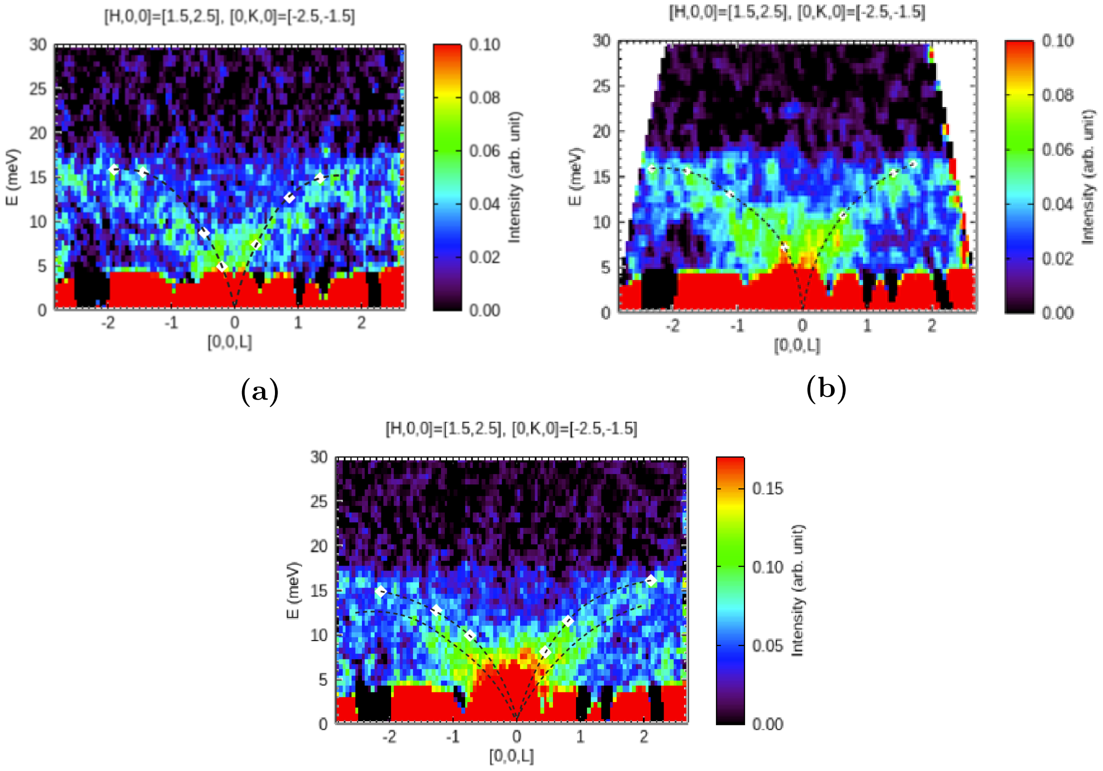

(a) **(b)**

(c)

Figure 9.35: (a) Dispersion along L at 3 K with intensity range [0,0.10]. (b) Dispersion along L at 85 K with intensity range [0,0.10]. (c) Dispersion along L at 220 K with intensity range [0,0.17].

In Fig. 9.35, the dispersion relation along L is plotted. This seem to be the most clear example of acoustic branches analysed so far. They start exactly from the center of the Bragg point and nicely come out of it in a symmetric way.
Some weak optical features might be present in Fig. 9.35(a) and (b) around 15 meV.

9.4 Subtraction of results at low temperature (3 K) from the results at high temperature (220 K)

In order to see if there are any changes between different temperatures, the results at low temperature (3 K) have been subtracted from the one at high temperature (220 K). This procedure tells if there is something at high T which is not present at low T, with positive intensity.

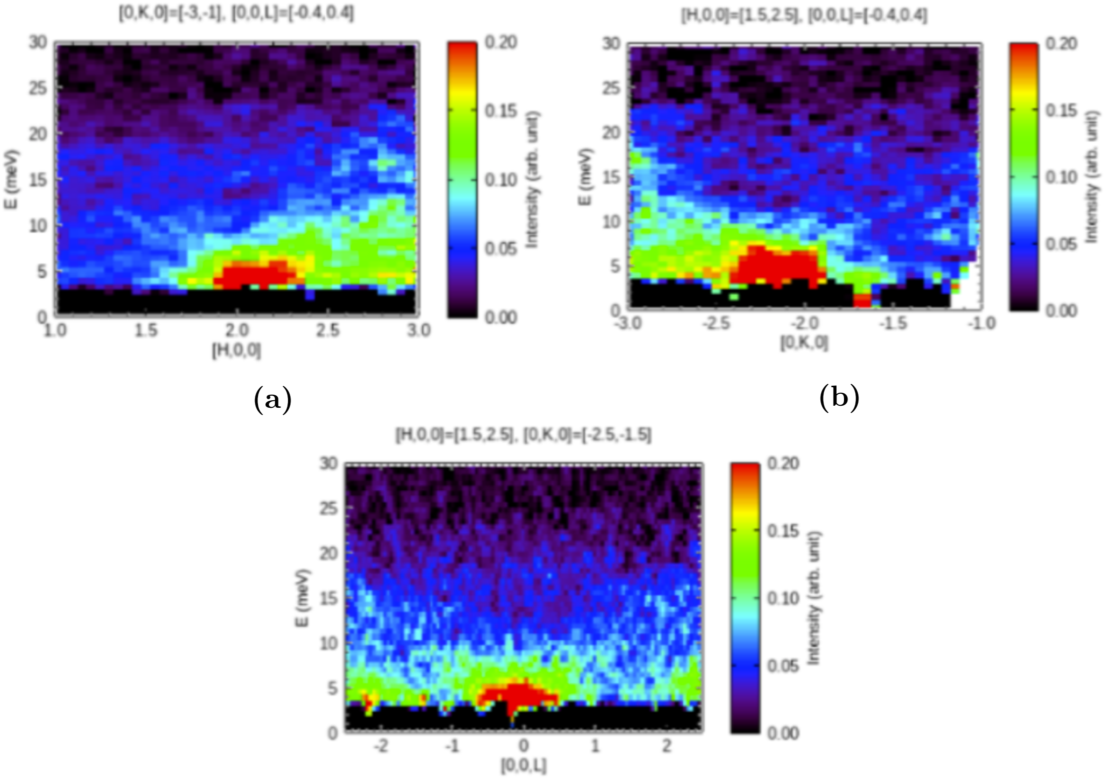

(a)

(b)

(c)

Figure 9.36: 3 K data set subtracted from 220 K data, centered at (0,-2, 0).

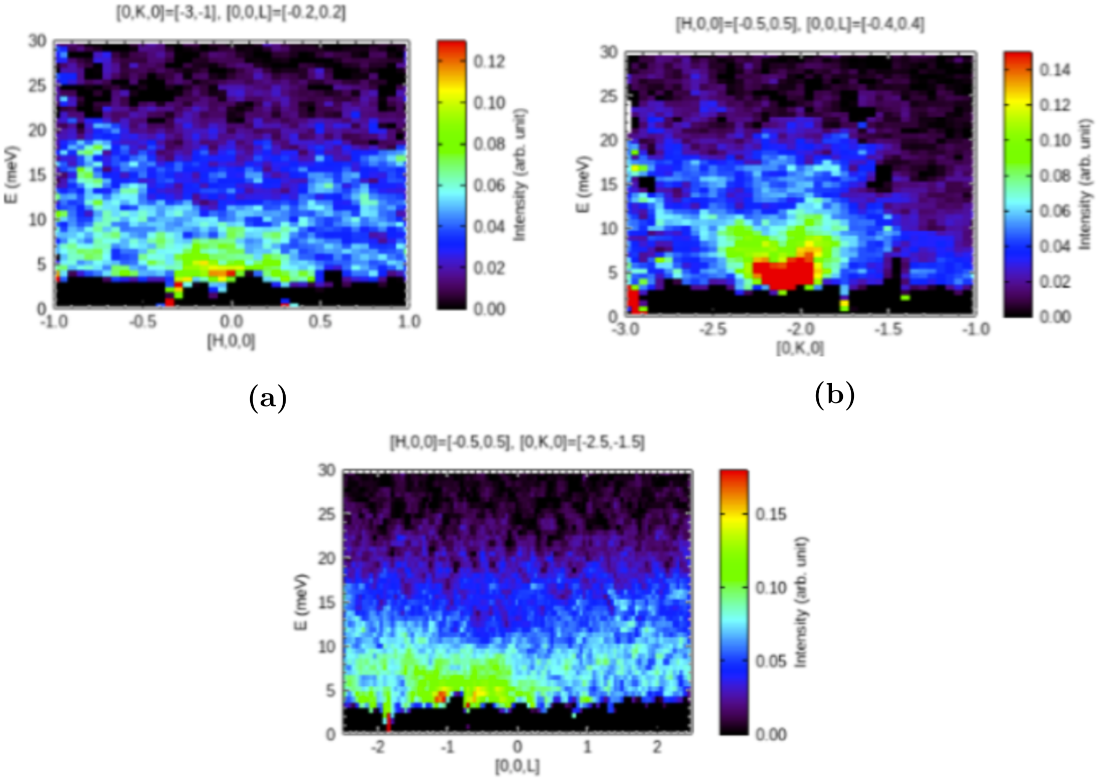

(a) **(b)**

(c)

Figure 9.37: 3 K data set subtracted from 220 K data, centered at (2,-2, 0).

In Fig. 9.36 and Fig. 9.37, the subtracted data are shown from the 2 Bragg points. We see that there is a signal at low energy transfers, close to the Bragg peak. This is likely from low-energy phonons that are amplified by temperature due to the increase of the Bose factor.

The elastic line is totally black because it has been subtracted. A strong intensity red point in the center of the Bragg point is present in almost all the plots, showing that Bragg point becomes stronger in intensity. By tuning the intensity range it is possible to see the features in a more clear way, however this has not been shown here. There is no apparent presence of optical branches; instead acoustic features are present.

9.5 Superstructure peaks

In previous studies on the single crystal $LaPt_2Si_2$ [1], X-ray diffraction (XRD) patterns show the occurrence of satellite Bragg peaks corresponding to the wave vector q ≈ [0.36, 0, 0)]. The observation is a clear evidence of lowering of the tetragonal symmetry and points to a CDW state at low temperatures [1]. From the authors' results, the satellites reveal maximum intensity at 85 K, disappear above 175 K and decline (or shifting from observable part of reciprocal space) below 85 K, as it is shown in Fig. 1.2. During the INS experiment at HRC, it was possible to acquire a map to observe the incommensurate reflections at three different temperatures.

Previously also Gupta et al.[32] studied the superlattice reflections on polycrystalline samples and found out a reflection at (n/3, 0, 0) where n = 1 and 2 below 10 K, which indicates the tripling of unit cell below CDW transition.

The 1D cuts along the H direction with respect to the intensity are shown in Fig. 9.38 at three different temperatures. In order to better understand the exact position and intensity values, a zoom on the supposed superstructure peaks has been performed and the x axis scale range has been narrowed down, as seen in Fig. 9.39.

On the H axis the peaks are at -0.35 and 0.35 in space, showing a good agreement with the q ≈ [0.36, 0, 0)] measured by XRD [1].

The values of the intensity of the peaks are:

- 3 K: left peak 5 a.u. and right peak 8.5 a.u. ;
- 85 K: left peak 5.8 a.u. and right peak 9 a.u. ;
- 220 K: both peaks at 10.5 a.u. ;

The intensity of the peaks are instead very different in trend to what was expected, as their maximum should be around 85 K and then the peaks should decrease both at higher and lower temperature (3 K and 220 K in this case). Instead the peaks from the INS data show a maximum at 220 K, and a similar lower value at both 3 K and 85 K, slightly increasing at 85 K. This is something unexpected and in contrast with the literature mentioned above.

During the experiment, it was possible to collect data for incoming energy of the neutrons at 12 meV, 23 meV and 61 meV, thanks to the use of the choppers illustrated in Fig. 7.2.

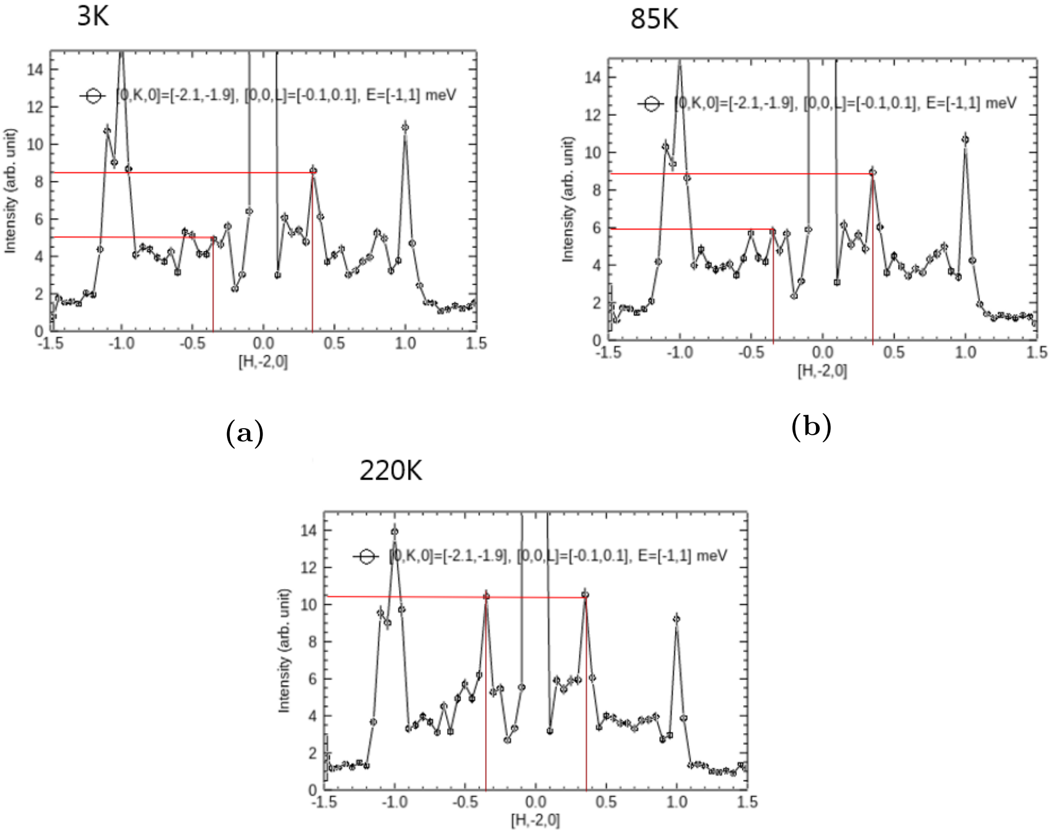

(a) **(b)**

(c)

Figure 9.38: Cut at the elastic (zero energy transfer) line with variable H to get an overview of the Bragg peaks in the crystal. (a) At 3 K. (b) At 85 K. (c) At 220 K.

The data analysed in this chapter are the ones at $E_i = 61$ meV, covering a bigger $\vec{Q}$ space and also energy range compared to the other two incoming energies. As the resolution should improve at lower energy, a check on the other two incoming energies has been done for the study of the superstructure peaks. However, in the 12 meV data, the two Bragg points of interest were not covered in space. Instead at 23 meV, the peaks were not clearly visible as their intensity was below 1 a.u.. Moreover, the incoming neutron flux was not very high at 23 meV. For completeness, also the difference between 220 K and 3 K is shown in Fig. 9.40. On the left of the same figure, the incoming energy is 61 meV, the intensity difference between the peaks is clear and intense, while on the right of the figure, the data for the incoming energy of 23 meV are shown, with an almost imperceptible difference between the data collected at the two temperatures.

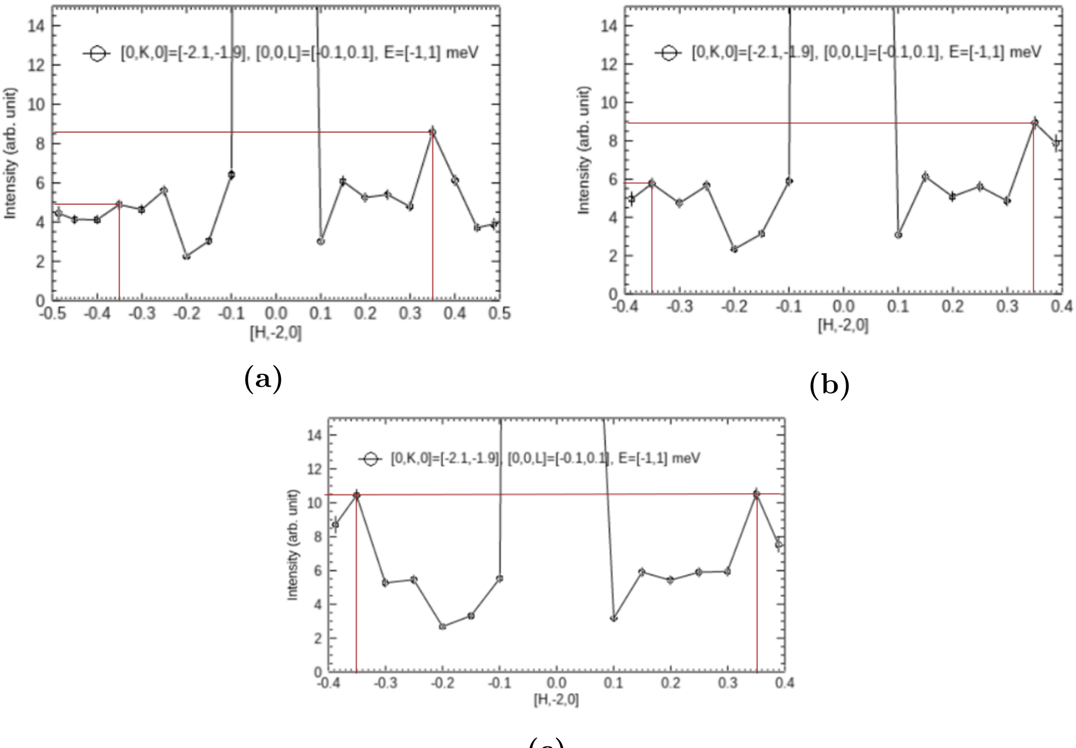

(a) **(b)**

(c)

Figure 9.39: Zoom on the feature of interest in order to understand the exact position and intensity of the supposed superstructure peaks (a) At 3 K. (b) At 85 K. (c) At 220 K.

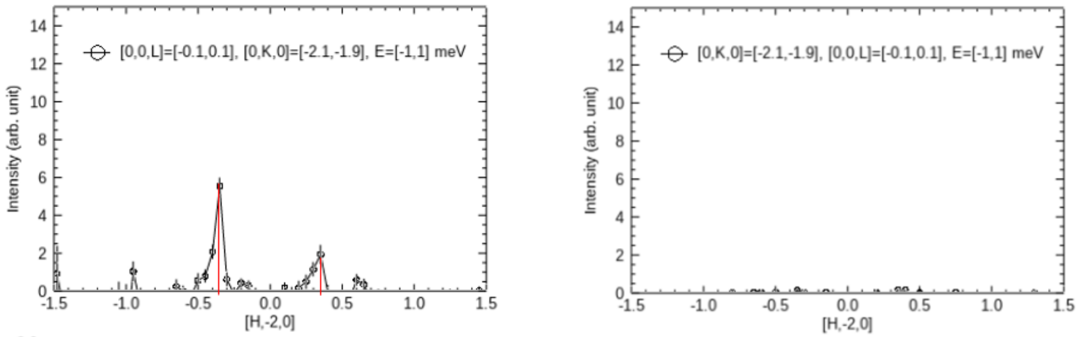

Figure 9.40: Subtraction of the 3 K data from the 220 K data along the H direction in the space. Left: Incoming neutron energy is 61 meV. Right: Incoming neutron energy is 23 meV.

Chapter 10

Discussion

In this work, $LaPt_2Si_2$ has been studied with several different techniques. The very recent synthesis of good quality single crystals allows further investigations to clarify the nature of the interplay between the CDW and SC in this material.
The superconducting state of unconventional superconductors is commonly in competition with other order parameters, as for instance magnetic fluctuations [6]. There are reports of unconventional superconductors in which spin ordering and superconducting state coexist [60] [61].
For a polycrystalline sample [9] a transition temperature $T_S^{pc} = 112$ K has been reported, and more recently the same group of researchers obtained for a power sample, grinded from a single crystal, an ordering temperature $T_S^{powder} = 85$ K [32]. At the structural transition, the onset of a charge density wave with periodicity of three multiples of the lattice constant a has been observed.

Nonmagnetic calculations were performed with the commercial VASP software [62, 63] and Phonopy [31] by Johan Hellsvik, from PDC Center for High Performance Computing, KTH, Sweden. Modeling of the phonon spectra of $LaPt_2Si_2$ can be found in Fig. 10.1. The supercell that has been used is 3 x 3 x 2 with k point grid 6 x 6 x 6. The exchange correlation potential is PBE and the phonon calculations were performed with spin-orbit coupling.
30 phonon dispersion curves are expected in total, since the work was performed with 10 atoms and 1 primitive cell. Three are acoustic phonons and the rest are optical phonons, which is in good agreement with what has been described in the theory section.
The negative regions in some acoustic branches indicate that the phonon mode is close to a structural instability. The energy is actually imaginary, but in order to presenting it in a regular graph, it is shown as a negative number. The imaginary energies appear for phonon modes where the forces are displacive and bring the atoms away from their equilibrium positions.

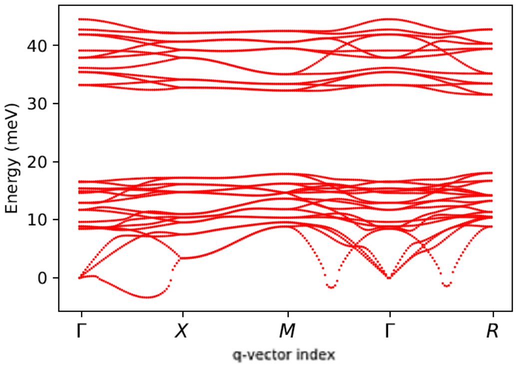

Figure 10.1: Phonon band structure from a $3 \times 3 \times 2$ supercell VASP PBE SOC calculation.

By comparing the INS results with the theoretical calculation, the overall measured phonon dispersions show the two main energy levels predicted. There are strong phonon features below 20 meV that are also investigated in Chapter 9. The bands between 32 and 40 meV, present in Fig. 10.1 were neglected in the analysis as their intensity is much weaker compared to the low energy bands. Instead, if the whole intensity range is taken into account, as seen in Fig. 10.2, it is possible to observe that just below 40 meV there are some evidence of weak optical phonon bands in a compact way.

Kim et al. [8] studied the single elements contribution to the curve, they conclude that the CDW exist in the Pt_3-Pt_4. The theoretical calculations done are in good agreement with their results. In particular, they conclude that in the low energy band, the Pt_3-Pt_4 layer is the one responsible for the presence of the phonons from 0 to 10 meV. Around 12 meV, the curve presented a local minimum, and subsequently another maximum, where both the Pt_1-Pt_2 and the La_1-La_2 layers are responsible for. The upper energy levels are mainly related to the silicon atoms. As seen in Fig. 10.1, the first optical phonon bands and the acoustic phonon are overlapping, therefore it is not easy to determine the respective edges.

The aim of the INS experiment was to investigate the phonon spectra of $LaPt_2Si_2$, in order to observe the phonon softening predicted, and confirm in this way the occurrence of CDW.

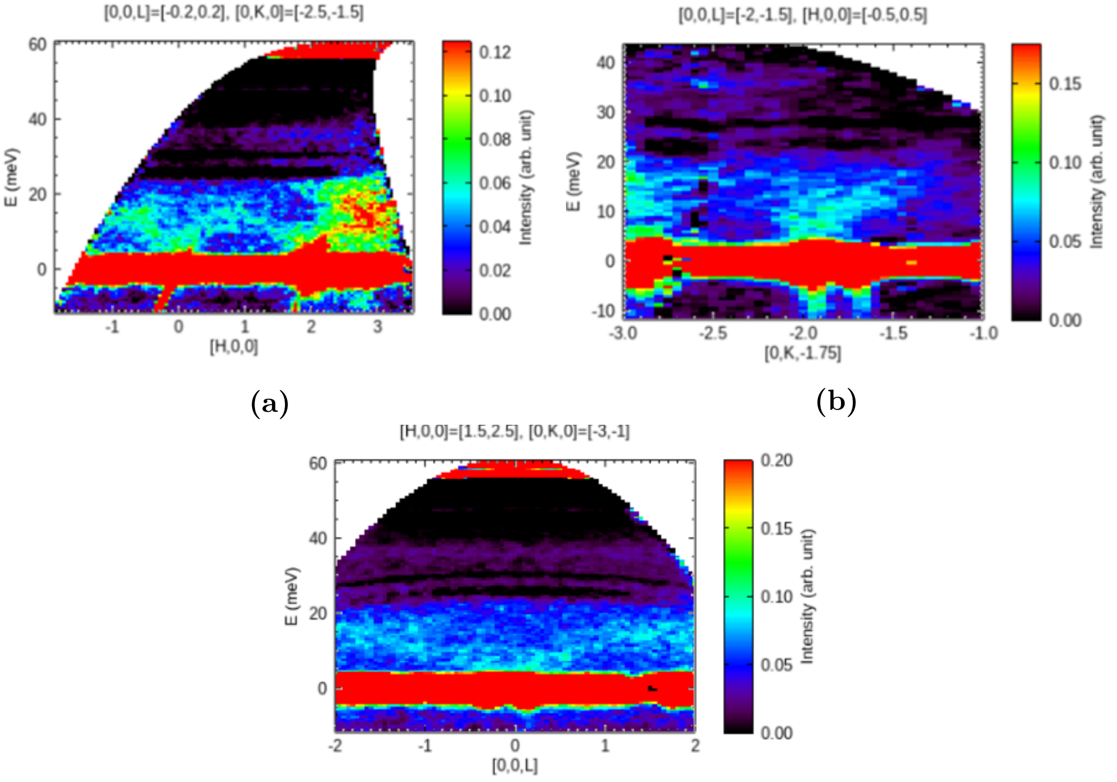

(a) **(b)**

(c)

Figure 10.2: Evidence of the phonon dispersion fingerprint between 35 and 40 meV along different directions in the $\vec{Q}$ space.

The analysis of the inelastic scattering data has been done at all the three temperatures collected (3 K, 85 K and 220 K). At first, an overview on the H-K plane at different energy ranges has been plotted in order to find the energy range at which the dispersion relation appears more clear. In this range, the two Bragg points of interest have been selected and analysed in Chapter 9. The background has been subtracted. The cuts in the full 4D $\vec{S}(Q_x, Q_y, Q_z, \omega)$ INS data set have been done along all the three directions (H,K,L) with the integration along the other two directions. For every direction and every plot, several intensity ranges have been tried in order to find the range in which the features were more visible.

Above 30 meV, there is no strong dispersion, therefore the energy range taken into account in the analysis is [0, 30] meV.

At the beginning, the whole Brillouin zone along the integrated directions is taken into account, then the ranges are decreased, at first only along one direction, and then along both, always around the Bragg point of interest. In general, the range goes from ±1 to ±0.2 around the two Bragg points considered (0,-2,0) and (2,-2,0).

Almost the entire analysis has been shown for 3 K and then only the most relevant plots have been shown for the other two temperatures, 85 K and 220 K. Once selected, these same plots have been cut along the Q space directions for a constant energy range, and the maximum intensities have been selected and pointed in the relevant plots. The points are then linked by a black line, to be a guide for the eye.

In general, the phonon spectra presents some very clear patterns in terms of acoustic branches for the longitudinal(H) and transverse modes(K) in the low energy transfer range.

Just above the elastic line, from approximately 3 meV one can observe the acoustic modes. At 10 meV there is the superimposition between the longitudinal acoustic and longitudinal optic up until 18 meV. This is in agreement with the theoretical calculations, showing different intensities on the plots of Chapter 9. This is a drawback in determining the edges of each band. Above this energy, the phonon are difficult to see and also they are not organized in a typical band-like structure, in fact they appear as groups/clusters. Since the material shows some anisotropies, in the upper energy range, it is possible to see different features, which are not consistent in every Q-point. Similar behaviour is present in the transverse modes (K). Along the L direction instead, the dispersion relation is very random when seen with the center at (0,-2, 0), instead the acoustic branches become very clear around (2,-2,0). Some optical branches with weaker intensity might be present.

When analysing the data at 3K, the intensities decrease, but here the optical branches are more visible, specifically from 5 to 20 meV due to the Pt and La atoms, in fact there is no clear distinction between the acoustic and optic and they appear as a single band.

If then we move to the upper optical band, this is not organised in a band-like structure, and their intensity remains low compared to the branches at lower energy. One cause for this is that the Silicon atoms provides the main contribution for the high-energy phonons and Si has a lower neutron scattering length when compared to both La and Pt, resulting in lower intensity levels.

Concerning the superstructure peaks, the investigation at $E_i = 12$ meV was unsuccessful because the q range is not covered. The peaks at $E_i = 23$ meV are very weak and almost imperceptible. From the subtraction of the 3 K data from the 220 K data, the only difference is spotted exactly at q $\approx$ [0.35, 0, 0)] along H, suggesting that the position of the satellites is in agreement with XRD [1] where the satellites are seen at wave vector q $\approx$ [0.36, 0, 0)].

The disagreement is with the intensity trend of the satellites at different temperatures. In INS data the maximum is at 220 K and then they decrease at 85 K and 3 K, leaving the satellite on the positive side of H being the one with the higher intensity, as seen in Fig. 9.38 and Fig. 9.39.

The analysis is not able to justify their unexpected dependence on temperature. The data do not have the necessary resolution for structural analysis and precise determination of the Q-vector for the satellite peaks.
To conclude, the INS results provided a good overview of the phonon spectra in $LaPt_2Si_2$, but the resolution necessary to resolve an eventual phonon softening was not present and these results opened further questions regarding the structural transition.

More experiments have been performed on $LaPt_2Si_2$ in order to study its properties and in order to reply to some of the questions opened by the INS results.
The performed resistivity measurements show the superconducting nature of the material. Moreover a transition at around 100 K is observed as seen in Fig. 5.2, which could be related to the CDW [1]. The results are in good agreement with the literature [1] [15] [33] [9] [12]. The hysteresis in resistivity of $LaPt_2Si_2$ between cooling and heating data confirms the first order nature of the phase transition.
Raman scattering has been performed and from Fig. 5.10 it is possible to observe that the center and the FHWM are shifting with respect to the temperature. At 85 K there is something anomalous and this could be the fingerprint of the CDW at 85 K.
The FWHM behaviour is consistent with the literature results [1], it shows a clear constant dependence above 200K and a clear increase below 200 K, which lead us to the conclusion that the CDW is present. As reported in the literature, the anomaly at 85 K is compatible with the occurrence of a structural transition associated with a CDW transition.

From X-ray diffraction between 80 K and 300 K, the 2D maps of the Bragg reflections show the appearance of satellites at 85 K in the hk0 plane only, with periodicity (0.36, 0, 0) which is exactly the one observed from past research [1]. Comparing the integrated intensity of the satellites as function of temperature of our data with the Falkowski paper (Fig. 6.7), the results overall look quite similar; however, our data have more structure and several differences in the trend that cannot be discarded. The difference in the trend could be caused by the limited angular coverage that Falkowski's group mentioned, therefore it is possible that they did not see the whole evolution of the structure. On the other hand, due to lack of time, the range of temperatures in the acquisition of the data from 110 K increases. Another interesting point is that we see an increase in the satellites intensity at 220 K from the INS data, while it is not clear from the XRD data what happens above 180 K. In Fig. 6.7 there is a slightly increase in intensity from 200 K whose nature could be the background or something nonphysical.

A check in order to understand if the structural transition occurs has been done

by studying the equivalent reflections for the tetragonal symmetry at different temperatures. The one investigated in this case was the operation hkl which should be equal to -khl. This is not true instead in the orthorhombic case, therefore by performing this check, one of the two structure can be selected.
Two peaks investigated were (2,1,0) and (-1,2,0), as shown in Fig. 6.8, are equal in the whole range within the calculated error except at 85 K, where the values are very different and exceed the errorbar. To conclude, the behaviour at 85 K could be a hint of the change of symmetry, however the measurement is limited in the temperature range and resolution. Therefore, it is not possible to obtain a complete structural characterization.

Chapter 11

Conclusion and Outlook

The phonon excitation spectra was investigated below and above the structural transition T_{CDW} = 85 K and we acquired maps at 3 different temperatures (3 K, 85 K, 220 K), for the first time. The CDW wavevector q=(0.35,0,0) was clearly observed, but no phonon softening was observed. The measured phonon dispersions are in good agreement with theoretical predictions, showing two main energy levels (4-18meV and 32-42meV), and weak superlattice peaks were observed.
Interestingly, the incommensurate peaks we observed (q $\approx$ [0.35, 0, 0]), by doing zero-energy-transfer cuts, were present in the full temperature range, even increasing in temperature above T_{CDW} , which is different from what has been observed in XRD data [1]. The resolution was not enough to shown an eventual phonon softening and opened further questions regarding the structural transition.

Resistivity measurements confirmed the superconducting nature of $LaPt_2Si_2$ and a transition around 100 K was observed, which could lead to CDW.
The Raman scattering experiment confirmed the presence of the CDW. The anomaly at 85 K is compatible with the occurrence of a structural transition associated with a CDW transition, as reported in the literature.

The results from X-ray diffraction lead us to the identification of the unit cell and the clear observations of satellites in the hk0 plane. The trend in intensity of the satellites when compared to the previous literature [1] has important differences that cannot be discard. Due to lack of time, the range of temperatures in the acquisition of the data from 110 K increases, therefore more time should be allocated to the study of the trend above this temperature, to better compare it with the previous results.
When looking at the equivalent reflections for the tetragonal symmetry, the trend was the same for the two peaks analysed and then only clear difference has been observed at 85 K. This can be a hint of the change of symmetry however such

measurement does not provide complete structural characterization. In order to improve this picture, further measurements at both lower and higher temperature should be performed, in order to have a complete overview of the intensity of the satellites in a broader temperature range and check again if the trend is comparable to the Falkowski result and consistent with the increase of the intensity of the satellites around 220 K that is seen in INS results. The statistics could also be improved if more time can be allocated to each temperature measurements and more temperatures could be taken above 110 K. Moreover,in order to determine a change in the symmetry in an accurate way, a structural analysis with a refinement is needed.

Further investigations on the single crystal are necessary, in particular Neutron Diffraction (ND) in order to clarify the structural evolution of single-crystalline $LaPt_2Si_2$. A single crystal diffractometer would be needed to perform structural characterization with better resolution compared to the X-rays diffractometer used. In order to reach lower T, higher resolution and probably see the very weak crystalline structure changes, the experiment should be performed at a large scale facility. Moreover, X-rays detect also charge ordering effects, which we would like to exclude by using neutrons.

Another suggestion could be to integrate the DFT calculations with the studies on the Raman active modes. From the phonon eigenvalues and eigenvectors, it would be possible to label the symmetries of modes and calculate the correct frequencies. This could lead to verifying numerically if the 300 cm^{-1} is what we expect for B2G.

Finally, for the future could be to study also the superconducting state, where 1.6 K needs to be reached for single crystals [1], once the structure and CDW nature would be clarified.

Bibliography

[1] M. Falkowski, P. Doležal, A. V. Andreev, E. Duverger-Nédellec, and L. Havela. «Structural, thermodynamic, thermal, and electron transport properties of single-crystalline $LaPt_2Si_2$». In: *Phys. Rev. B* 100 (2019), p. 064103 (cit. on pp. i, 3–7, 43, 44, 51, 53, 58, 59, 101, 107, 108, 110, 111).

[2] J. Bardeen, L. N. Cooper, and J. R. Schrieffer. «Microscopic Theory of Superconductivity». In: *Phys. Rev.* 106 (1957), pp. 162–164 (cit. on pp. 1, 2).

[3] J. Bardeen, L. N. Cooper, and J. R. Schrieffer. «Theory of Superconductivity». In: *Phys. Rev.* 108 (1957), pp. 1175–1204 (cit. on pp. 1, 2).

[4] J. G. Bednorz and K. A. Müller. «Possible high T_c superconductivity in the Ba-La-Cu-O system». In: *Zeitschrift fur Physik B Condensed Matter* 64 (1986), pp. 189–193 (cit. on p. 1).

[5] John Tranquada, B. Sternlieb, John Axe, Y. Nakamura, and Shin-ichi Uchida. «Evidence for stripe correlations of spins and holes in copper oxide superconductors». In: *Nature* 375 (1995), pp. 561–563 (cit. on p. 2).

[6] D. J. Scalapino. «A common thread: The pairing interaction for unconventional superconductors». In: *Rev. Mod. Phys.* 84 (2012), pp. 1383–1417 (cit. on pp. 2, 104).

[7] I. Hase and T. Yanagisawa. «Electronic structure of $LaPt_2Si_2$». In: *Physica C: Superconductivity* 484 (2013), pp. 59–61 (cit. on pp. 2, 44).

[8] Sooran Kim, Kyoo Kim, and B. I. Min. «The mechanism of charge density wave in Pt-based layered superconductors: $SrPt_2As_2$ and $LaPt_2Si_2$». In: *Scientific Reports* 5 (2015), p. 15052 (cit. on pp. 2, 3, 44, 56, 105).

[9] Ritu Gupta, U B Paramanik, S Ramakrishnan, K P Rajeev, and Z Hossain. «Coexistence of superconductivity and a charge density wave in $LaPt_2(Si_1 - xGe_x)_2(0 \leqslant x \leqslant 0.5)$». In: *Journal of Physics: Condensed Matter* 28.19 (2016), p. 195702 (cit. on pp. 3–5, 41, 43, 104, 108).

[10] Mazza Federico. «First Principle Calculations & Inelastic Neutron Scattering on the Single-Crystalline Superconductor $LaPt_2Si_2$». MA thesis. KTH, Materials Science and Engineering, 2020, p. 60 (cit. on p. 3).

[11] *VESTA, Visualization for Electronic and structural analysis.* 2021. URL: `https://jp-minerals.org/vesta/en/` (cit. on p. 3).

[12] Yutaro Nagano, Nobutaka Araoka, Akihiro Mitsuda, Hideki Yayama, Hirofumi Wada, Masaki Ichihara, Masahiko Isobe, and Yutaka Ueda. «Charge Density Wave and Superconductivity of RPt_2Si_2 ($R =$ Y, La, Nd, and Lu)». In: *Journal of the Physical Society of Japan* 82.6 (2013), p. 064715 (cit. on pp. 4, 41, 43, 53, 108).

[13] Debarchan Das, Ritu Gupta, A. Bhattacharyya, P. K. Biswas, D. T. Adroja, and Z. Hossain. «Multigap superconductivity in the charge density wave superconductor $LaPt_2Si_2$». In: *Physical Review B* 97.18 (2018) (cit. on pp. 4, 41, 44).

[14] Tetsuro Kubo, Yasuhide Kizaki, Hisashi Kotegawa, Hideki Tou, Yutaro Nagano, Nobutaka Araoka, Akihiro Mitsuda, and Hirofumi Wada. «Structural Phase Transition and Superconductivity in $LaPt_2Si_2$>: ^{1}39La- and ^{1}95Pt-NMR Studies». In: *JSP, The Physics Society of Japan* (2014) (cit. on p. 4).

[15] Ritu Gupta, A. Thamizhavel, P. Rodière, S. Nandi, K. P. Rajeev, and Z. Hossain. «Electrical resistivity under pressure and thermal expansion of LaPt 2 Si 2 single crystal». In: *Journal of Applied Physics* 125.14 (2019), p. 143902 (cit. on pp. 4, 43, 108).

[16] Robert E. Thorne. «Charge-Density-Wave Conductors». In: *Physics Today* 49.5 (1996), pp. 42–47 (cit. on p. 6).

[17] Kim Lefmann. *Neutron Scattering:Theory, Instrumentation,and Simulation.* Niels Bohr Institute, University of Copenhagen, 2020 (cit. on pp. 8, 10, 14, 16, 19, 24, 25, 29, 31, 34–36).

[18] European Spallation Source. *Science Using Neutrons.* 2020. URL: `https://europeanspallationsource.se/science-using-neutrons` (cit. on p. 8).

[19] R. P. Feynman. *The Feynman Lectures on Physics.* Addison Wesley Longman, 1970 (cit. on p. 9).

[20] J.L. Garcia-Luna A. Garcia and G.L. Castro. «Neutron beta decay and the current determination of V-ud». In: *Phys. Lett. B* 500 (2001), p. 66 (cit. on p. 9).

[21] Jaehong Jeong, Sanghyun Lee, and Je-Geun Park. «Introduction to Neutron Scattering for Magnetic Materials Research». In: *Journal of the Korean Magnetics Society* 22 (2012) (cit. on p. 11).

[22] Tapan Chatterji. «CHAPTER 1 - Magnetic Neutron Scattering». In: *Neutron Scattering from Magnetic Materials.* Ed. by Tapan Chatterji. Elsevier Science, 2006, pp. 1–24 (cit. on p. 13).

[23] J. Howard. «Determination of the neutron absorption cross section for hydrogen as a function of wavelength with a pulsed neutron source». In: *J. Appl. Cryst.* 20 (1987), pp. 120–122 (cit. on p. 13).

[24] P. Henry. *NIST Chemistry WebBook.* 2011. URL: `https://webbook.nist.gov/chemistry/` (cit. on p. 13).

[25] R. L. McGreevy I. S. Anderson and H. Z. Bilheux. *Neutron imaging and applications.* Springer, 2009 (cit. on p. 20).

[26] Anastasios Pateras. «Three dimensional X-ray Bragg ptychography of an extended semiconductor heterostructure». PhD thesis. 2015 (cit. on p. 22).

[27] Institut Laue-Langevin. *D2B - HIGH-RESOLUTION TWO-AXIS DIFFRACTOMETER.* URL: `https://www.ill.eu/users/instruments/instruments-list/d2b/description/instrument-layout` (cit. on p. 26).

[28] Kirsten M. Ø. Jensen. *Neutron Powder Diffraction and Rietveld refinement.* 2018 (cit. on p. 27).

[29] C.Kittel. *Introduction to Solid State Physics.* Wiley, 2004 (cit. on p. 35).

[30] G. Kresse and J. Furthmüller. «Efficient iterative schemes for ab initio total-energy calculations using a plane-wave basis set». In: *Phys. Rev. B* 54 (1996), pp. 11169–11186 (cit. on pp. 36, 48).

[31] Atsushi Togo and Isao Tanaka. «First principles phonon calculations in materials science». In: *Scripta Materialia* 108 (2015), pp. 1–5 (cit. on pp. 36, 37, 104).

[32] Ritu Gupta, S K Dhar, A Thamizhavel, K P Rajeev, and Z Hossain. «Superconducting and charge density wave transition in single crystalline $LaPt_2Si_2$». In: *Journal of Physics: Condensed Matter* 29.25 (2017), p. 255601 (cit. on pp. 41, 53, 101, 104).

[33] Ritu Gupta, K P Rajeev, and Z Hossain. «Thermal transport studies on charge density wave materials LaPt2Si2 and PrPt2Si2». In: *Journal of Physics: Condensed Matter* 30.47 (Nov. 2018), p. 475603 (cit. on pp. 43, 108).

[34] J. C. Tsang, C. Hermann, and M. W. Shafer. «Raman Spectroscopy of the Charge-Density-Wave State in TaS_3». In: *Phys. Rev. Lett.* 40 (23 1978), pp. 1528–1531 (cit. on pp. 44, 50, 51).

[35] J Petzelt and V Dvorak. «Changes of infrared and Raman spectra induced by structural phase transitions. I. General considerations». In: *Journal of Physics C: Solid State Physics* 9.23 (1976), pp. 4355–4355 (cit. on p. 44).

[36] J. D. Axe and G. Shirane. «Influence of the Superconducting Energy Gap on Phonon Linewidths in Nb_3Sn». In: *Phys. Rev. Lett.* 30 (6 1973), pp. 214–216 (cit. on p. 44).

[37] Daniel C. Harris and Michael D. Bertolucci. Dover Publications, 1989 (cit. on p. 45).

[38] Moxfyre. *Raman energy levels*. 2009. URL: `https://commons.wikimedia.org/wiki/File:Raman_energy_levels.svg` (cit. on p. 45).

[39] John R. Ferraro, Kazuo Nakamoto, and Chris W. Brown. In: *Introductory Raman Spectroscopy (Second Edition)*. Ed. by John R. Ferraro, Kazuo Nakamoto, and Chris W. Brown. Second Edition. Academic Press, 2003, pp. 1–94 (cit. on pp. 46, 48).

[40] Teledyne Princeton Instruments. *TriVista Universal Raman Solution*. 2021. URL: `https://www.princetoninstruments.com/` (cit. on p. 47).

[41] Yuki Itoh and Takeshi Hasegawa. «Polarization Dependence of Raman Scattering from a Thin Film Involving Optical Anisotropy Theorized for Molecular Orientation Analysis». In: *The Journal of Physical Chemistry A* 116 (2012), pp. 5560–5570 (cit. on p. 48).

[42] Bilbao Crystallographic Server. *IR Raman and Hyper-Raman Modes*. 2021. URL: `http://www.cryst.ehu.es` (cit. on pp. 48, 49).

[43] E. Kroumova, M.I. Aroyo, J.M. Perez-Mato, A. Kirov, C. Capillas, S. Ivantchev, and H. Wondratschek. «Bilbao Crystallographic Server : Useful Databases and Tools for Phase-Transition Studies». In: *Phase Transitions* 76.1-2 (2003), pp. 155–170 (cit. on p. 48).

[44] Norman B. Colthup, Lawrence H. Daly, and Stephen E. Wiberley. In: *Introduction to Infrared and Raman Spectroscopy (Third Edition)*. Ed. by Norman B. Colthup, Lawrence H. Daly, and Stephen E. Wiberley. Third Edition. Academic Press, 1990, pp. 1–73 (cit. on p. 48).

[45] Bruker. *D8 VENTURE*. 2010. URL: `www.bruker.com` (cit. on p. 54).

[46] University of London School of Crystallography Birkbeck College. *Reflection Multiplicity*. 2006. URL: `http://pd.chem.ucl.ac.uk/pdnn/symm2/multj.htm` (cit. on p. 59).

[47] J-PARC Center. *About J-PARC*. 2014. URL: `https://j-parc.jp/en/jparc.html` (cit. on pp. 61, 62).

[48] J-PARC Center. *Materials and Life Science Experimental Facility*. 2020. URL: `http://j-parc.jp/c/en/facilities/mlf/index.html` (cit. on p. 62).

[49] Shoji Nagamiya. «Introduction to J-PARC». In: *Progress of Theoretical and Experimental Physics* 2012 (2012), p. 13 (cit. on p. 62).

[50] Shinichi Itoh, Tetsuya Yokoo, Setsuo Satoh, Shin Ichiro Yano, Daichi Kawana, Junichi Suzuki, and Taku J. Sato. «High Resolution Chopper Spectrometer (HRC) at J-PARC». In: *Nuclear Instruments and Methods in Physics Research, Section A: Accelerators, Spectrometers, Detectors and Associated Equipment* 631 (2011), pp. 90–97 (cit. on p. 63).

[51] Kim Lefmann et al. «Simulation of a suite of generic long-pulse neutron instruments to optimize the time structure of the European Spallation Source». In: *Review of Scientific Instruments* 84 (2013) (cit. on p. 63).

[52] Kim Lefmann, Peter Willendrup, Emmanuel Farhi, Peter Christiansen, and Klaus Lieutenant. «Component Manual for the Neutron Ray-Tracing Package McStas, Version 1.9». In: (2006) (cit. on p. 63).

[53] Shinichi Itoh, Tetsuya Yokoo, Takatsugu Masuda, Shinichiro Asai, Hiraku Saito, Daichi Kawana, Ryosuke Sugiura, Toshio Asami, and Yoshiaki Ihata. «Progress in High Resolution Chopper Spectrometer HRC by improving collimator and Fermi chopper». In: *Physica B: Condensed Matter* 568 (2019), pp. 76–80 (cit. on pp. 64–66).

[54] Shinichi Itoh, Kenji Ueno, and Tetsuya Yokoo. «Fermi chopper developed at KEK». In: *Nuclear Instruments and Methods in Physics Research Section A: Accelerators, Spectrometers, Detectors and Associated Equipment* 661.1 (2012), pp. 58–63 (cit. on p. 64).

[55] "Meet At MLF" Production Committee. *HRC High Resolution Chopper Spectrometer*. 2015. URL: `https://mlfinfo.jp/en/bl12/` (cit. on p. 65).

[56] KEK HIGH ENERGY ACCELERATOR RESEARCH ORGANIZATION. *Using neutrons to see waves in a solid*. 2010. URL: `https://www2.kek.jp/proffice/archives/feature/2010/NeutronCHOPPER.html` (cit. on p. 65).

[57] SAP HANA. *HANA*. Version SAP S/4HANA Cloud. URL: `https://saphanajourney.com/` (cit. on p. 67).

[58] NIST Center for Neutron Research. *DAVE Data Analysis and Visualization Environment*. Version 2.4. Mar. 5, 2020. URL: `https://www.ncnr.nist.gov/dave/` (cit. on p. 67).

[59] Wei-Wei Zhang, Hong Yu, Shuang-Ying Lei, and Qing-An Huang. «Modelling of the elastic properties of crystalline silicon using lattice dynamics». In: *Journal of Physics D: Applied Physics* 44 (Aug. 2011), p. 335401 (cit. on p. 77).

[60] Qing-Wei Wang, Da-Yong Liu, Ya-Min Quan, and Liang-Jian Zou. «Coexistence and competition of spin-density-wave and superconducting order parameters in iron-based superconductors». In: *Physics Letters A* 380.34 (2016), pp. 2685–2692 (cit. on p. 104).

[61] Eun Gook Moon and Subir Sachdev. «Competition between spin density wave order and superconductivity in the underdoped cuprates». In: *Phys. Rev. B* 80 (2009), p. 035117 (cit. on p. 104).

[62] G Kresse and J Furthmüller. «Efficient iterative schemes for ab initio total-energy calculations using a plane-wave basis set». In: *Physical Review B* 54.16 (Oct. 1996), pp. 11169–11186 (cit. on p. 104).

[63] G Kresse and J. Furthmüller. «Efficiency of ab-initio total energy calculations for metals and semiconductors using a plane-wave basis set». In: *Computational Materials Science* 6.1 (1996), pp. 15–50 (cit. on p. 104).